Experimental and Numerical Analysis of Hydroformed Tubular Materials for Superconducting Radio Frequency (SRF) Cavities

DISSERTATION

Presented in Partial Fulfillment of the Requirements for the Degree Doctor of Philosophy

in the Graduate School of The Ohio State University

By

Hyun Sung Kim

Graduate Program in Materials Science and Engineering

The Ohio State University

2016

Dissertation Committee:

Professor Michael D. Sumption, Adviser

Professor Glenn Daehn

Professor Alan A. Luo

Professor Edward A. Overman

Abstract

Superconducting radio frequency (SRF) cavities represent a well established technology benefiting from some 40 years of research and development. An increasing demand for electron and positron accelerators leads to a continuing interest in improved cavity performance and fabrication techniques. Therefore, several seamless cavity fabrication techniques have been proposed for eliminating the multitude of electron-beam welded seams that contribute to the introduction of performance-reducing defects. Among them, hydroforming using hydraulic pressure is a promising fabrication technique for producing the desired seamless cavities while at the same time reducing manufacturing cost.

This study focused on experimental and numerical analysis of hydroformed niobium (Nb) tubes for the successful application of hydroforming technique to the seamless fabrication of multi-cell SRF cavities for particle acceleration. The heat treatment, tensile testing, and bulge testing of Cu and Nb tubes has been carried out to both provide starting data for models of hydroforming of Nb tube into seamless SRF cavities. Based on the results of these experiments, numerical analyses using finite element modeling were conducted for a bulge deformation of Cu and Nb. In the experimental part of the study samples removed from representative tubes were prepared for heat treatment, tensile testing, residual resistance ratio (*RRR*) measurement, and orientation imaging electron microscopy (OIM). After being optimally heat treated Cu and Nb tubes were subjected to hydraulic bulge testing and the results analyzed. For numerical analysis of hydroforming process, two different simulation approaches were used. The first model was the macro-scale continuum model using the constitutive equations (stress-strain relationship) as an input of the simulation. The constitutive equations were obtained from the experimental procedure including tensile and tube bulge tests in order to investigate the influence of loading condition on deformation behavior. The second model was a multi-scale model using both macroscopic continuum model and microscopic crystal plasticity (CP) model: Frist, the constitutive equation was obtained from the other microscopic simulation model (CP-FEM) using the microstructural information (i.e., orientation) of materials from the OIM and simple tensile test data. Continuum FE analysis based on the obtained constitutive equation using CP model were then fulfilled.

Several conclusions can be drawn on the basis of the experimental and numerical analysis as follows: 1) The stress-strain relationship from the bulge test represents a more accurate description of the deformation behavior for a hydroforming than that from tensile tests made on segments cut from the tubular materials. 2) For anisotropic material, the incorporation of anisotropic effects using anisotropy coefficient from the tensile test led to even more accurate results. 3) A multi-scale simulation strategy using combination of continuum and CP models can give high quality predictions of the deformation under hydroforming of Cu and Nb tubes.

Dedication

This document is dedicated to my father, mother, and sister.

Acknowledgments

I first would like to express my sincere gratitude to my advisors, Professor Edward Collings and Professor Michael Sumption for their valuable advice and intellectual guidance during my graduate studies. I also appreciate Professor Glenn Daehn and Professor Alan Luo for serving as committee members of my dissertation. In addition, I want to acknowledge grant DE-SC0004217 from the Department of Energy (DOE).

I would like to thank Dr. Hojun Lim, Dr. Jinwoo Lee, and Dr. Hyuk Jong Bong who support for my numerical simulation study. Their supporting was critical for my degree. Thanks to the CSMM members including Dr. Milan Majoros, Dr. Michael Susner, Dr. Guangze Li, Cory Myers, Yuan Yang, Chris Kovacs, Xingchen Xu, Yi Ding and Fang Wan. It was great pleasure to work in Center for Superconducting and Magnetic Materials (CSMM). I also appreciate the support from Professor Tylan Altan in Center for Precision Forming (CPF) Center for a hydraulic bulge test, and Dr. Lance Cooley in Fermi Lab for the heat treatment of Nb. Furthermore, I want to appreciate the help from the staffs in our department, and the Center for Electron Microscopy and Analysis (CEMAS). Thanks to my Korean friends for my unforgettable life in Columbus.

Finally, I sincerely thank my father, mother, and sister.

Vita

1982..Born, Busan, Korea

2007..B.S. Materials Science and Engineering, Korea University

2010..M.A. Materials Science and Engineering, Korea University

2010 to present ....Graduate Research Associate, Department of Materials Science and Engineering, The Ohio State University

Publications

H. S. Kim, M. D. Sumption, M. A. Susner, H. Lim and E. W. Collings, “Bulge Testing of Copper and Niobium Tubes for Hydroformed RF Cavities”, Materials Science and Engineering A, vol. 654, 13-20, 2016

H. S. Kim, M. D. Sumption, H. Lim and E. W. Collings, “Evaluation of mechanical properties of tubular materials with hydraulic bulge test for superconducting radio frequency (SRF) cavities", IEEE Trans. Appl. Supercond., vol. 23, no. 3, 2013

H. S. Kim, M. D. Sumption, H. Lim and E. W. Collings, "Analysis of materials properties of niobium tube from the results of virtual bulge test", Advances in Cryogenics Engineering Trans.of the ICMC Conference, vol. 58, 305-12, 2011

Fields of Study

Major Field: Materials Science and Engineering

Table of Contents

List of Tables

List of Figures

CHAPTER 1: INTRODUCTION

Dozens of electron-synchrotron-based light source exist worldwide, all of them powered by radio frequency (RF) cavities both for boosting the electrons to final energy and maintaining that energy in the storage ring. The goal of the accelerating cavity designer is to achieve the largest possible operating electric field gradient which implies a high quality factor, Q, and hence a low surface resistance, R_s. To that end early RF cavities were of polished high purity Cu. The R_s of a Cu cavity decreases with decreasing T and ρ until a limit is reached after which it is temperature independent and of order mΩ [1]. To further reduce R_s and increase Q the cavity needs to be lined with or constructed from superconducting material. Currently the superconductor of choice is Nb whose BCS-based R_s is some 3 to 4 orders of magnitude smaller than that of Cu [2]. For these reasons the synchrotrons of high energy particle physics are also powered superconducting RF (SRF) cavities [3-8].

My research topic focused on the fabrication of SRF cavities. Reference [9] presents an overview of SRF cavity fabrication. The process may begin with the preparation of a disc-shaped blank and the formation by pressing of a half-shell; or the preparation of a length of Nb tube followed by the spinning of back-to-back pairs of half-shells. A series of such half-shells are joined by electron-beam (EB) welding to form a multi-cell cavity. Numerous welded seams are required. For example a nine-cell cavity fabricated from half-shells would require some eighteen equatorial and iris seams. To circumvent this costly process new seamless fabrication techniques [10] instead of EB welding emerge to improve electric field gradients and expedite the fabrication of long cavity strings. They include: spin forming [11-13], and hydroforming [14-18]. Use of the hydroforming technique would lead to the elimination of the multitude of EB welded seams which introduce performance-reducing defects. In addition, it is expected to reduce the manufacturing cost and time resulting from the reduced post-preparing process including polishing process [19]. Therefore, hydroforming has been introduced by groups at Japan's High Energy Accelerator Research Organization (KEK) [20] and Gemany's Deutsche Elektronen-Synchrotron (DESY) [9, 14-19, 21] as a way of creating seamless multicell SRF cavities. Under hydroforming, a previously "necked" tube is locked in a die and formed into a series of cells by hydraulic pressure.

1.0 Objective

The hydroforming technique exhibits many advantages for application in SRF cavity, and the technical problems are being solved. However, the fundamental studies associated with deformation as well as numerical simulation studies for a tube hydroforming are not sufficient. Therefore, the objective of study is the development of a numerical simulation model for a tube hydroforming to fabricate multi-cell SRF cavities. This numerical simulation will be used for a design of the cavities, which determines the required material properties (i.e. yield strength, uniform elongation) and process parameters (i.e. loading path). Therefore, accurate numerical prediction is important to avoid the waste of time and cost from failure during fabrication. With a goal of the development of a numerical simulation model, the following four topics will be discussed in this study: 1) verification of an analytical model for obtaining the constitutive equation from a tube bulge test (chapter 3.3), 2) the comparison of constitutive equations from tensile and bulge tests (chapter 4.1.2), 3) the consideration of anisotropic properties using anisotropic coefficients for a tube bulge test (chapter 4.1.3), and 4) a multi-scale simulation model using both continuum and crystal plasticity (CP) models (chapter 4.2).

In this chapter, I first provide a fundamental background for RF cavities and special issues relating to SRF cavities. Characterization methods for mechanical properties of tubular materials are then discussed and appropriate forms to be implemented in the simulation are reviewed.

1.1 Superconducting RF cavities

1.1.1 Cavity basics

An RF cavity is a device which provides an electric field necessary to accelerate a particle beam. Figure 1.1 shows a typical elliptical cavity operating in the fundamental mode (TM 010), in which a longitudinal electric field accelerates the charged particles, and the accompanying magnetic field loops around it [4, 22].

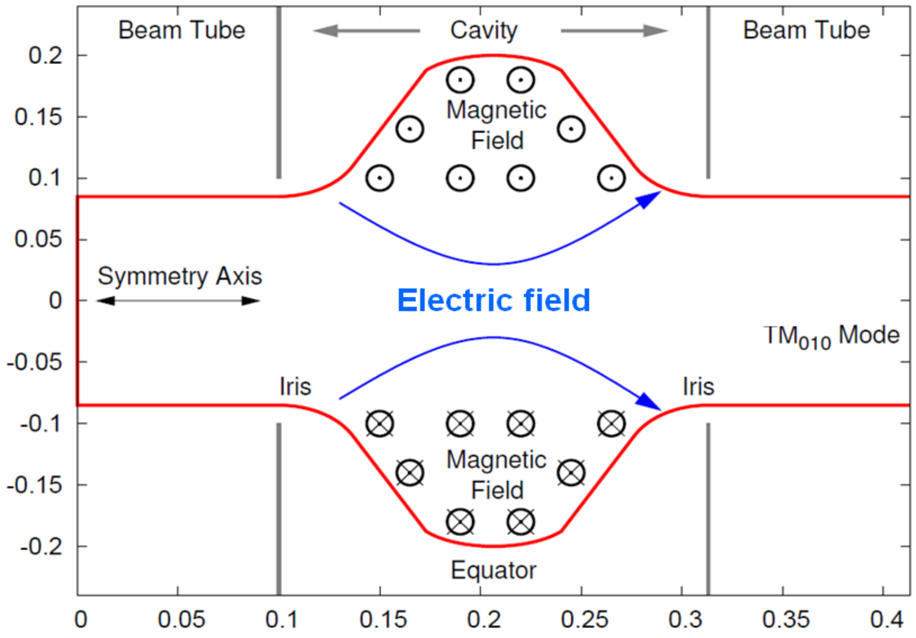

Figure 1.1 Schematic of an elliptical cavity with field lines of TM010 mode

An important parameter for evaluating the performance of the cavity is the accelerating gradient (E_{acc}), which is the time average of the electric field along the particle's flight. The accelerating gradient is defined as

$$E_{acc} = \frac{V_c}{d} \tag{1-1}$$

where d is the cell length, and V_c is the voltage. This voltage can be obtained from the line integral of electric field, E_z, as follows:

$$V_c = \int_0^d E_z(Z) \cdot dz. \tag{1-2}$$

The energy available for accelerators can be increased by extending the accelerating gradients of cavities.

Another important characteristic of a cavity is the quality factor, Q_0, which is a dimensionless parameter representing the efficiency of a cavity. It can be defined as

$$Q_0 = \frac{\omega U}{P_c} \tag{1-3}$$

where ω is the angular frequency, U is the stored energy per cycle of the electromagnetic field in the cavity, and P_c is the power dissipated at the cavity wall. The power dissipation is obtained by the integral of resistive wall losses over the surface of cavity. It can be expressed as

$$P_c = \frac{1}{2} R_s \int_s |H|^2 ds \tag{1-4}$$

where R_s is the surface resistance and H is the magnetic field in the cavity. The stored energy in the cavity can be calculated by integrating the energy density over the volume of the cavity as follows:

$$U = \frac{1}{2} \mu_0 \int_V |H|^2 dV \tag{1-5}$$

where μ_0 is the permeability of free space. However, the integrals of the electromagnetic field in the above expressions are generally hard to solve analytically because of their complexity. Instead, computer programs are used to calculate the fields in the cavity with complex shapes and numerically integrate the above expressions.

In order to evaluate the influence of the cavity's shape alone on the performance of cavity, the geometry factor is introduced:

$$G = \frac{\omega_0 \mu_0 \int_V |H|^2 dV}{\int_s |H|^2 ds}. \qquad (1\text{-}6)$$

Consequently, quality factor can be described by

$$Q_0 = \frac{\omega_0 \mu_0 \int_V |H|^2 dV}{R_s \int_s |H|^2 ds} = \frac{G}{R_s}. \qquad (1\text{-}7)$$

Therefore, as shown in equation 1.7, the quality factor of a cavity can be improved by using a cavity material with low surface resistance since Q_0 is inversely proportional to R_s. Therefore, a superconducting material with zero resistance under certain conditions is used for a cavity. The details relating superconductivity discussed as followed.

1.1.2 Superconductivity

A superconductor has two main characteristics: zero resistance and diamagnetism. A superconductor has no resistance to the flow of electricity below a certain temperature called the critical temperature (T_c) [23]. In normal conducting materials, the existence of resistivity is due to the scattering of charge carriers (electrons) by phonons and impurities. In case of superconductors, the electrons are coupled, forming cooper pairs which are not scattered; as a result, zero resistance is obtained. Another important property of superconductors is the expulsion of a suitably small magnetic field from a superconductor. When a magnetic field is applied, current circulating at the surface of the superconductor contributes to an induced magnetic field that exactly opposes the direction of the applied field; the material expels the external magnetic field. The material is strongly diamagnetic as a result. The complete expulsion of the magnetic field from the interior of a superconductor is known as the Meissner-Ochsenfeld effect [24].

Superconductivity is governed by a critical surface relating the three electro-magnetic properties: the critical temperature (T_c), the critical magnetic field (H_c), and the critical current density (J_c). Although there are in-depth formulas governing their relations to each other, figure 1.2 illustrates the general case. Outside this critical surface, the superconductor will lose its superconductivity, and revert to its normal state properties. Therefore, higher values of these critical values are preferred for commercial and industrial applications such as power cables, fault current limiters, magnetic resonance imaging devices, motors, and so on [25]. The superconducting RF cavity is one well-established application and is the focus of this research.

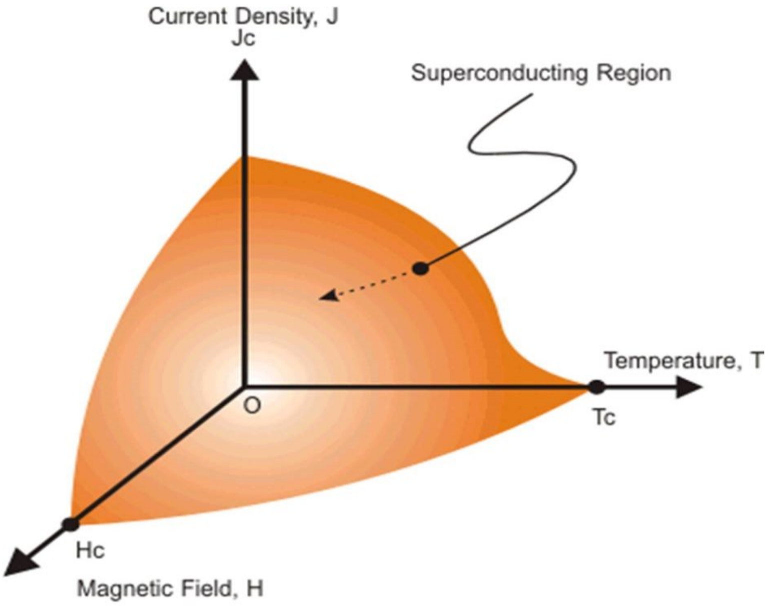

Figure 1.2 Critical surface for superconductivity

The most significant advantage of a superconducting accelerating cavity is the ability to obtain a higher quality factor compared to a normal-conducting cavity. As mentioned before (equation 1.7), the quality factor is determined by the surface resistance, so the extremely low surface resistance of superconducting cavities contributes to the lower energy dissipation compared to the normal cavity. Therefore, the RF source driving the cavity needs only to provide the RF power absorbed by the particle beam being accelerated; power dissipation in the normal- conducting cavity wall can easily equal or exceed the beam power consumption [4].

Although SRF cavities make possible a wider variety of accelerator designs, there are certain issues unique for SRF cavities that must be addressed. The Q_o values tend to degrade as the accelerating field increases, as depicted in a "Q vs. E" curve, figure 1.3. Ideally, the cavity Q_o would remain constant as the accelerating field is increased up to the critical magnetic field of cavity materials, as depicted by the "ideal" line in the plot. However, Q value is generally limited before accelerating field reaches a critical value. Several factors contribute to the drop in the Q value, including multipacting, thermal breakdown, and field emission.

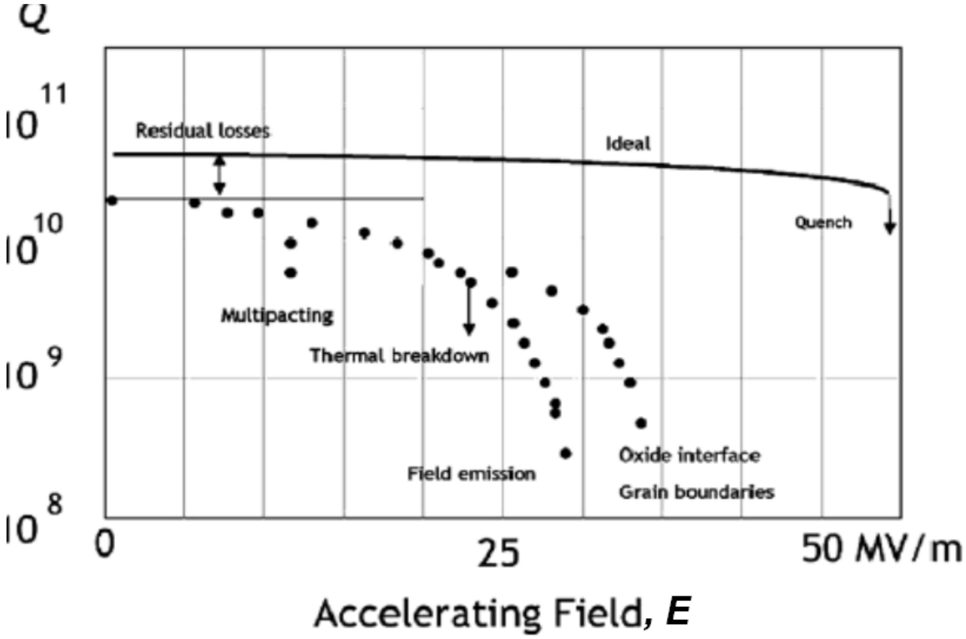

Figure 1.3 *Q* slope of superconducting RF cavity [8]

Multipacting is a resonant process caused by the impact of electrons on the cavity surface and the resultant release of secondary electrons. This secondary electron emission in resonance with the electric field leads to exponential electron multiplication via an electron avalanche. In this way, a large number of electrons build up spontaneously and absorb RF power. This problem has been solved by changing the cavity shape from a rectangular to a spherical or elliptical shape. As shown in figure 1.4, in the elliptical shaped cavity, the released secondary electrons move to the equator of the cavity where electric field is not sufficient to fully accelerate the electrons.

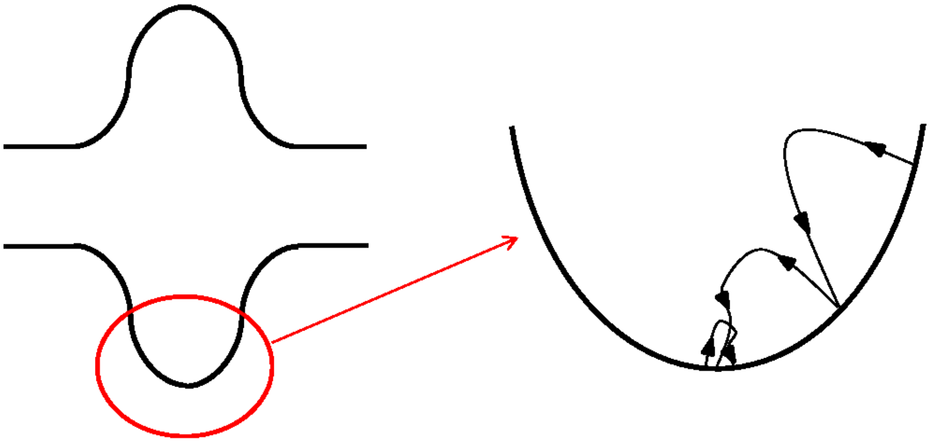

Figure 1.4 Elliptical shaped cavity eliminates multipacting [4]

Thermal breakdown imposes another limitation on the gradient where the temperature of part of the RF surface exceeds the critical temperature causing quench, i.e. the loss of superconductivity. Thermal breakdown is most often a localized effect, in which a small defect in the cavity surface causes its temperature to rise above T_c. Although a defect-free surface is most obvious solution to avoid quench, it is difficult to achieve in all of the cavities in a string. Alternatively, the use of higher thermal conductivity of cavity materials allows the defect and Nb around it to stay below the critical temperature, figure 1.5. Therefore, thermal conductivity can be improved by associating the cavity surface with a high conductivity metal such as high purity Cu.

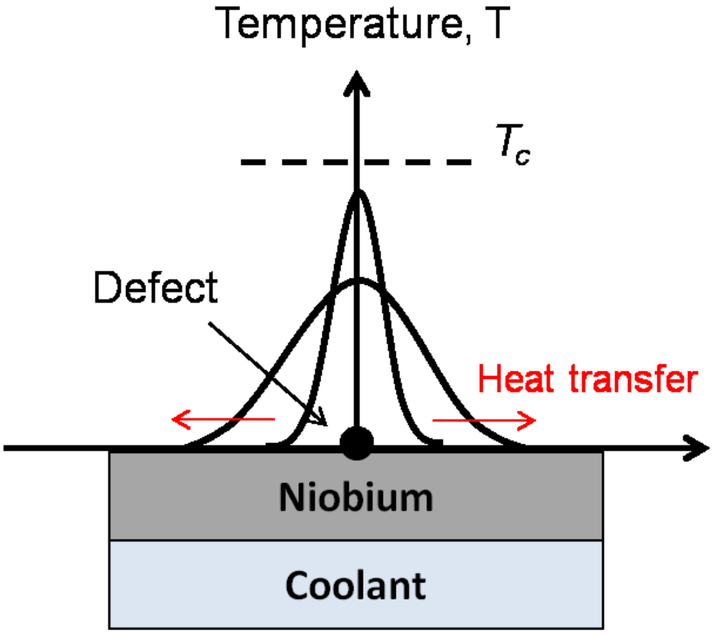

Figure 1.5 Temperature profile around a defect in the cavity surface [4]

Even though other limitations have been solved, the primary limitation that has been the main factor for researchers in the recent years is field emission (which is also somewhat related to multipacting), in which electrons are emitted from the surface by high surface electric fields. Under low electric fields electrons inside a metal cannot be emitted because of an electrostatic potential well. As electric field increases, however, electrons may tunnel the potential well resulting from the reduced work function. These emitted electrons impact elsewhere on the cavity surface resulting in heating the surface and increasing the surface resistance. Hence, field emission can lead to thermal breakdown resulting from the temperature increase. Several researches using thermometry show that the origin of this field emission is associated with the surface contaminants [26]. Therefore, surface cleaning is an important step in cavity processing.

High pressure water rinsing and assembly in a vacuum system are used to reduce emission sites and improve cavity performance. In addition, some other efforts including vacuum firing, RF processing, and helium processing continue [27].

1.1.3 Fabrication of superconducting RF cavities

An EB welding technique is the most common and well-established technique for the elliptical cavity fabrication. The process for a fabrication of cavities consists of two steps: deep drawing of half cells and EB welding of the deep drawn half cells. Figure 1.6 show deep drawn half cells and the EB welded cavities.

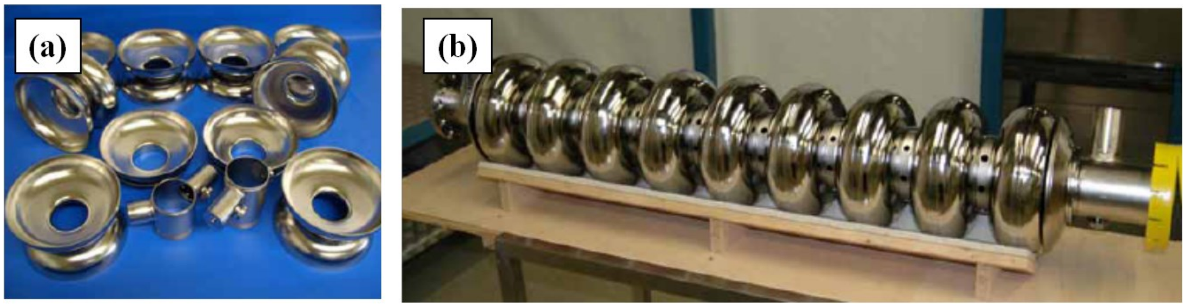

Figure 1.6 (a) Deep drawn half cells and (b) assembled EB welded cavities [18]

However, this technique may cause some problems that limit the cavity performance. Welding provides opportunities for the formation of defects such as an inclusion of a foreign material and topological surface imperfections, figure 1.7. Since the magnetic field is concentrated near equatorial weld of the cavity, the welded region is a major concern of surface defects leading to a quench [28].

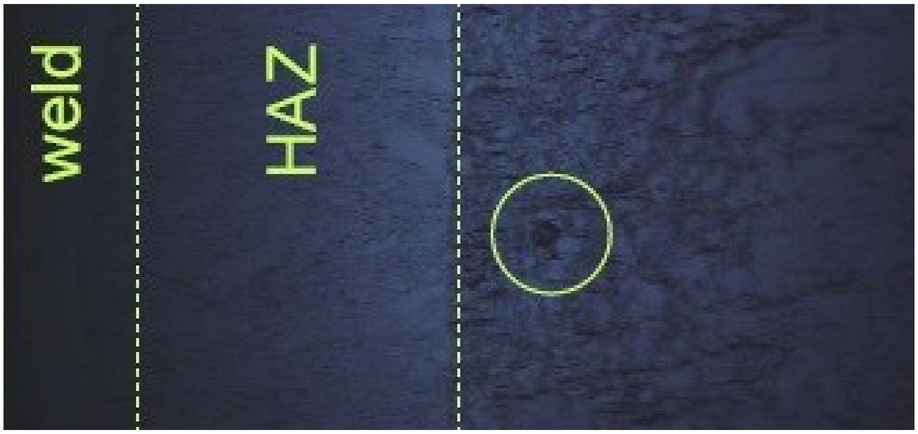

Figure 1.7 Defects near the welded region and the heat-affect zone (HAZ) of the cavity surface [28]

In recent years advanced cavity treatment techniques including electropolishing permitted accelerating gradients to approach the theoretical limit. However, higher accelerating fields and drastic reductions in resonator production time and costs are needed for the further development of more powerful accelerators.

In order to overcome the multitude of problems associated with EB welding techniques, seamless techniques for cavity fabrication have been sought. Non-welded (seamless) fabrication methods have two advantages: 1) the seamless cavity prevents the risk of equatorial weld contamination; 2) a potential cost reduction can be obtained. By eliminating the welding region, the risk of contamination in the welded and heat affected zones (HAZ) can be avoided. In addition, less scattering in the performance statistics of seamless cavities compared to welded cavities is to be expected. Finally, the resource-intensive surface treatment process can be reduced, and hence cost of fabrication can be reduced.

The development of several seamless techniques mostly for the Teraelectronvolt Energy Superconducting Linear Accelerator (TESLA) shape cavity has taken place at Istituto Nazionale di Fisica Nucleare (INFN) by V. Palmieri (spinning) [29] and Zolotukhin (spinning) [12], and at Deutsches Elektronen-Synchrotron (DESY) by W. Singer (hydroforming) [14]. Among them, the feasibility of seamless Nb-cavity hydroforming as a fabrication method has been demonstrated at DESY and High Energy Accelerator Research Organization (KEK) [19]. The typical procedure of hydroforming for cavity fabrication consists of two stages: 1) reduction of the tube diameter in the iris area, and 2) expansion of the tube diameter in the equator area. Figure 1.8 (a) shows the tubes in each stage. The developed technology allows the fabrication not only of single cells but also multi-cell cavities from Nb and bimetallic Nb/Cu. Figure 1.8 (b) shows an example of a hydroformed double cell cavity [15].

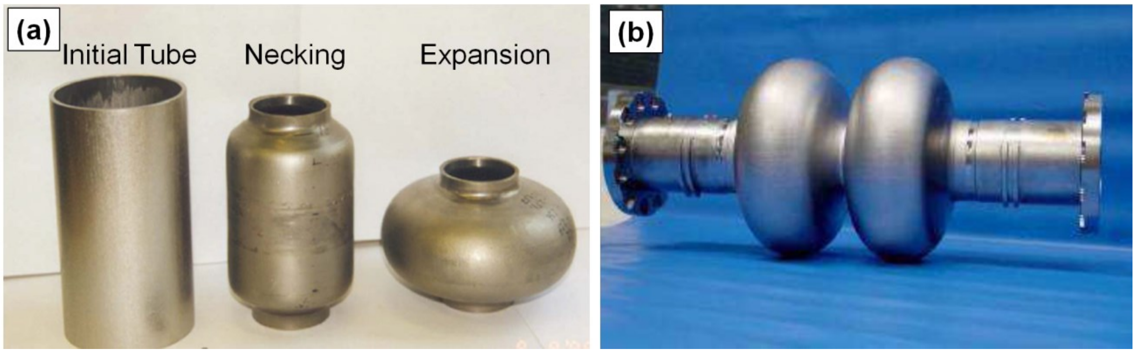

Figure 1.8 (a) The tube shape variation [19] and (b) first Nb double cell cavity produced at DESY by hydroforming [15]

Although the main technical problems of the fabrication of seamless single cells and multi-cells by hydroforming have been empirically solved, fundamental analysis in terms of formability relating to the microstructure is still incomplete.

1.2 Hydroforming techniques

Hydroforming is a forming process using a pressurized fluid (liquid or gas) in place of hard tooling in order to plastically deform a blank material for a desired shape. Since 1990s, it has been widely researched for various industrial fields, especially for automotive industries. An increasing demand for producing low-mass vehicle to achieve fuel saving and reduced emission leads to a continuing interest in hydroforming techniques. With a hydroforming technique, part consolidation and reduced post-forming processes (e.g. welding and piercing) can be achieved [30-35]. In this section, general research areas for hydroforming technique will be addressed.

1.2.1 Classification of hydroforming

The hydroforming process generally can be categorized: (a) sheet hydroforming, (b) tube hydroforming, as depicted in figure 1.9 [33].

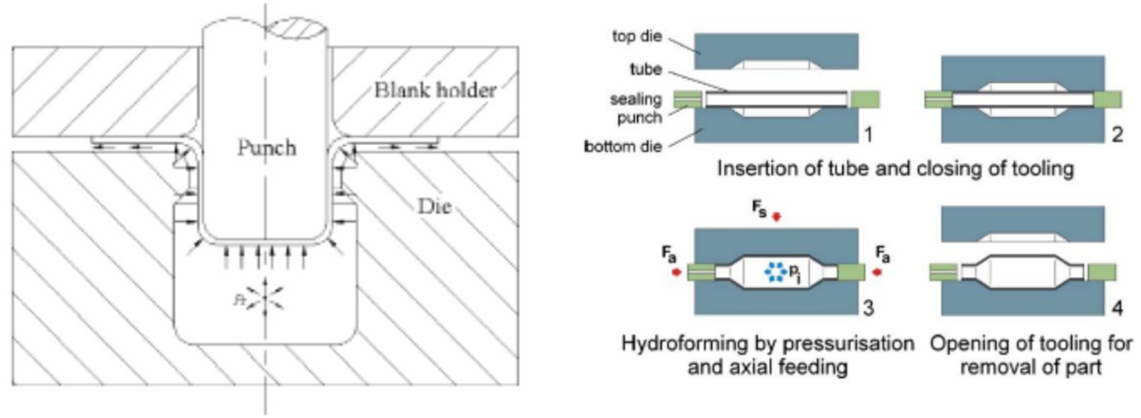

(a) (b)

Figure 1.9 Principle of Hydrofroming: (a) Sheet hydroforming [33] and (b) Tube hydroforming [32].

For the sheet hydroforming, sheet blank is formed by hydraulic pressure inside the die cavity. The process of this technique is similar to deep drawing. However, the main difference is the existence of the counter pressure on the opposite side of the punch. When the punch is moved to the blank, the die cavity filled with liquid medium is compressed, resulting in applying the counter pressure to the blank. During this process, the fluid medium will flow out between the die and blank, which allows to the reduction in friction force. It contributes to the deeper draw allowing fabrication of the blank with more complex shape. Second, tube hydroforming is a forming process of tubular materials using simultaneous application of internal pressure inside of tube and axial compressive forces from tube ends. The internal pressure is applied by filling a fluid medium inside the sealed tube with hydraulic pump. When internal pressure is applied, axial loading is also applied using sealing punch and hydraulic cylinder in order to feed the blank. Among these two conventional hydroforming technique, tube hydroforming technique is utilized for SRF cavity fabrication because of its axisymmetric shape.

1.2.2 Hydroforming design parameters

In order to obtain the desired final form of blank without failure using the hydroforming technique, several parameters should be considered. The parameters to consider for hydroforming process generally consist of three classes: 1) tube parameters, 2) process control parameters, and 3) tooling parameters [35].

First, the tube parameter includes the dimension of tube blank, materials, and their properties. Especially, the normalized material properties do not depend on the dimension are most important to determine other parameters. The material properties include: modulus of elasticity, yield strength, poison ratio, ultimate tensile strength, uniform elongation, percent elongation, work hardening exponent, plastic strain ratio (r value), flow stress curve, and so on. In order to evaluate these properties, there are several methods including tensile test and bulge test.

Control of forming loads is another of important parameters avoiding failures such as wrinkling, buckling and bursting. The loading history of the internal pressure (P_i) and axial force (F_a) are process control parameters for tube hydroforming process. The internal fluid pressure acts as the bulging pressure, which pushes the tube blank into the internal surface of the die. Therefore, the bulging pressure should be sufficient to form the local shape of the blank. The axial loading is used for preventing wall thinning. These two parameters should be considered together. Improper ratio of these parameters usually causes the failure of the process. An excessive axial loading, for example, may cause instability due to wrinkling, whereas local thinning resulting from excessive tensile force may be occurred when an axial loading is not sufficient. Researches relating to the loading path are highly connected to the numerical simulations. In order to obtain the optimal loading path for an appropriate criterion (e.g. thickness distribution), a series of simulations are conducted using trial and error method [36]. An adaptive approach is also proposed to reduce the number of simulations [37, 38]. This approach determines the loading path from one single simulation by modifying the load at the end of each increment during single simulation.

The third parameter is the tooling conditions: shape, surface finish, and hardness. The tooling includes die holders, dies, inserts, punches, and sealing systems. These tooling should have general requirements because of high pressure system: 1) high strength enough to endure stresses due to large internal pressure and axial loading, 2) good surface finish to reduce friction force, and 3) flexibility by interchangeable inserts. Especially, the surface finish is highly related to the process control parameters because the friction force should be properly considered to determine the axial force. Therefore, lubrication is also an important factor to consider.

1.2.3 Instability

Improper design of hydroforming parameters causes failures where equilibrium state of stress and strain between applied force and the resistance of the material cannot be maintained. There are mainly three forming limits of tube hydroforming: buckling, wrinkling, and bursting as depicted in figure 1.10 [39]. Buckling and wrinkling failures can be occurred when an excessive axial compressive force is applied. Buckling failure is observed on the tube with relatively long length and thick walls (i.e. low *D*/*t* ratios) during the beginning stage of the forming process, whereas wrinkling occurs on both long and short tubes with relatively thin walls (i.e. high *D*/*t* ratios) during both the initial and intermediate stages. Bursting failure is an irrecoverable failure mode different from previous limits. This failure is caused by local thinning of tube wall when an excessive tensile force is applied because of insufficient axial loading or inhomogeneity of material properties and dimensions. Separation or splitting usually follows due to the extreme deformation in the bursting area. An important issue is the prediction of the forming limit and bursting pressure for tube hydroforming, which provides guidelines for product designers and process engineers. Therefore, various researches have been conducted to investigate the effects of hydroforming parameters such as loading condition, die geometries and material parameters on the instability of hydroforming process [40, 41].

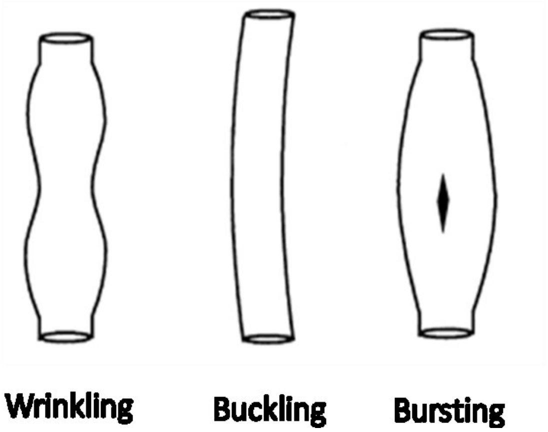

Figure 1.10 Typical failure modes

1.3 Characterization of tubular materials

Analysis of the typical hydroforming process consists of three steps: 1) determination of the material parameters of the tube material, 2) computer simulation of the forming, and 3) the hydroforming test itself. In this section, the first step is discussed. The procedures for obtaining the constitutive equation from testing with a multiaxial stress state are discussed. Numerical approaches using the obtained data are reviewed in the next section.

The material's parameters are critical to obtaining the final form without failure. Among them, an accurate constitutive equation (i.e., the relationship between stress and strain) of the material to be formed is essential to determine the force and work requirements of the forming process in which the plastic deformation is dominant. This relationship can be usually obtained from the true stress-strain curve from the tensile test with uniaxial stress state. However, in most forming and cutting processes, deformation takes place under complex states of stress. Therefore, it is necessary to define the equivalent or effective stress-strain relationship to represent all combinations of stress. For this purpose, a yield criterion, enabling consideration of all the combinations of stresses that will produce plastic flow, should be established first. Therefore, several theories have been proposed to predict the yield condition under multiaxial stresses. Each theory is based on a different hypothesis about material behavior. In what follows the yield criteria and testing method for determining the effective stress-strain curve were reviewed.

1.3.1 Yield criterion

The yield criterion defines the condition for the limit of elastic behavior or the onset of plastic flow in a material. In order to determine the yield conditions under multiaxial stresses, a relationship between the principal stresses is required. Each theory is based on a different hypothesis about material behavior. In this review, two yield functions are described: the von Mises [42] and Hill's 1948 quadratic [43] yield functions for isotropic and anisotropic materials, respectively.

The common assumptions for the yield criteria of most isotropic materials are as follows: First, the yield strength in tension and compression are identical, which means that the Baushinger effect can be ignored. The second assumption is that volume is conserved during deformation. Finally, the plastic deformation is associated with slip mechanisms; this implies that the shear stress rather than the normal stress is dominant [44].

The yield condition for isotropic materials should be identical regardless of any reference basis. Therefore, the yield condition can be expressed with the stress invariants of principal stresses (σ_i). Since the plastic deformation is independent of the mean stress (hydrostatic pressure), the yield condition can be expressed in terms of deviatoric stress components (σ_i'), which are given by

$$\sigma_1' = \sigma_1 - \frac{\sigma_1 + \sigma_2 + \sigma_3}{3}, \quad \sigma_2' = \sigma_2 - \frac{\sigma_1 + \sigma_2 + \sigma_3}{3}, \quad \sigma_3' = \sigma_3 - \frac{\sigma_1 + \sigma_2 + \sigma_3}{3}. \quad (1\text{-}8)$$

The von Mises criterion assumes that yielding occurs when the second invariant of the stress (*J₂'*) in terms of deviatoric stress components exceeds a critical value. Therefore, the yield criteria can be expressed mathematically as

$$J_2' = -(\sigma_1'\sigma_2' + \sigma_2'\sigma_3' + \sigma_1'\sigma_3') = \frac{1}{6}\left[(\sigma_2-\sigma_3)^2 + (\sigma_3-\sigma_1)^2 + (\sigma_1-\sigma_2)^2\right] = k \quad (1\text{-}9)$$

where *k* is the arbitrary constant. Therefore, the von Mises function is given by

$$(\sigma_2-\sigma_3)^2 + (\sigma_3-\sigma_1)^2 + (\sigma_1-\sigma_2)^2 = k \quad (1\text{-}10)$$

where the factor of 1/6 has been incorporated into the arbitrary constant, *k*. Figure 1.11 is the von Mises yield surface in two-dimensional space for the same value of yield strength, σ_y.

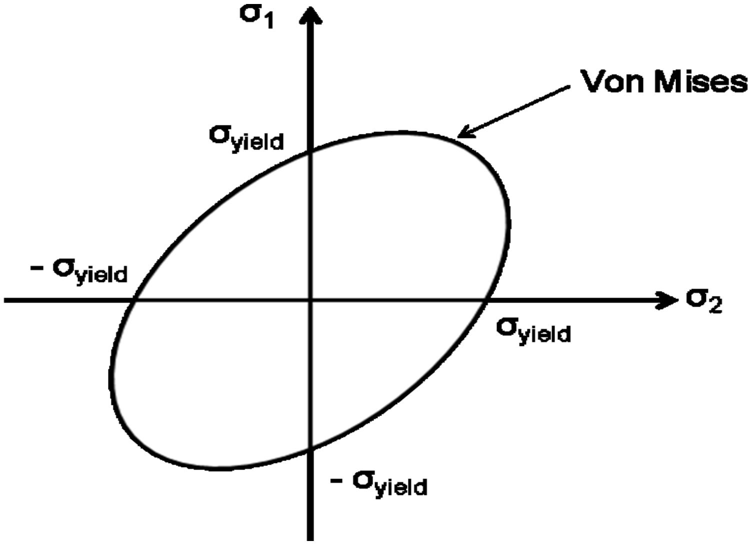

Figure 1.11 Yield locus for von Mises

In case of the anisotropic materials, Hill's quadratic yield function is usually used because of its simplicity. It is a simple extension of the von Mises function, which can be expressed in terms of principal stress components in the form:

$$F(\sigma_2 - \sigma_3)^2 + G(\sigma_3 - \sigma_1)^2 + H(\sigma_1 - \sigma_2)^2 = 1 \tag{1-11}$$

where *F, G,* and *H* are material constants defining the degree of anisotropy. When *F*=*G*=*H*=1/2, Hill's quadratic yield function is identical to the von Mises one. The material constants have relationships with yield stresses in the principal axes as follows:

$$\frac{1}{X^2} = G + H,\ \frac{1}{Y^2} = H + F\ ,\ \frac{1}{Z^2} = F + G \tag{1-12}$$

where *X, Y,* and *Z* are the yield stresses in the *x*, *y*, and *z* directions, respectively.

After one determines the shape of the yield surface by the form of the equation, it is necessary to evaluate the value of the arbitrary constant, *k*, which represents the size of the yield surface determined by experimental results. For this reason, the stress state of the tensile test ($\sigma_1 = \sigma_y$ and $\sigma_2 = \sigma_3 = 0$) is usually substituted into the yield functions. In this case, the yield stress in tension is defined as an effective stress ($\bar{\sigma}$) representing all of the combinations of stress by conjunction with the form of the yield surface [44-47].

Using the von Mises yield criterion the effective stress for the isotropic materials can be obtained as follows:

$$\bar{\sigma} = \frac{1}{\sqrt{2}}\left[(\sigma_2 - \sigma_3)^2 + (\sigma_3 - \sigma_1)^2 + (\sigma_1 - \sigma_2)^2\right]^{1/2}. \tag{1-13}$$

For Hill's quadratic yield function, the effective stress can be also expressed as

$$\bar{\sigma} = \sqrt{\frac{3}{2}}\left[\frac{F(\sigma_2 - \sigma_3)^2 + G(\sigma_3 - \sigma_1)^2 + H(\sigma_1 - \sigma_2)^2}{F + G + H}\right]^{1/2}. \tag{1-14}$$

After the effective stress is determined, one needs to relate multiaxial strain increments to an equivalent or effective strain increment ($\bar{\varepsilon}$) in a uniaxial tensile test.

Two theories are used to define the effective strain increment: the normality rule and the principle of equivalent plastic work.

The ***normality rule*** is invoked to connect the yielding with the strain increments for building a constitutive equation. As the strains for elastic deformation are described by Hooke's law, there are similar relations for plastic deformation, called the flow rules. It is mathematically written as

$$d\varepsilon_i = d\lambda \frac{\partial f}{\partial \sigma_i} \tag{1-15}$$

where $d\lambda$ is an arbitrary constant and f is the yield surface.

The other principle used for the determination of the effective strain increment is the ***equivalent plastic work*** definition which means that the plastic work done in 1-D is equivalent to the plastic work done in a general state. Therefore, the work done per unit volume in any process can be expressed as

$$\frac{dW}{vol.} = \int_0^{\bar{\varepsilon}} \bar{\sigma} d\bar{\varepsilon} = \sigma_1 d\varepsilon_1 + \sigma_2 d\varepsilon_2 + \sigma_3 d\varepsilon_3. \tag{1-16}$$

Using equation (4.8) and (4.9), the required effective strain increment can be obtained by substitution of the effective stress.

The effective strain increment for von Mises can be derived as

$$d\bar{\varepsilon} = \left[\frac{2}{3}\cdot\left(d\varepsilon_1{}^2 + d\varepsilon_2{}^2 + d\varepsilon_3{}^2\right)\right]^{1/2}. \tag{1-17}$$

In a monotonic, proportional process, equations (4.10) can be written in the integrated form with the equivalent strain ($\bar{\varepsilon}$) substituted for the incremental strain ($d\bar{\varepsilon}$) as

$$\bar{\varepsilon} = \left[\frac{2}{3}\cdot\left(\varepsilon_1{}^2 + \varepsilon_2{}^2 + \varepsilon_3{}^2\right)\right]^{1/2}. \tag{1-18}$$

For Hill's quadratic yield function, the effective strain can be also expressed as

$$\bar{\varepsilon} = \sqrt{\frac{2}{3}}(F+G+H)^{1/2} \cdot \left[\frac{F(G\varepsilon_2 - H\varepsilon_3)^2 + G(H\varepsilon_3 - F\varepsilon_1)^2 + H(F\varepsilon_1 - G\varepsilon_2)^2}{(FG+GH+HF)^2} \right]^{1/2} . \quad (1\text{-}19)$$

After effective stress-strain relationships are determined, these two parameters are related to each other through the expression of the form

$$\bar{\sigma} = K \cdot \bar{\varepsilon}^{n} \quad (1\text{-}20)$$

where K is the strength coefficient, and n is the strain hardening coefficient. These equations represent the constitutive relationship of materials and also use for simulation program.

1.3.2 Testing method

The most common method to evaluate material parameters is the tensile test in which a sample is subjected to uniaxial tension up to failure. The tensile test yields the stress–strain curve and hence the elastic modulus, yield stress, ultimate tensile strength, uniform elongation, elongation at fracture, strength coefficient, and straining hardening coefficient. These fundamental properties determine the formability and guide the process design.

For the tubular materials, a specimen in a longitudinal direction parallel to the tube axis is directly taken from the tube wall. In addition, it is also necessary to evaluate the characteristics of the tube material in the circumferential direction where much of the expansion during hydroforming occurs. Material which has identical properties in any direction is defined as being isotropic. However, most tubular materials are fabricated by rolling or extrusion and are consequently anisotropic due to texture developed during the fabrication process. Anisotropic properties are evaluated in terms of plastic strain ratios (*r* values) [48], which is defined as the ratio of width strain to thickness strain ($\varepsilon_w / \varepsilon_t$). Therefore, *r* value is

$$r = \frac{\ln(w / w_0)}{\ln(w_0 l_0 / wl)} \tag{1-21}$$

where w_0 and w are the initial and final width, while l_0 and l are the initial and final gage length. The direction of the *r* value is defined as the angle between the rolling direction and the axis of specimen. For example, the *r* values of specimens cut along the rolling, diagonal and transverse directions are r_0, r_{45} and r_{90}, respectively. In case of tube, the rolling direction is replaced by axial direction.

Several research works have been based on Nb the most common superconducting cavity material. The flow stresses of Nb over a broad range of temperatures and strain rates were evaluated by Nemat-Nasser *et al.* [49] and Byun *et al.* [50]. Jiang *et al.* [51] also investigated the influence microstructure in terms of texture and grain size on the mechanical properties of high residual resistance ratio (*RRR*) Nb. They confirmed that the mechanical properties of polycrystalline high *RRR* Nb revealed strong anisotropy. Zamiri *et al.* [52] obtained the mechanical properties of high purity Nb sheets from both tensile and balanced biaxial bulge tests. They also measured *r* values as a function of the strain showing that *r* value is very sensitive to the plastic deformation due to the presence of an unstable texture. These results were obtained from samples cut from the sheet material and although they provide useful information on the deformation behavior of Nb they cannot be directly applied to the tubular materials.

Although the tensile test is the simplest route towards a quantitative measure of formability it is not directly applicable to tubular materials. First, a flattening process for the specimen in the circumferential direction is required which would influence the mechanical characteristics. In addition, biaxial force is acting on the tube under hydraulic pressure for hydroforming, in contrast to tensile deformation under an applied uniaxial force. Hence results from uniaxial tensile test alone are not enough to evaluate the mechanical properties of tubular materials for hydroforming. More details regarding the various states of stress are required to obtain more accurate deformation behavior of tubular materials.

With the goal of improving the characterization of tube materials for hydroforming application, several research effort have been carried out using hydraulic tube bulge testing in which hydraulic pressure is applied to the inside of sample tube. Analysis of the resulting data leads to the constitutive relationships. Tube materials are placed under multiaxial stresses during the bulge test. Therefore, based on measurements of internal pressure, bulge height and wall thickness analytical methods are applied to determine the flow stress curves of the tubular materials. Several analytical models with an approximation of stress and strain have been proposed to obtain flow stress curve. In section 3.3, the verification of these analytical models was discussed.

1.4 Finite element analysis

1.4.1 Continuum model

Computer simulation is widely used to predict the deformation behavior and design process parameters because of its time and cost efficiency. Most hydroforming simulations are performed using commercial simulation program based on finite element method (FEM) such as ABAQUS, PAM-STAMP, and LS-DYNA. Using these FE simulations, it is possible to obtain a new process or optimize the design of the hydroforming process without the burden of experimentation. This approach can be used to simulate the process with various process parameters and schemes. From these series of simulations, proper structure design and process parameters can be determined prior to physical experimentation. Hence, a reduction of production costs and time consumption can be expected. Therefore, computer simulations are used increasingly to verify and modify the initial process design.

Continuum numerical simulation model considers the mechanical behavior of materials modeled as a continuous mass rather than as discrete particles. Therefore, it requires parameters describing the microscopic process inside the mass. The most important parameter is the constitutive equation which represents the stress-strain relationship obtained by experiments (e.g, tensile test, bulge test). Continuum numerical simulations of hydroforming of tubular materials show two main aspects. First, the method for determining the loading path (i.e., axial feeding) has been investigated [38, 53]. In this case, the axial forces for axial feeding acts at the both tube ends. Therefore, the choice of loading path is important to obtain the final form without wrinkling or buckling. The second aspect is related to the use of correct material laws and parameters including flow curve and anisotropic properties. This review focused on this second aspect. Altan et al. [54] compared simulation results using the obtained flow stress curve from both the bulge and tensile tests with the experimental results. This showed that the simulation results with flow curve from a bulge test are more accurate. Hwang et al. considered anisotropic properties of materials during numerical simulation using Hill's yield function [55]. These results showed that the accuracy of simulation increased by considering anisotropic properties. However, a discrepancy between simulation and experimental results still exists. Zamiri et al. constructed a model considering anisotropy using the evolutionary yield function for biaxial bulge test [56, 57]. This model verified that the evolutionary anisotropic coefficients of Hill's yield function are necessary to properly model the plastic behavior of the Nb sheet. Ahn et al investigated the numerical simulation model of ferritic stainless steel sheet using various yield functions [43, 58, 59] by conducting cylindrical cup drawing and biaxial bulge test [60]. However, these results cannot be directly applied to the tube bulge tests. Based on this approach, it is necessary to verify these models for the tube bulge test.

1.4.2 Crystal plasticity

Since early 1900s, crystal plasticity theories have been studied to find the relationship between the macroscopic properties of polycrystalline materials and the fundamental mechanical behavior of single crystals caused by dislocation movement through the crystal lattice. The main interest is the prediction of mechanical properties and texture evolution of polycrystalline materials by formulating the relations between the macroscopic and microscopic behaviors. Some theories have been proposed to define this relationship by simplifying the deformation behavior of polycrystalline materials. Sachs [61] and Taylor [62] started with polycrystal plasticity. The Sachs and Taylor models assume uniform stress and strain in all grains, respectively. Therefore, in the case of the Sachs model, the equilibrium condition between grains is satisfied while the kinematic compatibility condition is not satisfied. The Taylor model, assuming uniform deformation within grains, satisfies the compatibility condition but violates equilibrium conditions. Later theories were able to satisfy both equilibrium and compatibility [63-65]. Strain heterogeneities allowed for the relaxed constraint model. For a self-consistent model, each grain is regarded as an inclusion in a homogeneous and isotropic elastic body [66].

Strain gradient models have been introduced to simulate a length-scale mechanical behavior of materials by using the strain gradient and its work. [67-70]. Therefore, it is convenient for application to continuum mechanics problems. However, it ignores crystal structure, grain boundary structure, and slip systems. Therefore, it is impossible to predict Hall patch effect. This model was developed by many researchers including Evers [71] and Arsenlis [72, 73].

Finite element analysis using crystal plasticity (CP-FEM) has been developed by Peirce, Asaro and Dawson. [74-76]. CP-FEM is based on the single crystal constitutive equations. In CP-FEM, the equilibrium and compatibility is considered in a finite element sense. In addition, interactions between neighboring grains are considered. Peirce et al.

[74, 75] proposed an integration of crystal plasticity into non-linear formulations. This makes it possible to predict the texture evolution and strain distribution under various boundary conditions [77]. Researches also focused on approaches considering the relationship between one finite element and a given grain. Kalidindi considers one finite element as many grains using Taylor iso-strain [78-80], and Peirce [81, 82] regards one element as a single grain and a small part of one grain.

This study discussed tube hydroforming using the CP-FEM modeling using a PAN based CP model [74, 83] in order to include the anisotropic properties of materials. Peirce, Asaro, and Needleman, proposed a model that provides latent and self-hardening, which resolved shear stress has a higher initial hardening and saturated as shown in figure 1.12. The details of the kinematics follow in chapter 5.

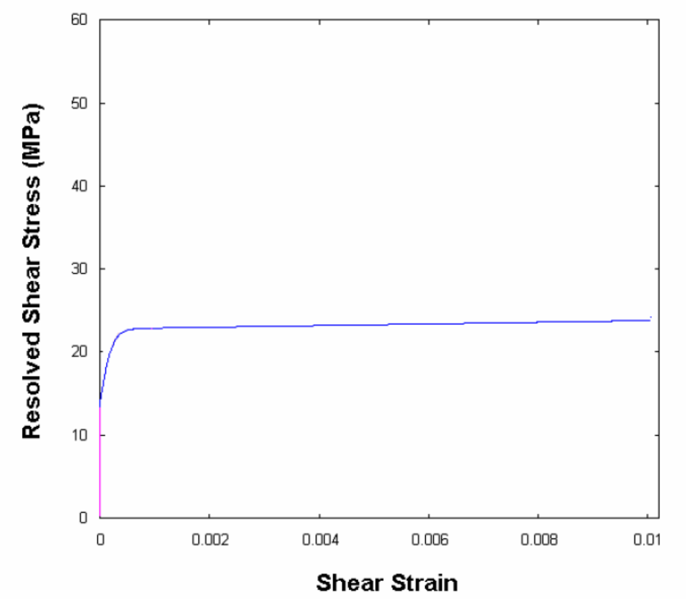

Figure 1.12 Peierce, Asaro & Needleman (PAN) model [84]

This model can consider the evolution of orientation during deformation as well as the anisotropy of tubes in all directions and under various loading conditions. Therefore, it is more attractive for the hydroforming of tubular samples into SRF-relevant shapes which involve a more complex geometry (a bulged tube) and loading conditions. However, there are few research efforts using CP-FEM for actual real size forming process including tube hydroforming [85] because the computing time for this detailed replication of hydroforming is very high. In this study we demonstrate a multi-scale simulation approach which uses both microscopic CP and macroscopic continuum models. In this approach the CP model was only used for determining the flow stress curve under biaxial loading. Continuum FE analysis of tube hydroforming using the obtained constitutive equation from the CP modeling was then performed. In principle, it is expected to allow high quality predictions of the deformation under hydroforming of Nb tubes based on their known texture and tensile tests, without the need of bulge test experimentation, using a fast simulation approach. The demonstration of this approach is then discussed based on the experimental data from the tensile, bulge test and microstructural analysis.

1.5 Summary

With a goal of development of a numerical simulation model, this work focuses on the characterization of tubular materials and numerical analysis. It includes:

1) Heat treatment of tube materials

    - Heat treatment of high purity Cu, Cu alloy, and Nb tubes, and analysis of the microstructure (orientation)
    - Measurement of the *RRR* values for evaluation of the purity of the materials
    - Determining of the heat treatment condition without degradation of electrical properties

2) Determination of the constitutive equation of OFHC Cu, Cu alloy and Nb tubes
    - Tensile and bulge testing of OFHC Cu, Cu alloy and Nb tubes
    - Verification of the analytical models
    - Obtaining the effective stress-strain curves from the tensile and bulge test
    - Considering the anisotropic properties using various yield functions
3) Construction of the numerical simulation model
    - Construction of a continuum simulation model for both isotropic and anisotropic materials
    - Construction of a CP simulation model using orientation information
    - Demonstration of a the multi-scale simulation approach using both continuum and CP simulation models

For the bulge testing of tubular materials, pre-deformation heat treatment may be necessary because tubular materials especially show the high stiffness and anisotropic properties due to the fabrication process. Therefore, heat treatment may be required to increase the formability. Therefore, the influence of heat treatment on microstructure and the mechanical properties needs to be investigated. The variation of electrical properties (i.e. *RRR*) during heat treatment was also investigated. Based on these efforts, the optimal heat treatment conditions were determined in order to obtain both high formability and *RRR* value.

Two different numerical simulation models were constructed to predict the deformation of heat treated tube materials under hydraulic pressure. The first model is the continuum model using the constitutive relationship as an input of the model. In order to obtain accurate prediction, an accurate constitutive equation is needed for the continuum model. Therefore, the constitutive relationship of tubular materials was determined using tube bulge tests. Previous studies showed that the tube bulge test is able to obtain more accurate flow stress curve than a tensile test can. However, no results with superconducting cavity materials (e.g., high purity Cu and Nb) exist. Therefore, tube bulge tests using these materials were performed. There are various analytical models which can be used to obtain the flow stress curve from the bulge test results. These models will be explored in terms of their ability to obtain accurate results. There are two main requirements for obtaining an accurate flow stress curve. The first one is the measurement of the axial radius of the bulge, and the other is the proper choice of yield function to consider the anisotropic properties. Hence, various approaches for considering these factors were investigated.

The second numerical simulation model for the hydroforming of a cavity was a multi-scale simulation model using both continuum and CP elements. The CP model using the information from the microstructure (i.e. orientation) can account for anisotropic properties and their evolution during deformation, which may lead to a more accurate prediction of deformation. However, the CP model is hard to use for a tube bulge problem because of complex geometry and large deformation. Although it can be solved, the computation time is large. Therefore, this study discussed the multi-scale simulation approach using both continuum and CP-FEM models. The detail of the experimental procedure and numerical simulation strategy follows:

Test Sample Preparation and Characterization: Samples removed from OFHC Cu tube were annealed at The Ohio State University (OSU) after which it was determined that the conditions corresponding to maximum tensile plasticity were characterized by maximum *RRR*, and minimum randomly oriented grain size. Samples removed from Nb tube were heat treated at the Fermi National Accelerator Laboratory (FNAL), according to prior experience, in preparation for tensile testing. Constitutive (stress-strain) relationships were derived from the tensile results.

Bulge Testing: The results of the tensile tests (above) were evaluated and optimally heat treated lengths of OFHC Cu, Cu alloy and Nb tubes were subjected to hydraulic bulge testing. Constitutive (stress-strain) relationships were derived from the bulge-test results. Stress-strain curves based on the tensile- and bulge-test measurements were plotted and compared.

Numerical simulation: Figure 1.13 shows the simplified flow chart illustrating the simulation strategy in this study. Two different simulation models were constructed to simulate the hydroforming process. The first model is the macroscopic continuum model using the constitutive equations (stress- strain relationship) as an input of the simulation. For a macroscopic simulation approach, two constitutive equations were obtained from the experimental process including tensile and tube bulge tests in order to investigate the influence of loading condition on deformation behavior.

As a multi-scale simulation approach, the CP-FEM model was also constructed as well as the continuum model. First, the constitutive equation of material was obtained from the microscopic simulation model (CP-FEM) using the microstructural information (i.e., orientation). For a CP model, the simple cubic shaped model was constructed reduce the computing time instead of the replicating of actual bulge test. This simplified model was only used for determining the flows tress curve. In order to increase the accuracy, the flow stress curve under biaxial force was determined to replicate the actual stress state during the bulge test. The obtained flow stress curve from the mentioned CP model was then used as an input for the continuum simulation model. The final simulation results were compared to the experimental results.

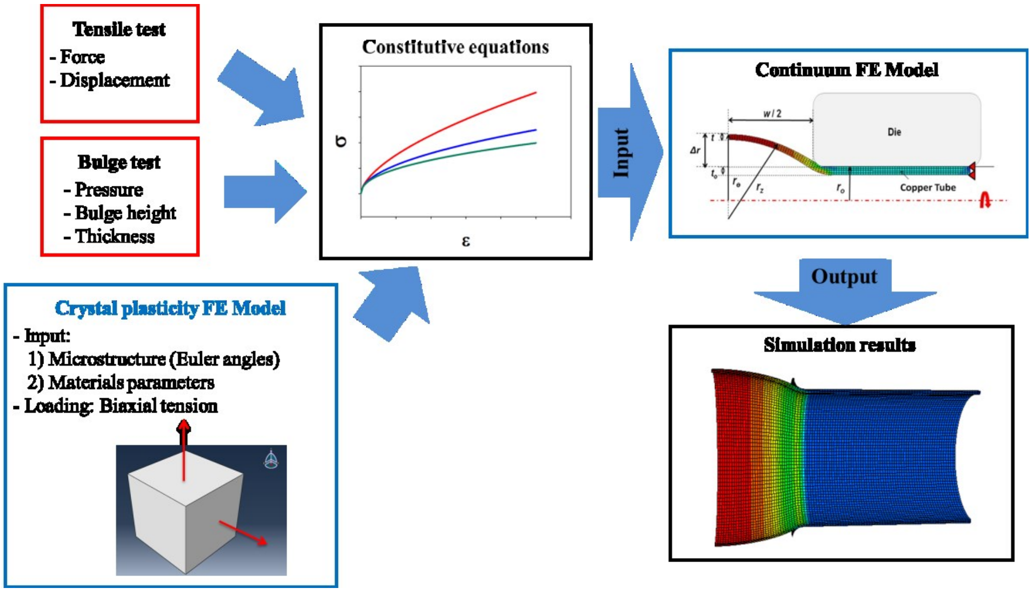

Figure 1.13 Simulation strategy for hydroforming of tubular materials

CHAPTER 2: SAMPLE PREPARATION AND CHARACTERIZATION

2.1 Materials

For a series of experiment including tensile and bulge tests, three different tubular materials were used: 1) oxygen free high purity Cu (OFHC), 2) reactor grade Nb and 3) copper alloy tubes. Figure 2.1 shows the picture of Cu and Nb tubes used in this experiment. Table 2.1 specifies the dimensions of the tube samples. The samples were heat treated to increase formability. Characterizations were performed in terms of the mechanical and electrical properties as well as microstructure of the materials. Mechanical and electrical properties were evaluated by tensile test and *RRR* measurement, respectively. The orientation image mapping (OIM) was used for microstructural analysis. Euler angles were extracted from the OIM image for CP-FEM. Table 2.2 describes the summary of materials, testing, and numerical simulation analysis performed in this study.

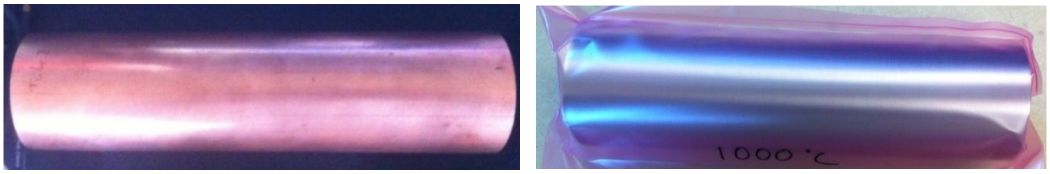

(a) (b)

Figure 2.1 Pictures of tubular materials: (a) OFHC Cu and (b) Nb

Table 2.1 Summary of the dimension of tube materials

Length [mm]	Outer radius [mm]	Wall thickness [mm]
240	31.75	1.65

Table 2.2 Summary of materials, experiments, and numerical simulations performed in these studies

Material	Heat treatment condition	Experiment				Numerical simulation	
		RRR	Tensile test	OIM	Bulge test	Continuum	Continuum +CP
OFHC Cu	2h/300°C	O	O	O	X	X	X
OFHC Cu	2h/400°C	O	O	O	X	X	X
OFHC Cu	2h/500°C	O	O	O	O	O	X
OFHC Cu	2h/600°C	O	O	O	X	X	X
OFHC Cu	2h/700°C	O	O	O	X	X	X
Nb	3h/800°C	O	O	O	X	O	O
Nb	2h/1000°C	O	O	O	O	O	O
Nb	3h/800°C+2h/1000°C	X	O	O	X	O	O
Nb	2h/1000°C X 3	X	O	O	X	O	O
Cu alloy	1h/500°C	X	O	O	O	O	X
Cu alloy	1h/600°C	X	O	O	O	O	O

O: performed in this study
X: not performed in this study

2.2 Preparation

2.2.1 OFHC copper

From a long piece of OFHC Cu tube purchased from ThyssenKrupp Materials, three types of samples were fabricated: (i) 240 mm long tubes for bulge testing (figure 2.1), (ii) standard “dog-bone” style segments, 50 mm gauge length, for tensile testing as shown in figure 2.2 [86] and grain size measurement, and (iii) wire segments, 100 mm long, for *RRR* measurement. The samples were heat treated (HT) in flowing argon gas for 2h at 300 ~ 700°C (heated up at 5°C/min and furnace cooled) using OSU’s 3 in. Lindburg tube furnace for the tubes and a 2 in. Thermdyne Corporation tube furnace for the smaller samples.

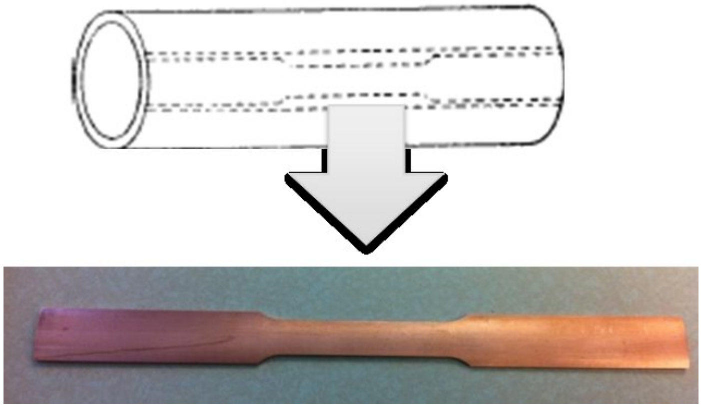

Figure 2.2 Standard “dong-bone” style segment [86]

2.2.2 Reactor-grade niobium

Eight pieces of “Reactor-grade” Nb tube 240 mm long, 63.5 mm OD and 1.65 mm wall thickness were purchased from the Firmetal Co., Ltd., Shanghai, China. The analysis of the Nb tube is given in Appendix A. In preparation for bulge testing, tensile testing, grain size and *RRR* measurement several pieces of tube along with some tensile-test samples were heat treated for 3h/800°C and 2h/1000°C, respectively. Some samples were heat treated multiple times to increase the formability. One sample was first heat treated for 3h/800°C and then heat treated for 2h/1000°C ("3h/800°C+2h/1000°C"). The other sample was heat treated three times of 2h/1000°C ("2h/1000°C X3"). The heat treatments were performed at the Fermi National Accelerator Laboratory (FNAL) under the guidance of Dr. L. D. Cooley.

2.2.3 Copper alloy

Copper alloy was used for verifying the procedure considering anisotropic properties of tube material. Therefore, the longitudinal and transverse samples for the tensile test were cut from the tube with ASTM-standard dimensions. The longitudinal sample is identical to the "dog bone" style segment for OFHC and Nb samples. The transverse sample was taken from the flatten specimen taken from the ends of the tube as shown in figure 2.3. The samples were heat treated for 1h at 500 and 600°C, respectively. The samples heat treated for 1h/500°C and 1h/600°C were used for the continuum simulation and CP-FEM, respectively. In order to consider the anisotropy effects, the strains in the width direction were measured at five different strains (loading direction) of 0.1, 0.15, 0.2, 0.25 and 0.3 during tensile tests, and the ratios of width strain to thickness strain (*r* values) were determined by taking into account the condition of volume constancy for each longitudinal and transverse sample.

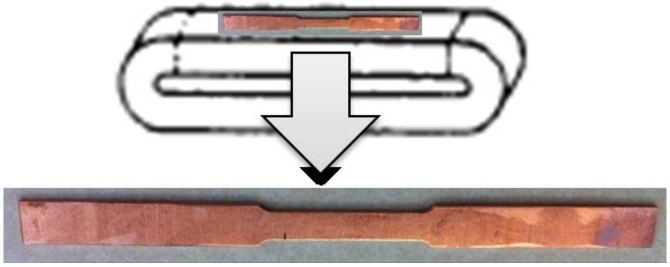

Figure 2.3 Tensile test sample in transverse direction [86]

2.3 Characterization

2.3.1 OFHC copper

RRR measurement: It is well known that metallic purity, solid solution strengthening, and electron scattering (electrical resistivity) are closely related [87-89]. Thus it is expected that a metal's ductility will increase along with its residual resistance ratio, $RRR = R_{273K}/R_{0K} = R_{273K}/R_{4.2K}$. The latter was measured using the standard four-point technique while the wire sample was dunked alternately into ice-water and liquid He. Figure 2.4 shows *RRR* versus 2 h HT temperature rising to a maximum at 500°C as $R_{4.2K}$ passes through a corresponding minimum, presumably in response to a minimization of intragrain electron-scattering-center concentration. It has been suggested that during the initial stages of HT impurities migrate to the grain boundaries [90] while during grain growth at higher HT temperatures (see below) they migrate back into the grains [91] which would account for an increase in resistivity. A similar curve of *RRR* versus HT temperature and an explanation in terms of the precipitation and redissolution of impurities has been offered by Fickett [92].

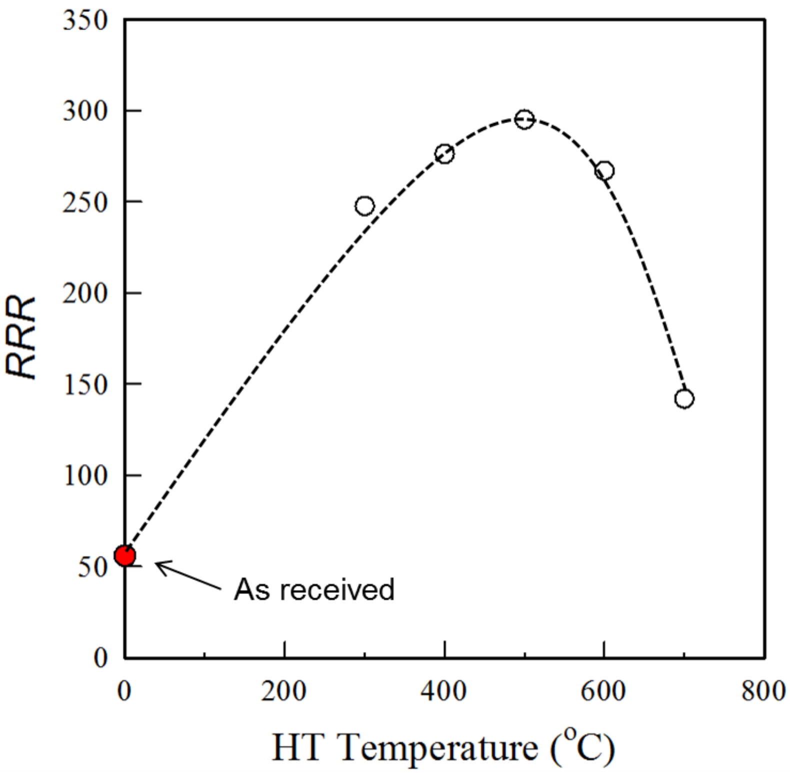

Figure 2.4 *RRR* as f unction of 2 h heat treatment temperature for OFHC Cu

As an intermediate cooling step between 273 K and 4.2 K the sample may be immersed in liquid nitrogen which provides an opportunity for examining the use of a new resistance-ratio metric, herein designated $rr = R_{273K}/R_{77K}$. Figures 2.5 (a) and (b) demonstrate that *rr* which also maximizes at 500°C is directly related to *RRR* according to $RRR = 0.001 \cdot \exp(1.604 \cdot rr)$ within $50 < RRR < 300$, a useful range of values.

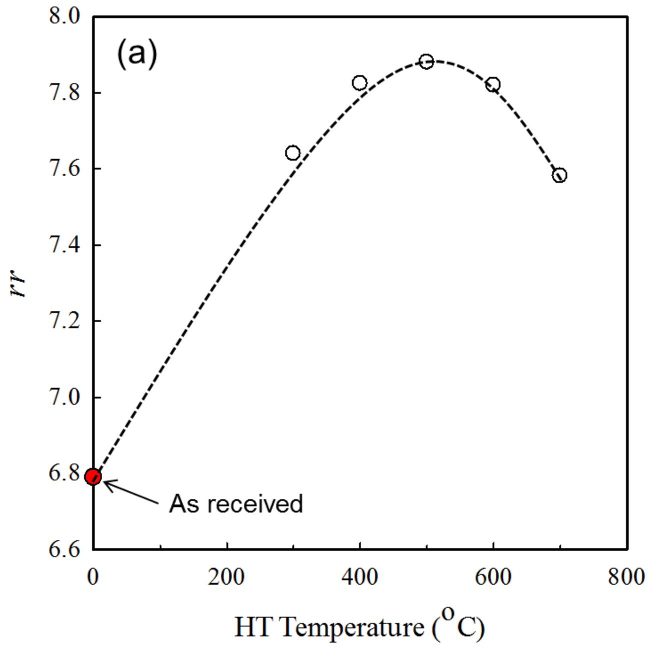

(a)

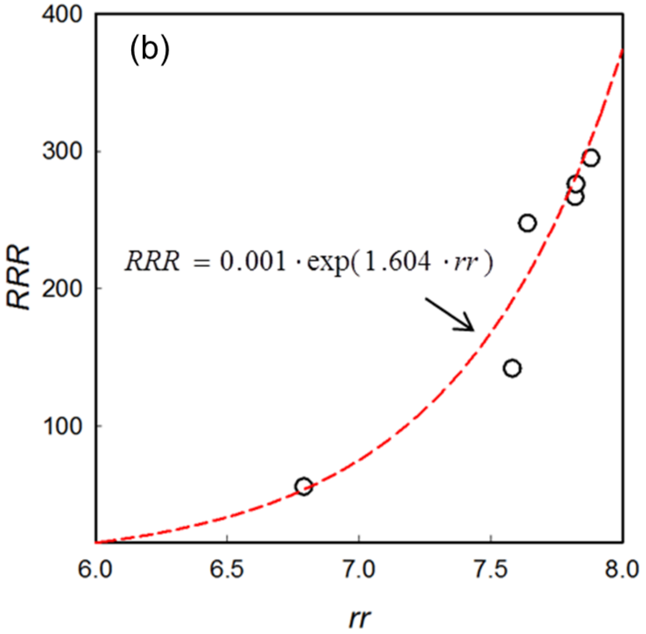

(b)

Figure 2.5 (a) *rr* as function of 2 h heat treatment temperature for OFHC Cu and (b) *RRR* versus *rr* within about 50<*RRR*<300 for heat treated OFHC Cu

Microstructure: The microstructures of the OFHC samples were examined using OIM. Following standard procedures, surface grinding started with 320 grit SiC paper and continued through 1200 grit. The sample was then polished using 6 μm, 1 μm, and 0.05 μm abrasives and etched using the 1:1:1 (volume) mixture of ammonium hydroxide, and hydrogen peroxide (3%), and distilled water. Post polishing with colloidal silica was performed using a vibratory polisher. During HT the as-received elongated cold-worked grain structure quickly begins to recrystallize, figure 2.6. The small increase in grain size up to 500°C is followed by a rapid increase above that temperature, figure 2.7.

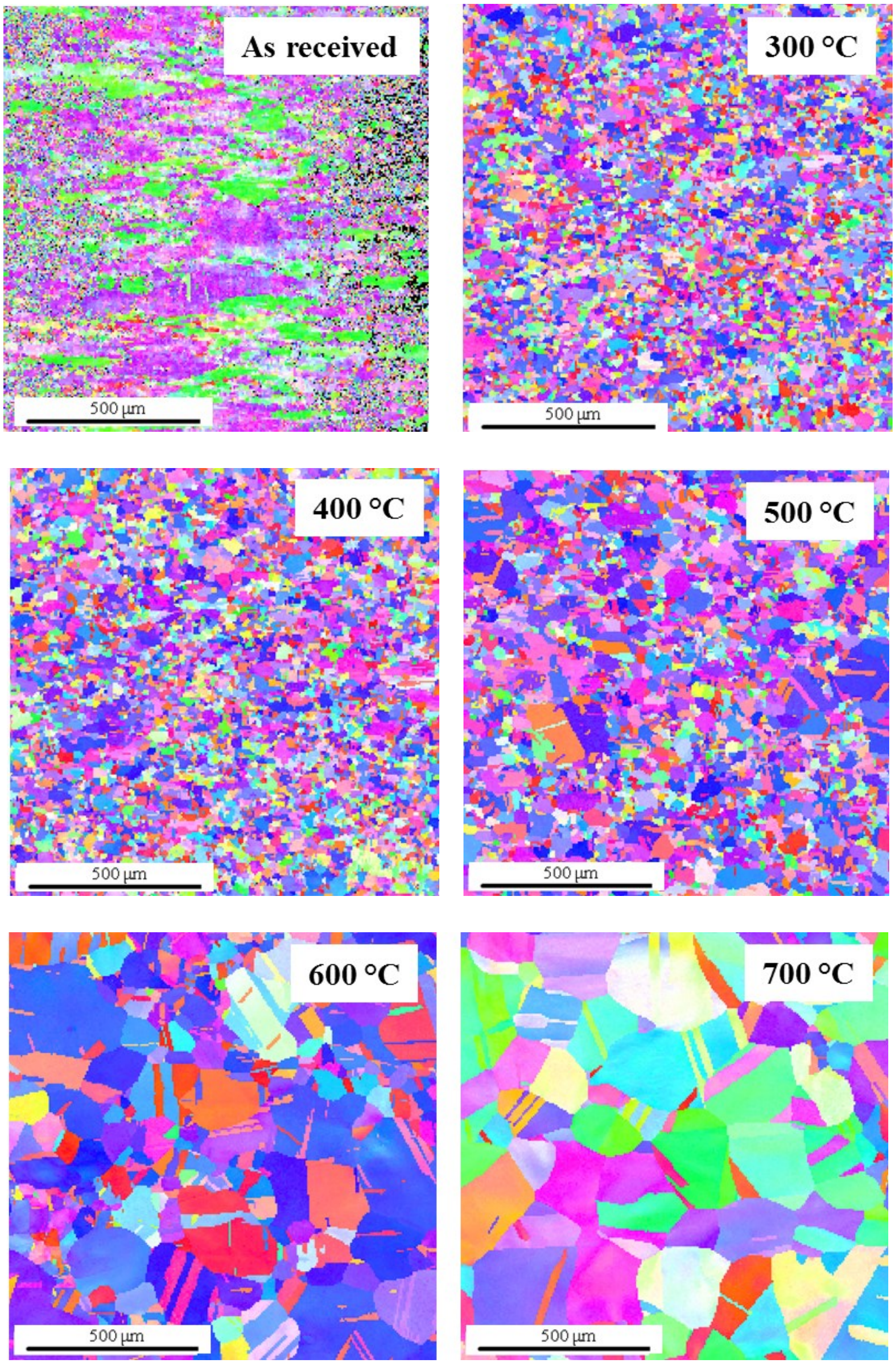

Figure 2.6 OIM micrographs of heat treated OFHC Cu

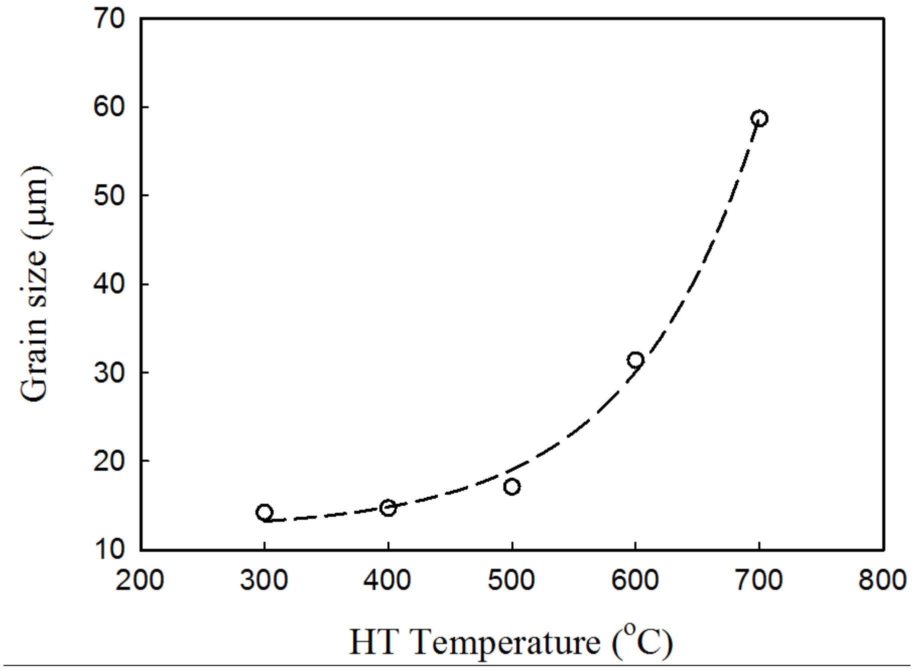

Figure 2.7 Grain size of OFHC Cu as function of 2 h HT temperature

Tensile testing: For tensile testing a standard specimen was cut from a tube wall parallel to the tube axis. Mounted in an MTS tensile test machine the sample was strained at a rate of 0.002/s. The strain was measured using an MTS extensometer and data was recorded using the MTS software. The test results, in the format engineering stress versus engineering strain are plotted in figure 2.8.

The elongated cold-worked grains (figure 2.6) of the as-received material along with dissolved impurities (low *RRR*, figure 2.5) are responsible for its low ductility. Heat treatment up to 500°C results in recrystallization and a slight increase in grain size. It contributes to the improvement of formability as well as the increase of *RRR* due to the decrease of structural defects during the recrystallization. Accompanying HT above 500°C are the precipitation and re-dissolution of impurities [91, 92] resulting in solution strengthening accompanied by reductions in *RRR*. The results of the tensile tests are summarized in Table 2.3. With regard to the sample HT for 2h/500°C, the parameters of the constitutive relationship (in the Hollomon format $\sigma = K \cdot \varepsilon^n$ [93]) are $K = 573.30$ and $n = 0.578$. These values will be used for the numerical simulation.

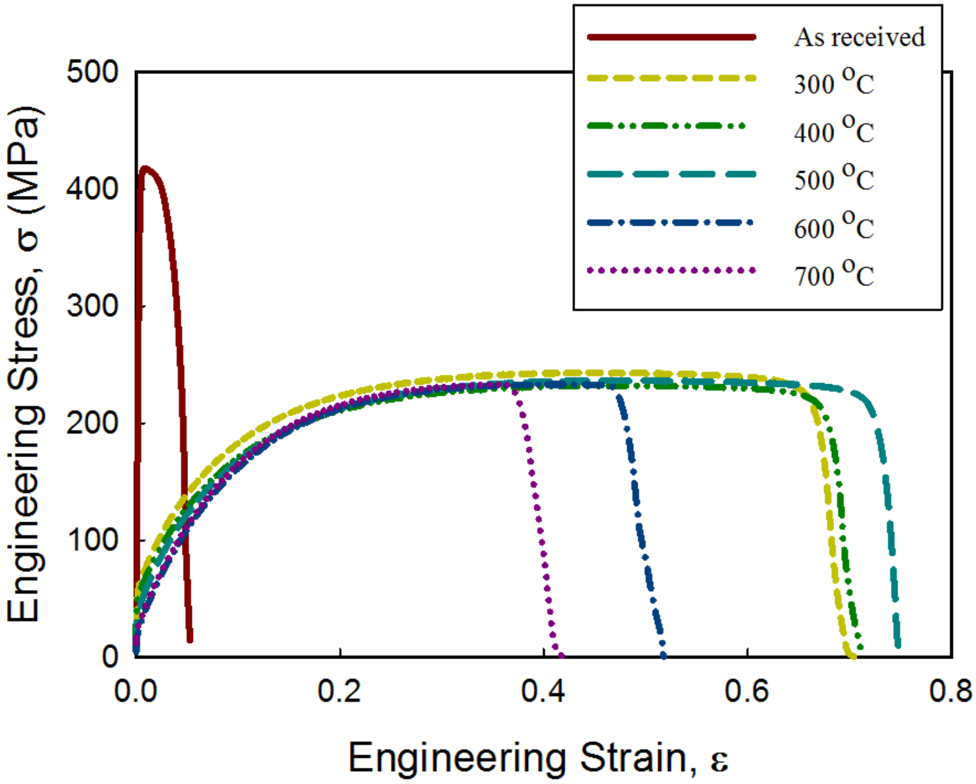

Figure 2.8 Tensile properties of OFHC Cu as-received and after HT

Table 2.3 Summary of the tensile properties of heat treated OFHC Cu

HT Temperature (°C)	Yield Strength (MPa)	Tensile Strength (MPa)	Uniform elongation	Grain Size (µm)
As received	412	417.56	0.01	-
300	60	243.34	0.46	14.2
400	53	242.41	0.46	14.7
500	38	236.77	0.49	17.1
600	23	233.56	0.42	31.4
700	27	233.40	0.35	58.7

Summary: The results of relative resistance ratio (*RRR* and *rr*) measurement, orientation imaging microscopy, grain size measurement, and tensile testing combine to show that the optimal HT need to prepare an OFHC Cu sample for bulge testing 2h/500°C.

2.3.2 Reactor-grade niobium

RRR measurement: The *RRR* measurements were made on small tensile-test type samples heat treated at 3h/800°C and 2h/1000°C, respectively. The chemical analysis provided by the vendors (Appendix A) reveals the presence of several important impurities such as: C, 30 ppm; Fe, 20 ppm; O, 10 ppm, Ni, 7 ppm. It is therefore not surprising that the as-received Nb has a *RRR* of 34 instead of the 300 usually requested for cavity-grade Nb. After a HT of 3h/800°C the *RRR* dropped to 25, as some of the impurities entered solution, and remained there even after 2h/1000°C.

Microstructure: OIM analysis was carried out on samples removed from the Nb tube. Following the above standard polishing procedure the samples were etched using a 1:1:2 (volume) mixture of nitric acid, hydrogen fluoride and hydrochloric acid. An elongated and cold-worked grain structure was observed for the as-received sample, figure 2.9. After HT, an inhomogeneous microstructure was still observed even though the samples were heat treated multiple times. The rolling process used for the fabrication of the tubes contributes to a non-uniform distribution of plastic strain through the thickness, which leads to an inhomogeneous of driving force for recrystallization. Therefore, an inhomogeneous microstructure was still observed after HT, figure 2.9. In addition, multi-step heat treatments were not effective to obtain the recrystallized microstructure. It seems that the recrystallization temperature increased with decreasing cold working during the first heat treatment. Therefore, the recrystallization process was not occurring in the subsequent heat treatment. In order to obtain a recrystallized structure, a heat treatment at higher temperatures is required.

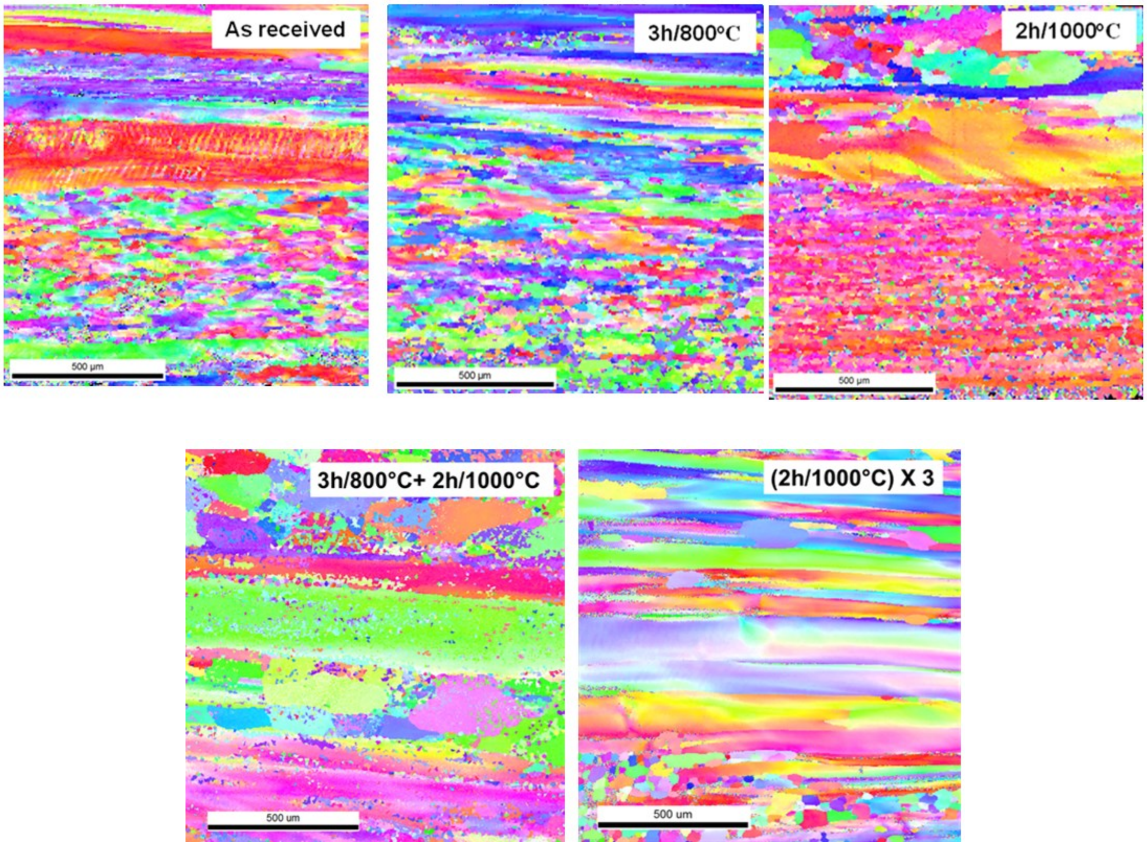

Figure 2.9 OIM micrographs of heat treated reactor-grade Nb

In order to be used for an input of CP-FEM, the Euler angles were also extracted from the OIM image. In order to reduce the computing time of CP-FEM, one thousand orientations in terms of Euler angles were selected from the measured orientations which represent the initial orientation of the sample for CP-FEM simulation. The pole figures of measured and selected orientations of heat treated Nb are shown in Figure 2.10, 2.11, 2.12, and 2.13. Highly preferred orientations were observed regardless of HT condition. In addition, there was little difference between the pole figures of measured and selected orientations, which means that the selected orientations represent the measured orientations without losing characteristic grain distribution in statistical sense.

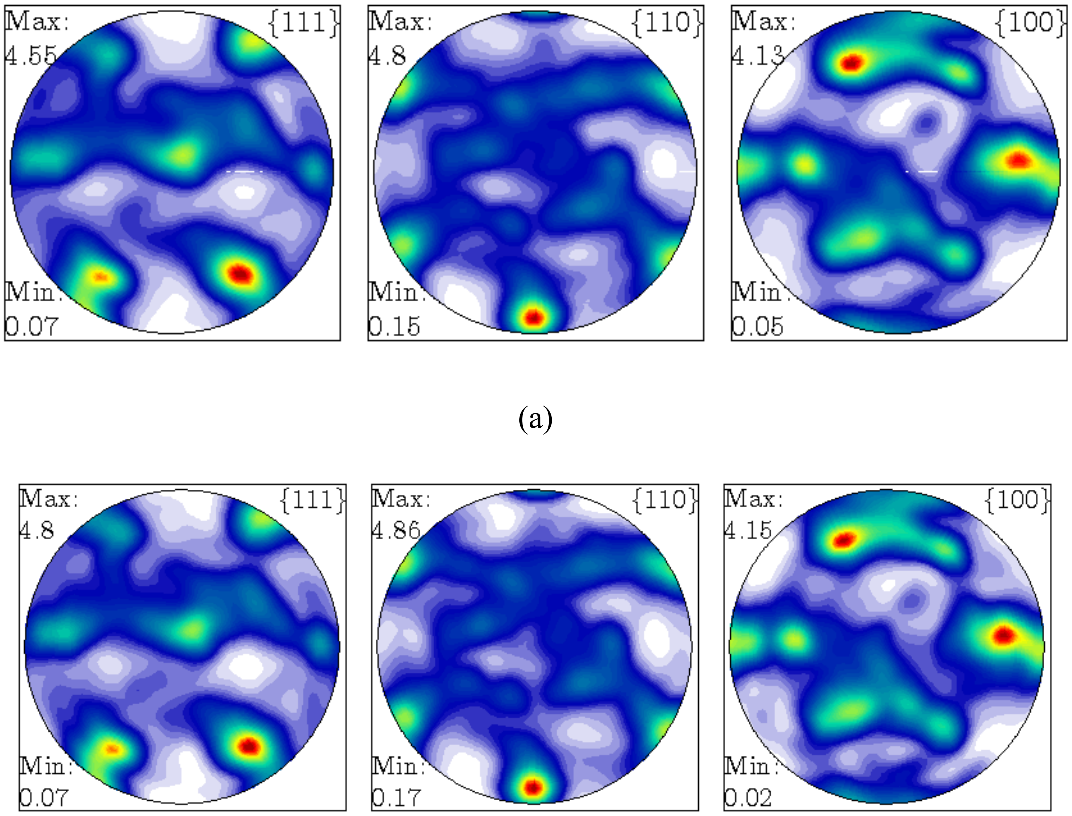

(b)

Figure 2.10 Pole figure of the Nb heat treated for 3h/800°C: (a) measured and (b) selected orientations [8]

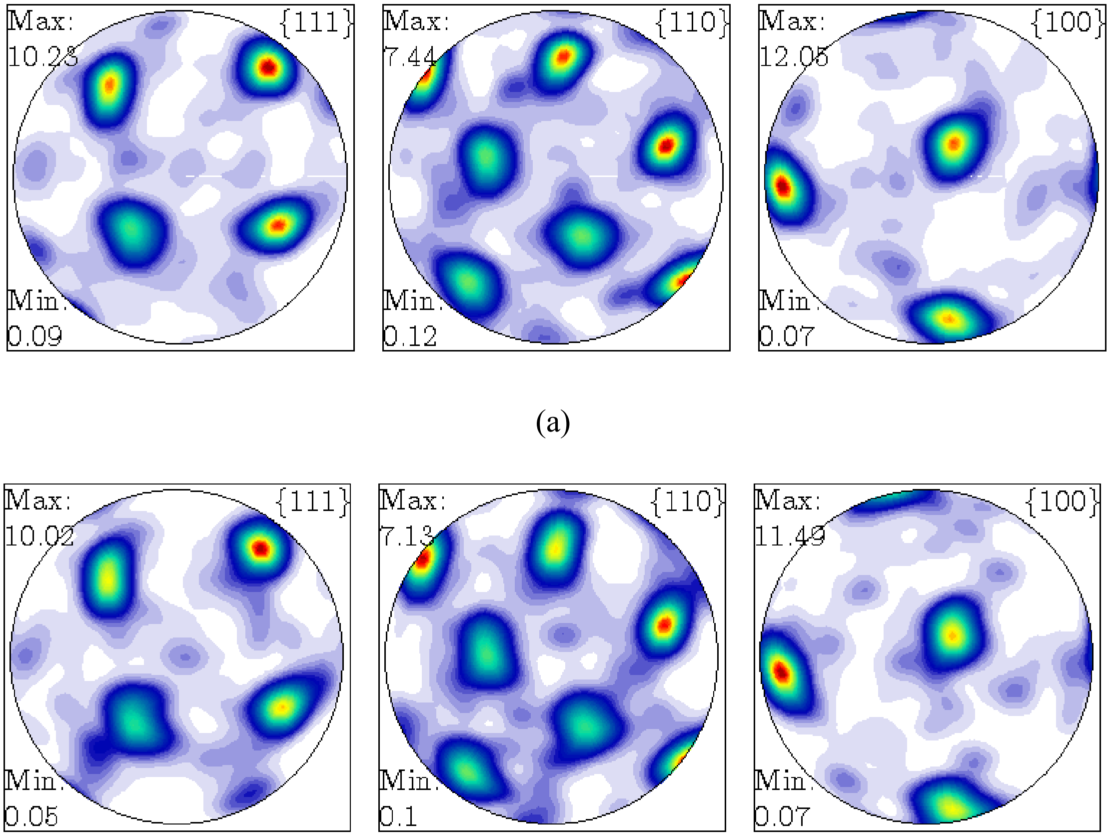

(a)

(b)

Figure 2.11 Pole figure of the Nb heat treated for 2h/1000°C: (a) measured and (b) selected orientations [8]

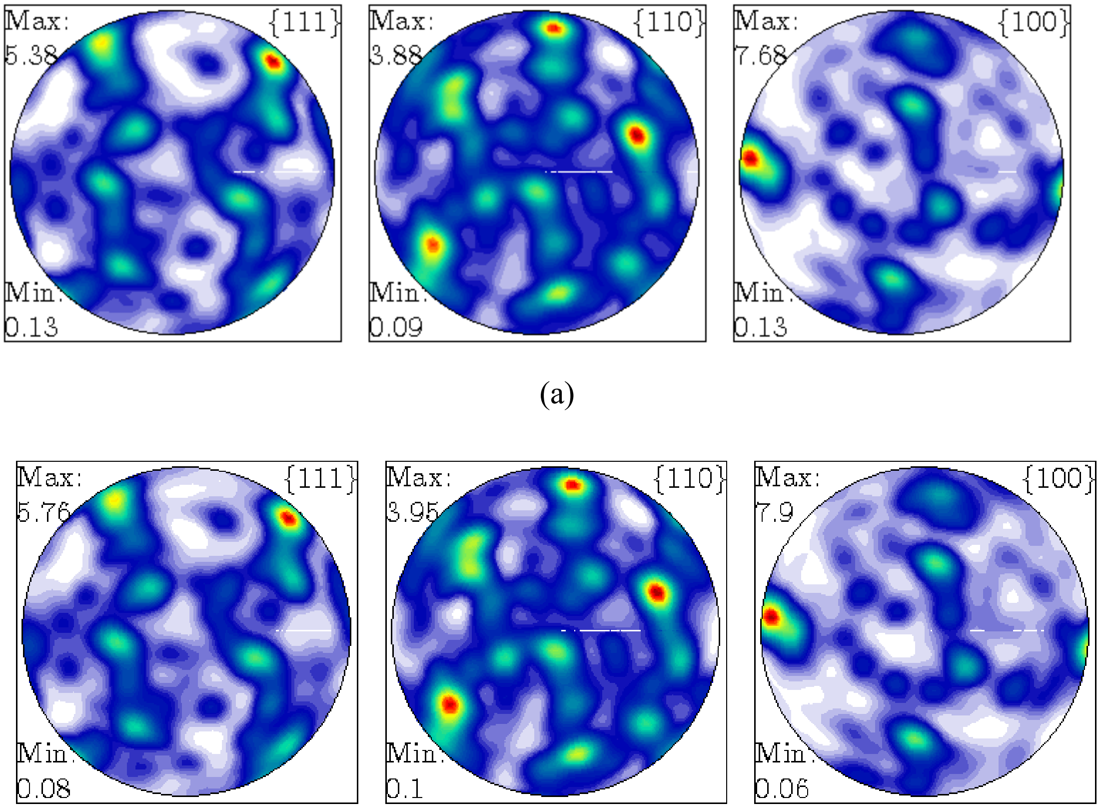

(a)

(b)

Figure 2.12 Pole figure of the Nb heat treated for 3h/800°C+2h/1000°C: (a) measured and (b) selected orientations

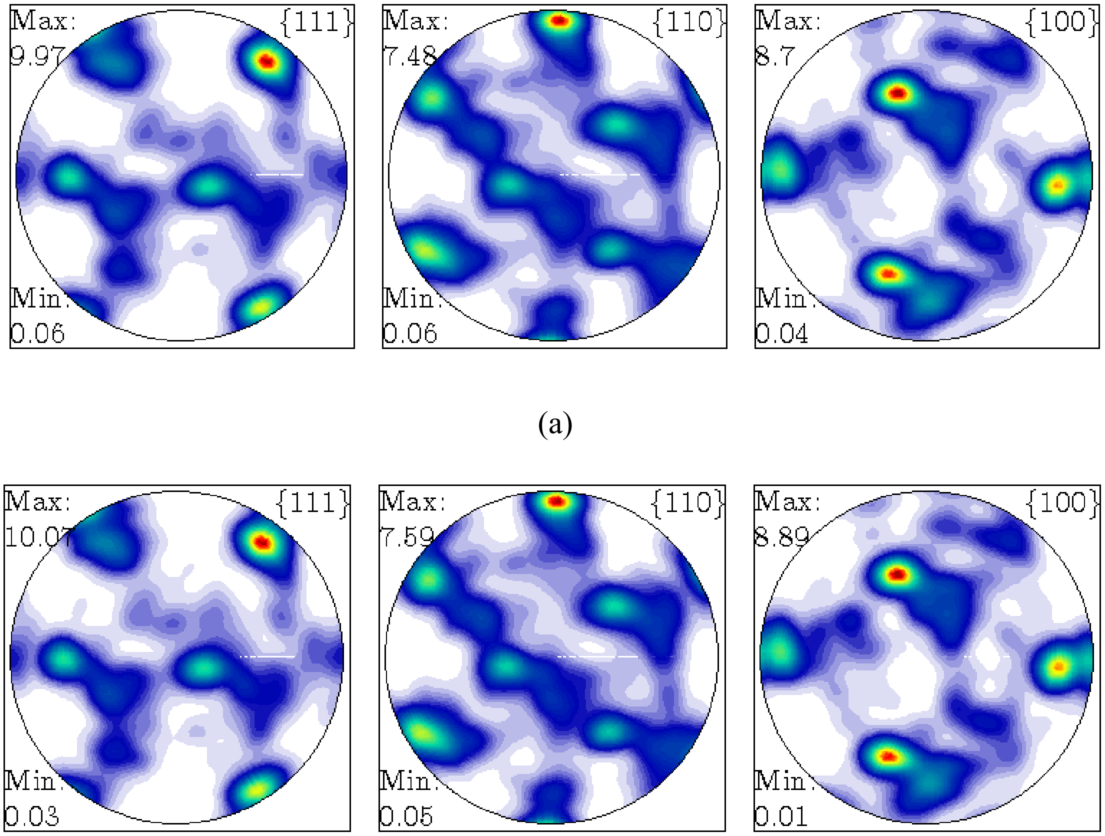

(a)

(b)

Figure 2.13 Pole figure of the Nb heat treated for 2h/1000°C X3: (a) measured and (b) selected orientations

Tensile testing: Tensile testing of the Nb samples took place at strain rates of 0.001/s and 0.005/s. The strain rate for samples heat treated for 3h/800°C and 2h/1000°C was 0.005/s while that for the other samples was 0.001/s.

The results of the tensile tests are depicted in figure 2.14 and summarized in table 2.4. The sample heat treated for 2h/1000°C X3 has highest uniform elongation. Even though the microstructure was not fully recrystallized, the partial recrystallization during multiple heat treatments contributed to the decrease of strength and increase of uniform elongation.

Summary: The results of microstructure analysis and tensile test show that the heat treatment was not good enough to obtain the high formability. The sample heat treated for 2h/1000°C was used for the bulge test. The parameters of the deduced constitutive relationship ($\sigma = K \cdot \varepsilon^n$) of true stress-strain curve for this sample are K = 314.18 and $n = 0.191$.

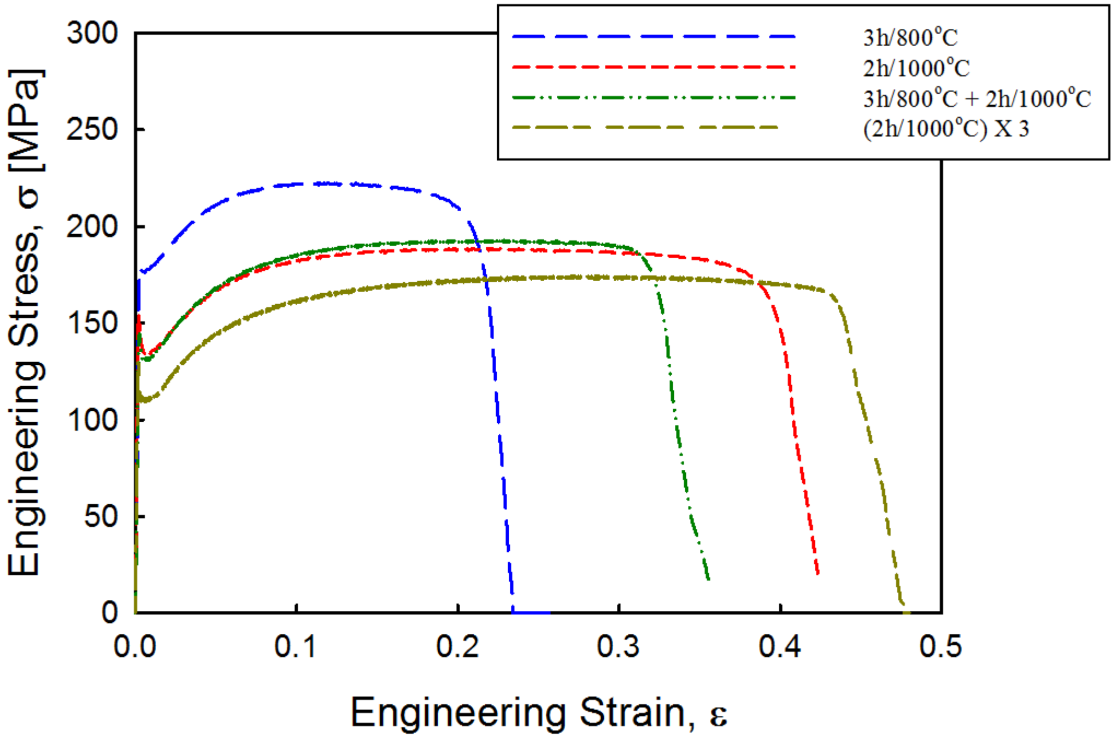

Figure 2.14 Tensile test results of reactor grade Nb

Table 2.4 Summary of the tensile properties of heat treated reactor grade Nb

HT Temperature (°C)	Yield Strength (MPa)	Tensile Strength (MPa)	Uniform elongation
800/3h	171	214	0.12
1000/2h	140	189	0.23
800/3h+1000/2h	141	193	0.23
1000/2h X 3	116	174	0.29

2.3.3 Copper alloy

Microstructure: Figure 2.15 shows the microstructures of as-received and samples heat treated for 1h/500°C obtained using optical microscopy and orientation image mapping, respectively. The elongated cold-worked grains observed in the as-received sample contributed to the low ductility. The fully recrystallized microstructure of the heat treated samples resulted in the observed increase of ductility. The average grain size of the heat treated samples was 10 μm. There was no strong preferred orientation. Figure 2.16 shows the pole figure of sample heat treated for 1h/600°C. The pole figure shows the no strong preferred orientation. The orientation information of this sample was used for CP-FEM analysis.

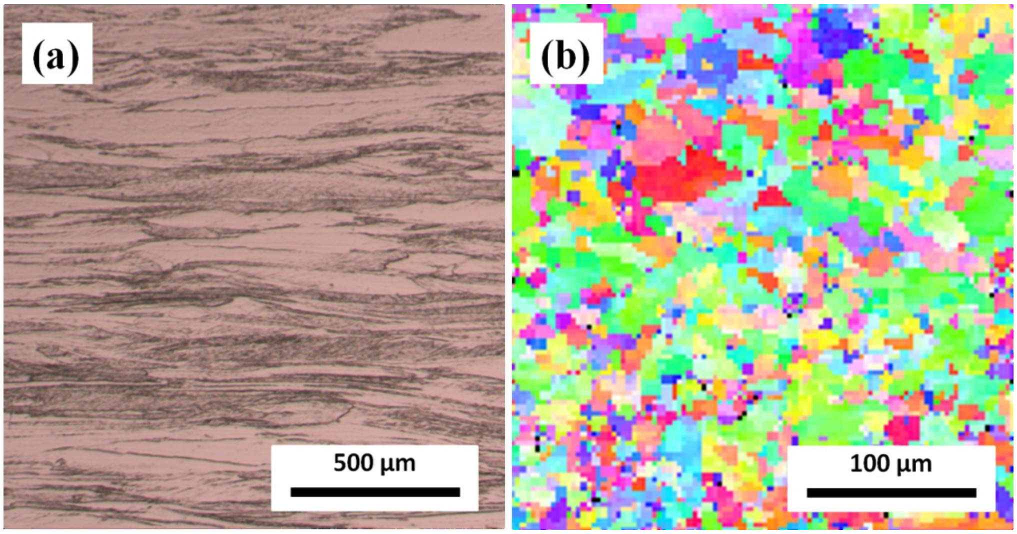

Figure 2.15 Microstructure of (a) as received and (b) Cu alloy heat treated 1h/500^{o}C

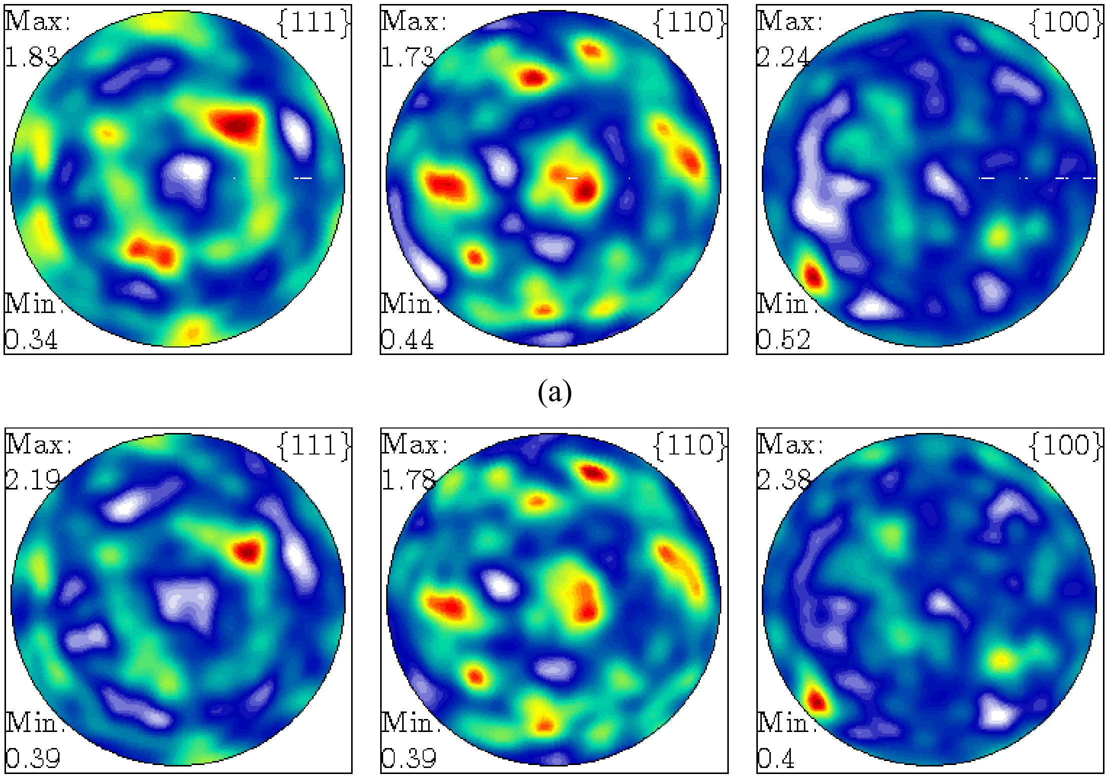

(a)

(b)

Figure 2.16 Pole figure of Cu alloy heat treated for 1h/600^{o}C: (a) measured and (b) selected orientations

Tensile testing: Figure 2.17 shows engineering stress and strain curves of samples obtained from tensile tests. The yield (σ_y) and ultimate tensile strengths (σ_{uts}) for as received sample were 420 and 437 MPa, respectively. The uniform elongation (e_u) before necking was really small (~0.01), which is not desirable for forming.

The heat treated samples had lower σ_y and σ_{uts}, but higher value of e_u. The sample heat treated at 500°C shows 64 MPa of σ_y, 242 MPa of σ_{uts}, and 0.46 of e_u. The sample heat treated at 600°C had similar value (σ_y = 50, σ_{uts} = 244, and e_u = 0.51). Table 2.5 shows the summary of the tensile properties of heat treated Cu alloy.

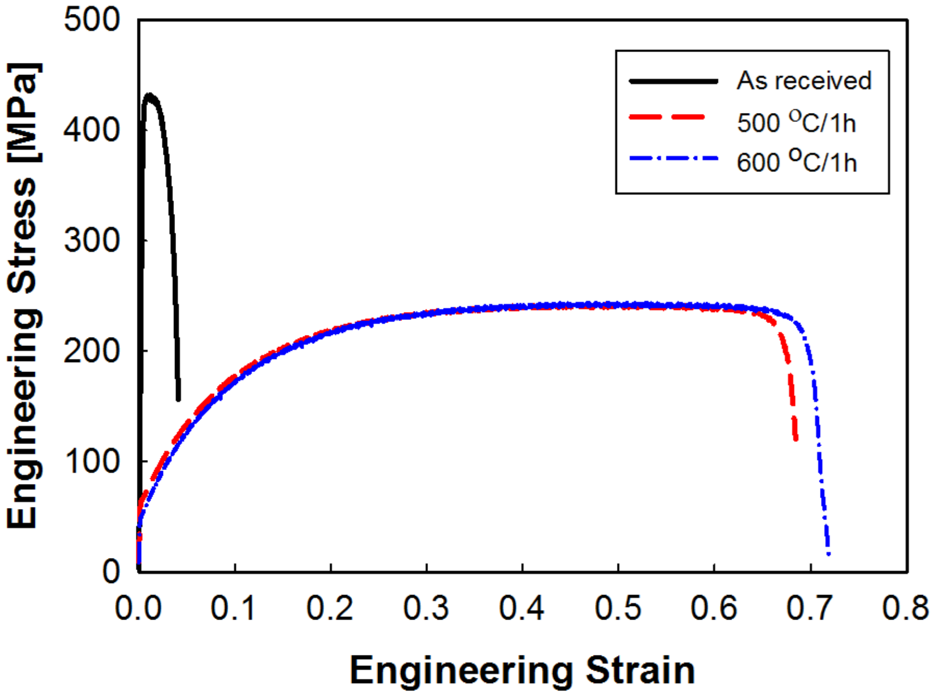

Figure 2.17 Tensile test results of as received and heat treated Cu alloy

Table 2.5 Summary of the tensile properties of heat treated Cu alloy

HT Temperature (°C)	Yield Strength (MPa)	Tensile Strength (MPa)	Uniform elongation
As received	420	437	-
500	64	242	0.46
600	50	244	0.51

In order to consider the anisotropic properties, the *r* values of sample heat treated for 1h/500°C were also measured. Figure 2.18 shows the relationship between width and thickness strains during the tensile testing of the longitudinal (*z* direction) and transverse (*Θ* direction) samples. The *r* values were obtained by calculating the slope of the best fitted straight line. The values of r_z and r_θ were 0.750 and 0.603, respectively. These values were used for considering anisotropic properties during the analysis of the tube bulge test results.

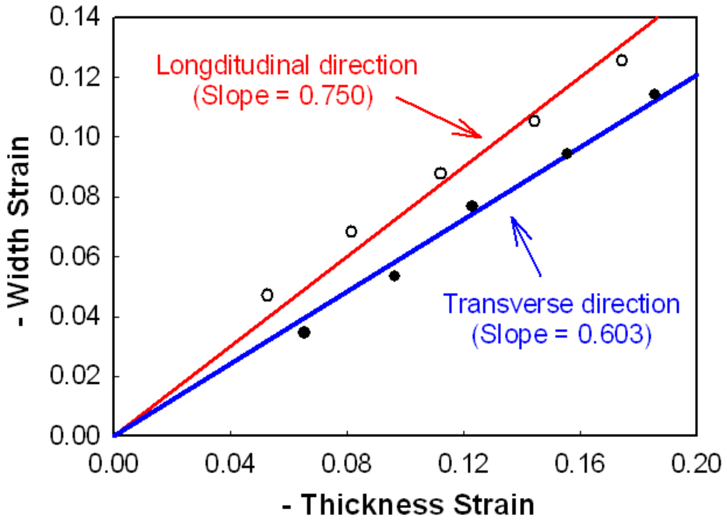

Figure 2.18 The *r* values of longitudinal and transverse samples heat treated for 1h/500°C

Summary: The samples heat treated for 1h/500°C and 1h/600°C have high formability. Therefore, two samples were used for the bulge test. Two different simulation approaches considering the anisotropic effect were used for these samples.

CHAPTER 3: TUBE BULGE TEST

3.1 Equipment and measurement

The equipment assembled for bulge testing, figure 3.1, consists essentially of three parts: the hard tooling, the hydraulic pressurizing system, and data acquisition system. Both ends of the tube blanks are clamped between pairs of fixed “dies” using a clamping force of up to 45 tons (figure 3.2). The tube ends are locked into the dies by lead-foil-wrapped sealing punches to which a force of up to 20 tons was able to be applied by an Enerpac hydraulic cylinder. The outer dies and the inner punches prevent axial movement of the tube blank during subsequent hydroforming. Hydraulic pressure (maximum 68.9 MPa) is applied to the tube blank via a through-hole in one of the sealing punches using an air assisted hydraulic pump from the Enerpac and measured by an Omega pressure sensor attached to a through-hole in the other punch. As the bulge forms in the free mid-segment of the tube its height is measure by a Keyence laser displacement sensor and its wall thickness measured by an Olympus ultrasonic thickness gauge. The data were collected and managed using a program in LabView (Appendix B). Figure 3.3 show the schematic of hydraulic bulge testing system.

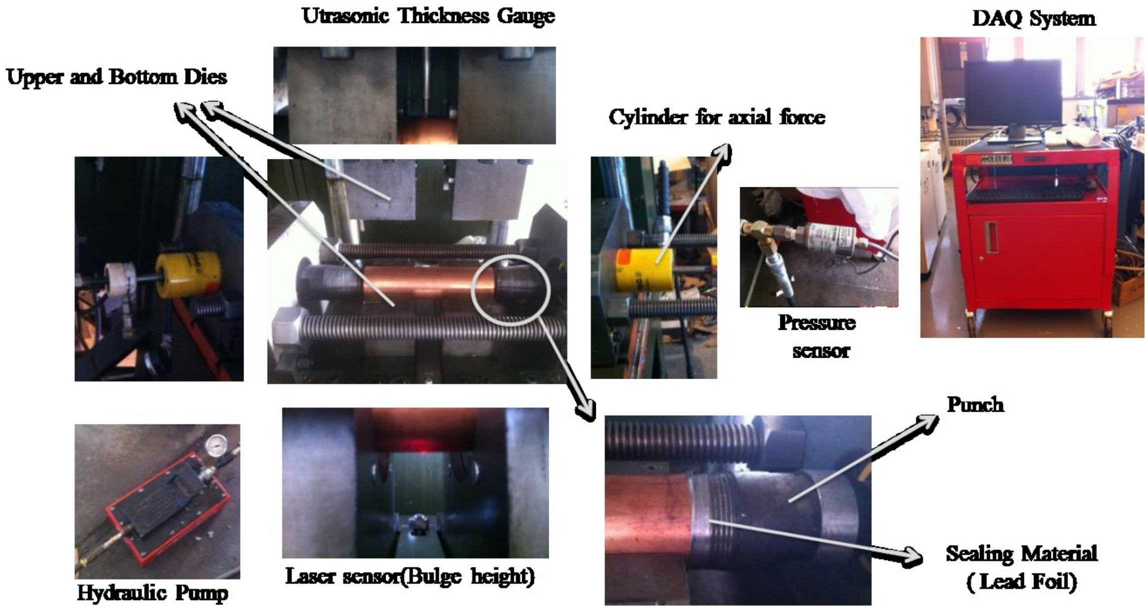

Figure 3.1 The equipment assembled for bulge testing

Figure 3.2 The OSU's hydraulic press for bulge test

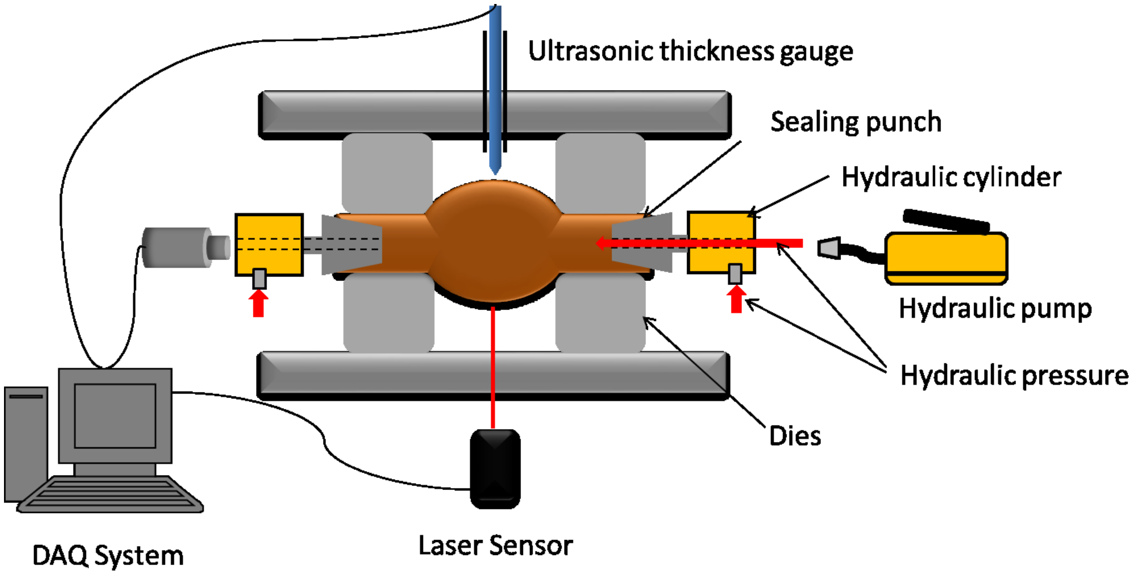

Figure 3.3 Schematic of the hydraulic bulge test system

3.2 Data analysis of test data

In order to quantitatively evaluate the mechanical properties of a material to be deformed an accurate constitutive equation is needed. The constitutive equation is generally obtained from the true stress-strain curve of a sample after uniaxial tensile testing. But if hydroforming is the goal it is necessary to obtain an equivalent or effective stress-strain relationship for a material under multi-axial stress. The results of a bulge test can provide the necessary data. The flow stress curves of tubular materials can be determined by several analytical models using. For analyzing the results several analytical models embodying various assumptions have been proposed (e.g. [94-96]). Dimensional parameters for analytical model are depicted in figure 3.4 and listed below.

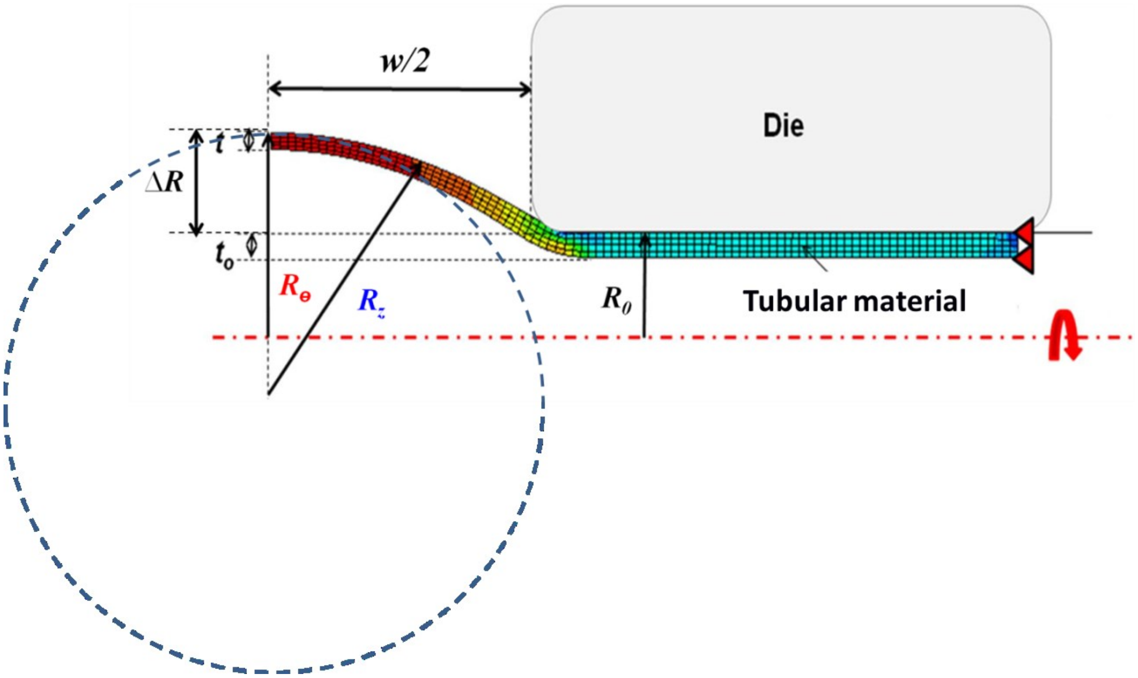

Figure 3.4 Parameters for analysis of the bulge test results

Dimensional Parameters

Starting Dimensions

R_0 = initial tube radius (31.75 mm)

t_0 = initial tube thickness (1.65 mm)

w = distance between the dies (70 mm, the “bulge width”)

Final Dimensions

t = wall thickness of the bulge

ΔR = radial expansion of the bulge (the “bulge height”)

$R_\theta \equiv R_0 + \Delta R$

R_Z = radius of the spherical bulge (the surface of the bulge is assumed to be everywhere part of a sphere of radius R_Z). By geometry (see Figure 3.5) R_Z is given by $[(w/2)^2 + \Delta R^2]/2\Delta R$

In order to determine the effective stress of material from bulge test, some parameters required to determine the flow stress curve from the bulge test results in terms of internal pressure, bulge height and wall thickness pressure. Figure 3.5 show the parameters required to determine the flow stress curve.

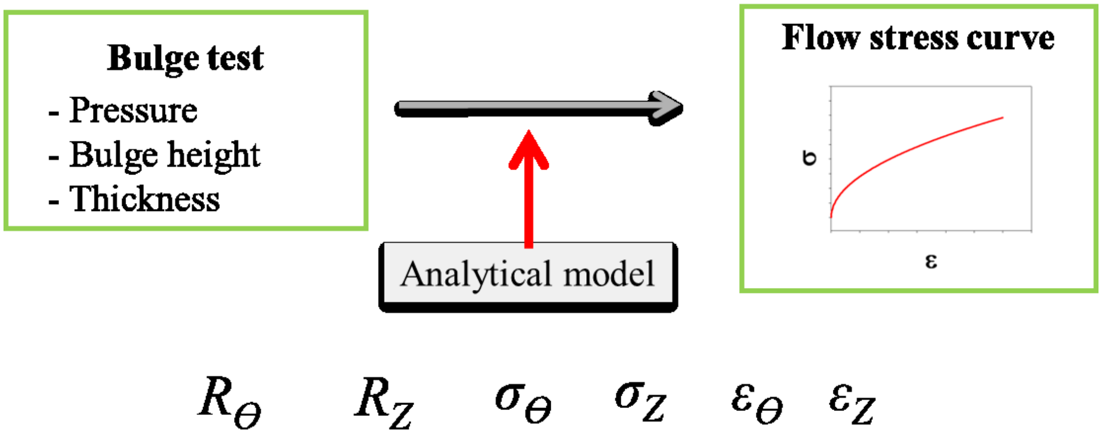

Figure 3.5 Parameters required to determine the flow stress curve

Here we discussed three different analytical methods (due to Fuchizawa et al[95], Koc et al [96], and Bortot et al [94]) to determine theses parameters for the effective stress-strain curve.

The radii of curvature in the longitudinal (R_z) and hoop (R_θ) directions should be determined first. By assuming the bulge is circular in shape, these values can be calculated as

$$R_\theta \equiv R_0 + \Delta R, \quad R_Z = [(w/2)^2 + \Delta R^2]/2\Delta \tag{3-1}$$

where r_0 is the initial radius of tube, Δr is the radial displacement of bulge height and w is the bulge width. Although these values are identical for all three models, the calculations of stress values are different.

For the Koc method [96], the longitudinal (σ_z) and hoop stresses (σ_θ) are obtained as functions of radii of curvature as follows:

$$\sigma_z = \frac{pR_\theta}{2t}, \tag{3-2}$$

$$\sigma_\theta = \frac{pR_\theta}{t} - \frac{\sigma_z R_\theta}{R_z} \tag{3-3}$$

where p is the internal hydraulic pressure and t is the wall thickness. In the case of the Fuchizawa method [95], these values can be also expressed as

$$\sigma_z = \frac{p(R_\theta - t)^2}{2t(R_\theta - t/2)}, \tag{3-4}$$

$$\sigma_\theta = \frac{p(R_\theta - t/2)}{t}\left[\left\{1 - \frac{t}{2(R_z - t/2)}\right\}\left\{1 - \frac{t}{2(R_\theta - t/2)}\right\} - \frac{(R_\theta - t)^2}{2(R_z - t/2)(R_\theta - t/2)}\right] \tag{3-5}$$

These values are derived by taking equilibrium of forces at the center of the tube. However, the equation for the Bortot method [94] is derived by assuming a strain path proportional to the corresponding deviatoric stress. The hoop stress can be calculated as

$$\sigma_\theta = \frac{pR_\theta R_z}{t}\left(\frac{1+2\dfrac{\varepsilon_\theta}{\varepsilon_z}}{2R_\theta + R_z + \dfrac{\varepsilon_\theta}{\varepsilon_z}(2R_z + R_\theta)}\right) \tag{3-6}$$

With this value, the longitudinal stress for the Bortot [94] method can be also obtained using equation 3-3.

Once directional stresses are calculated, effective stress ($\bar{\sigma}$) can be obtained using Von Mises yield criterion under isotropic condition:

$$\bar{\sigma} = \sqrt{{\sigma_\theta}^2 - \sigma_\theta \sigma_z + {\sigma_z}^2} \tag{3-7}$$

In order to obtain the effective strain, the hoop (ε_θ) and thickness strains (ε_t) should be calculated as

$$\varepsilon_\theta = \ln\left(\frac{R_\theta}{R_0}\right), \tag{3-8}$$

$$\varepsilon_t = \ln\left(\frac{t}{t_0}\right) \tag{3-9}$$

Then, effective strain ($\bar{\varepsilon}$) can be obtained using hoop and thickness strain as follows:

$$\bar{\varepsilon} = \frac{2}{\sqrt{3}}\sqrt{{\varepsilon_\theta}^2 + \varepsilon_\theta \varepsilon_t + {\varepsilon_t}^2} \tag{3-10}$$

If the anisotropic effects are considered, the effective stress and strain can be determined with the following equations using Hill's quadratic yield function [97-99]:

$$\bar{\sigma} = \sqrt{\frac{3}{2}} \cdot \left[\frac{(1+1/r_z){\sigma_z}^2 - 2\sigma_\theta \sigma_z + (1+1/r_\theta){\sigma_\theta}^2}{1/r_\theta + 1 + 1/r_z}\right]^{1/2} \tag{3-11}$$

$$\begin{aligned}\bar{\varepsilon} = \sqrt{2/3} \cdot \left[(1/r_\theta + 1/r_z + 1)/(1/r_z/r_\theta + 1/r_z + 1/r_\theta)\right]^{1/2} \\ \cdot \left[(1/r_\theta + 1/r_z){\varepsilon_\theta}^2 + 2/r_\theta \cdot \varepsilon_\theta \varepsilon_t + (1+1/r_\theta){\varepsilon_t}^2\right]^{1/2}\end{aligned} \tag{3-12}$$

where r_z and r_θ are r values obtained from longitudinal and transverse specimens, respectively. The principle stresses and strains are identical to those of isotropic case.

3.3 Verification of analytical model

3.3.1 Verification procedure

In this section, the steps obtaining the flow stress curve from the tube bulge test using three different analytical models mentioned before were verified. In order to verify the steps to be taken in analyzing experimental-bulge-test data a self-consistent argument recovers the original constitutive properties from the results of an FEM-based "virtual bulge test". Starting off with a published stress strain relationship (which for the purpose of the demonstration is based on the linear tensile testing of commercial Nb [49]) an FEM model of a bulge test was created. Regarding this as a "virtual bulge test" the resulting bulge heights and wall thicknesses obtained were used to recover a new stress-strain curve (according to the prescriptions of Fuchizawa et al [95], Koc et al [96], and Bortot et al [94]) for comparison with the starting data.

3.3.2 FEM simulation of tube bulge test (Virtual bulge test)

The deformation behavior of Nb tube under hydraulic pressure was tested using a FE model. ABAQUS Explicit was utilized for this analysis. This model is identical to the continuum model discussed in the following chapter 4. The input to the model consists of the tabulated elastic properties of Nb [100], table 3.1, and its graphically represented plastic properties [49], figure 3.6. The parameters of the fitted curve $\sigma = K.\varepsilon^n$ viz $K =$

452.54 MPa and the strain hardening exponent n = 0.192 were extracted for use in the simulation.

Table 3.1 The elastic properties of Nb for FE simulation [100]

Material	Young's modulus	Poisson's ratio	Density
Nb	104.9 GPa	0.397	8.57 g/cm^3

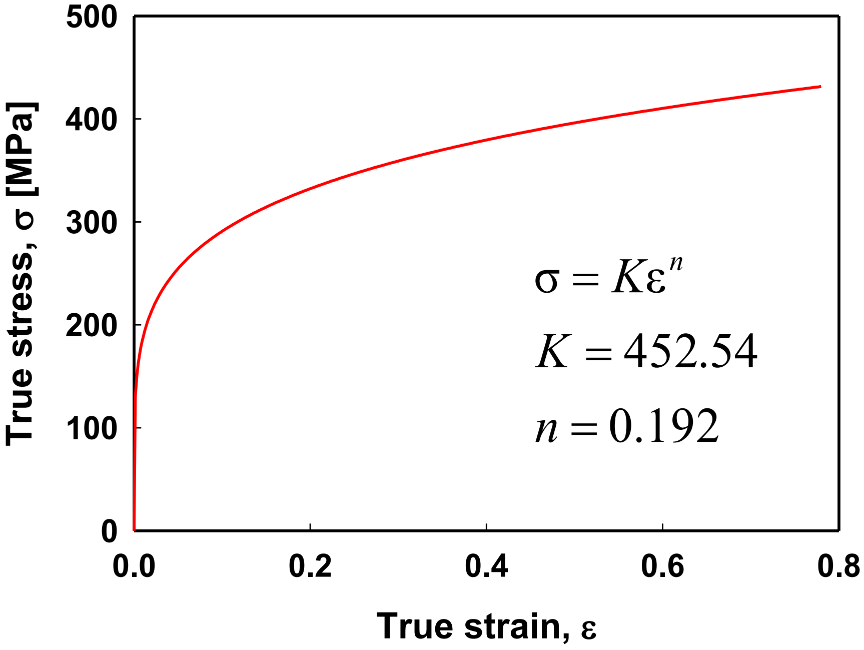

Figure 3.6 True stress-strain curve for commercial Nb after [49] for use as input to the FE simulation.

A von Mises yield function was adopted to define isotropic yielding for simplicity [101]. The initial outer radius (R_0), wall thickness (t_0) and bulge width (w) of tube were 28, 2 and 70 mm, respectively.

3.3.3 Analysis of the virtual bulge test results and discussion

The results of the simulation are depicted graphically in figure 3.7.

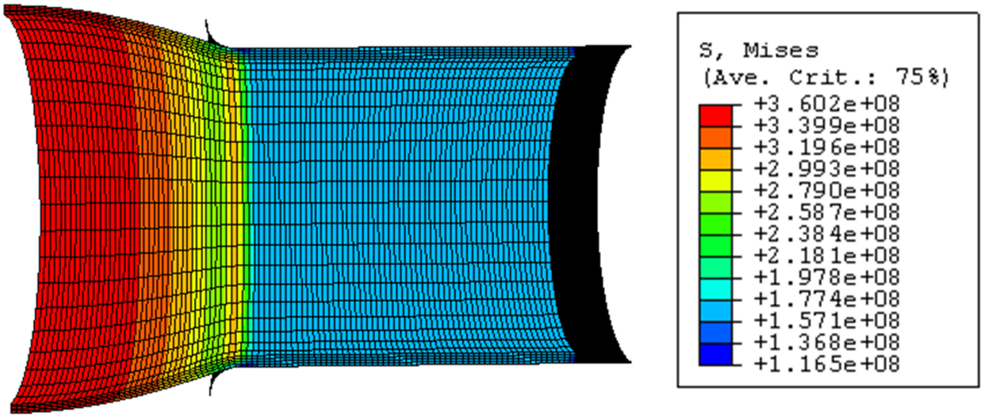

Figure 3.7 Pictorial representation of the results of the simulation

The numerical results of the simulation are depicted in figure 3.8 (a-c). As expected, the bulge height drastically increased with increasing pressure above ~22 MPa, while wall thickness decreased. An inverse linear relationship between bulge height and thickness was also observed, as shown in figure 3.8 (C). The slope of this line was - 0.062.

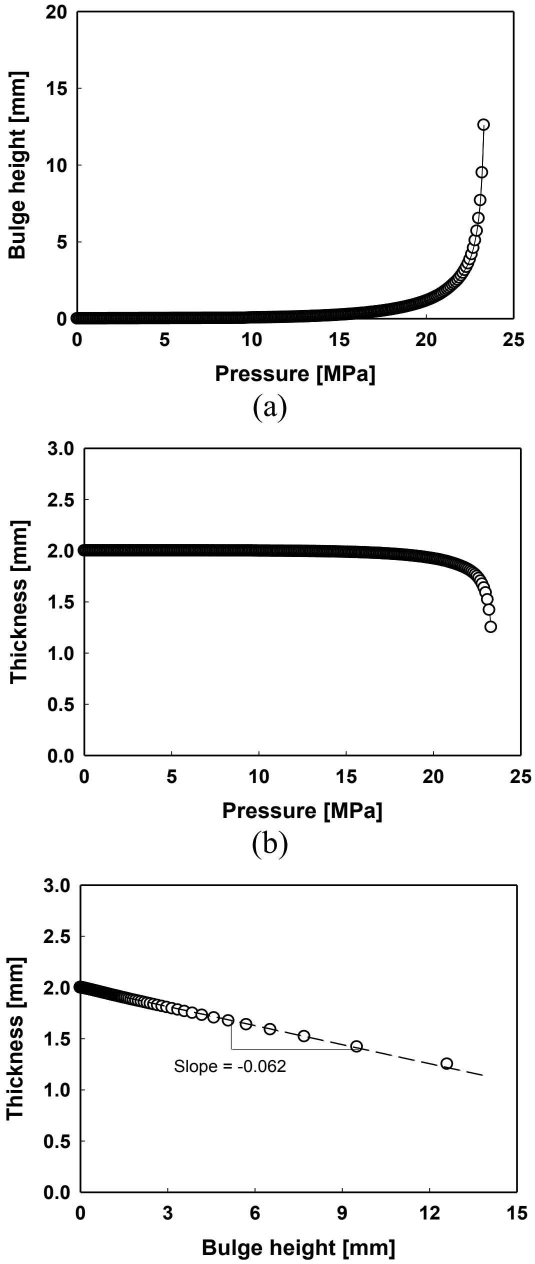

(a)

(b)

(c)

Figure 3.8 The simulation results: (a) pressure vs. bulge height, (b) pressure vs. wall thickness and (c) bulge height vs. wall thickness

Table 3.2 presents some numerical results of the simulation for five selected values of the hydraulic pressure (18~22 MPa) corresponding to which are the five values of effective (triaxial) stress-strain data pairs plotted in figure 3.9. Fitted to the usual $\sigma = K{\cdot}\varepsilon^n$ these yield $K = 449.44$ MPa and $n = 0.188$.

Table 3.2 Numerical results of the simulated bulge test

Internal Pressure [MPa]	Bulge height [mm]	Wall thickness [mm]
18	0.59	1.96
19	0.82	1.95
20	1.16	1.92
21	1.74	1.88
22	2.80	1.82

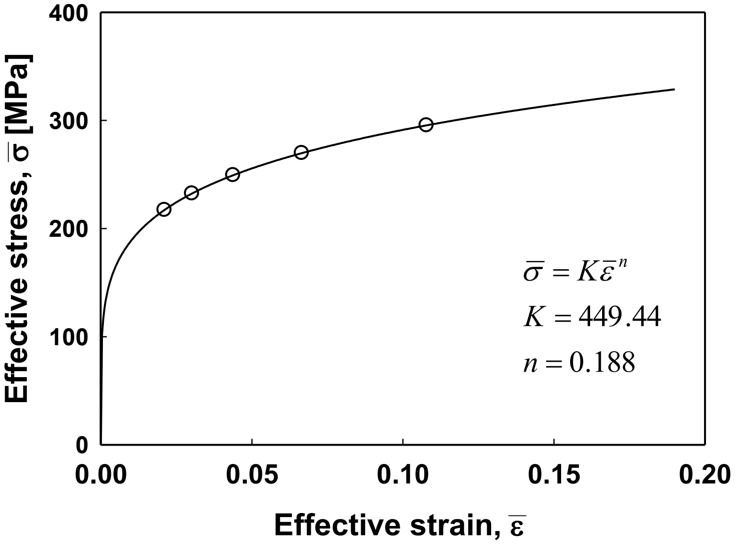

Figure 3.9 Five values of effective tri-axial stresss-strain data from the FE simulation to which the function $\sigma = K{\cdot}\varepsilon^n$ has been

As seen in figure 3.10, the flow stress curves lie close to each other, especially, the results from Koc et al. and Bortot et al. which agreed with the FEM results to within about 1.5 %. The small observed differences between these flow curves stem from the analytical approximation. But in the case of the Fuchizawa method, the effective stress was underestimated by about 5 %. We attribute this to the fact that the force balance equation used in Fuchizawa method for calculating the stress was different from the one used by Koc et al. and Bortot et al.

As a result we are confident in the utility of the analytical approaches of Koc et al. and Bortot et al for analyzing the results of experimental bulge testing. In the following study, analytical model of Koc et al. will be utilized.

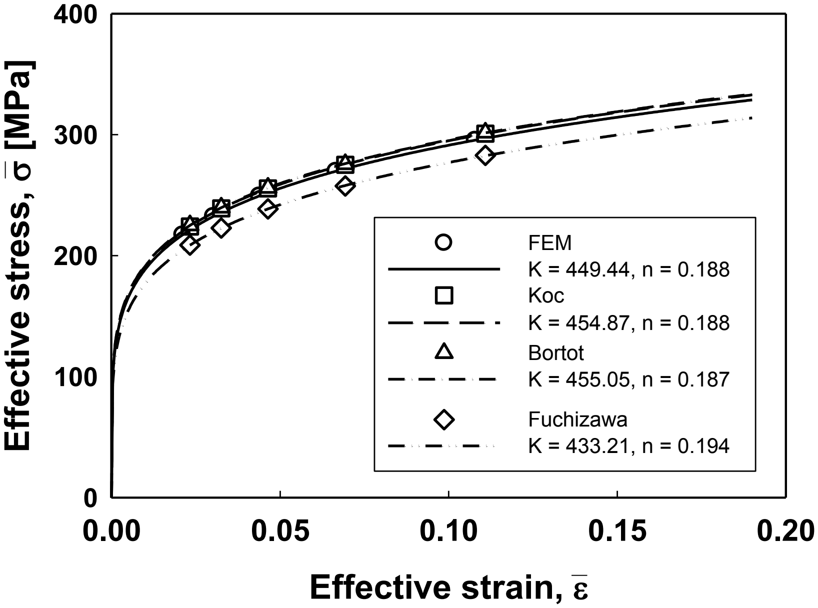

Figure 3.10 The flow stress curves and constitutive properties obtained by various analytical models

3.4 Results and comparison of bulge and tensile tests

3.4.1 OFHC Cu

By way of example, figure 3.11 depicts the OFHC Cu tube bulged tested after HT for 2h/500°C. Figure 3.12 shows the variation of bulge height and wall thickness as a function of pressure during bulge test for OFHC copper. Selected bulge test results for OFHC Cu after HT for 2h/500°C are shown in Tables 3.3. Using these data, and with the aid of the analytical model described above, corresponding flow stress curves were developed and fit to the Hollomon relationship $\sigma = K\cdot\varepsilon^n$ within $0.02 < \varepsilon < 0.60$. The results for the OFHC Cu are shown in figures 3.13. Also included for comparison is the fitted tensile test result for the Cu. The Hollomon parameters for all the fits are listed in Table 3.4. This deviation between the results from uniaxial and biaxial stress state may stem from the crystallographic properties of the material and its mode of deformation. Therefore, the tube bulge test which embodies more accurate deformation behavior is necessary for the successful design of a SRF cavity relating hydroforming process.

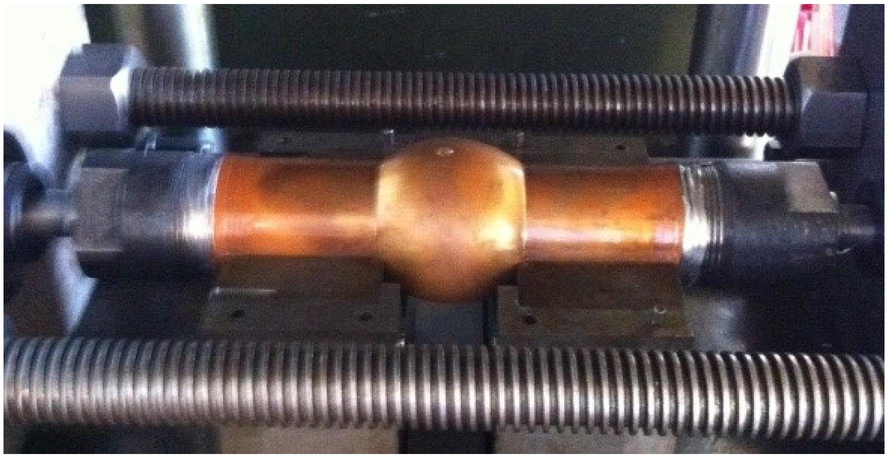

Figure 3.11 Bulge formed in the OFHC Cu tube heat treated for 2h/500°C

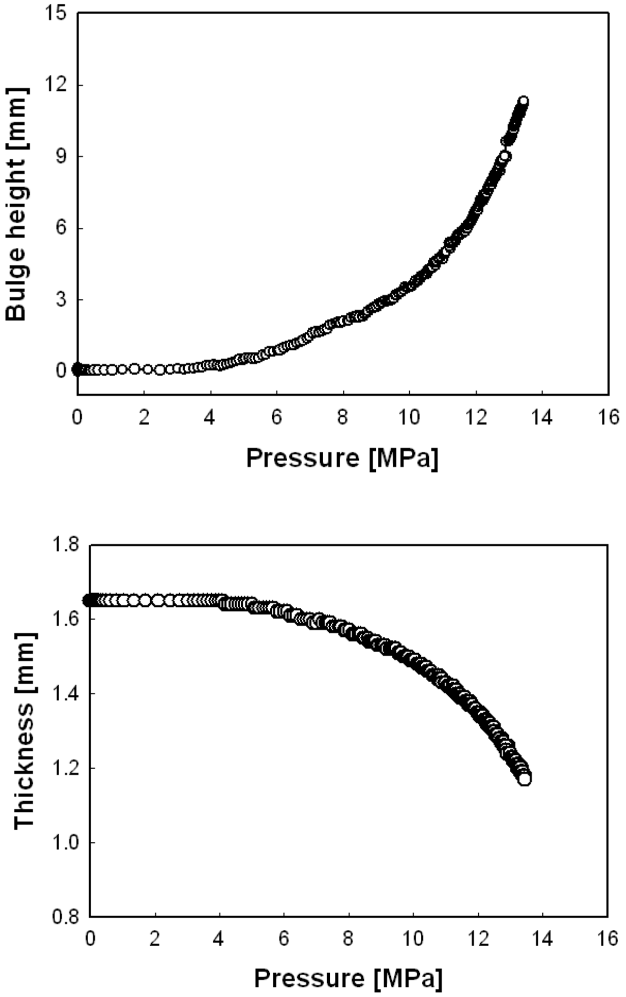

Figure 3.12 Bulge test results of OFHC Cu tube heat treated for 2h/500°C

Table 3.3 Selected bulge test results for OFHC Cu heat Treated for 2h/500^{o}C

Pressure (MPa)	Bulge height (mm)	Wall thickness (mm)
6.02	0.86	1.62
7.00	1.44	1.59
8.01	2.09	1.57
9.02	2.72	1.53
10.02	3.54	1.49
11.01	4.72	1.43
11.99	6.67	1.35
13.01	9.64	1.23

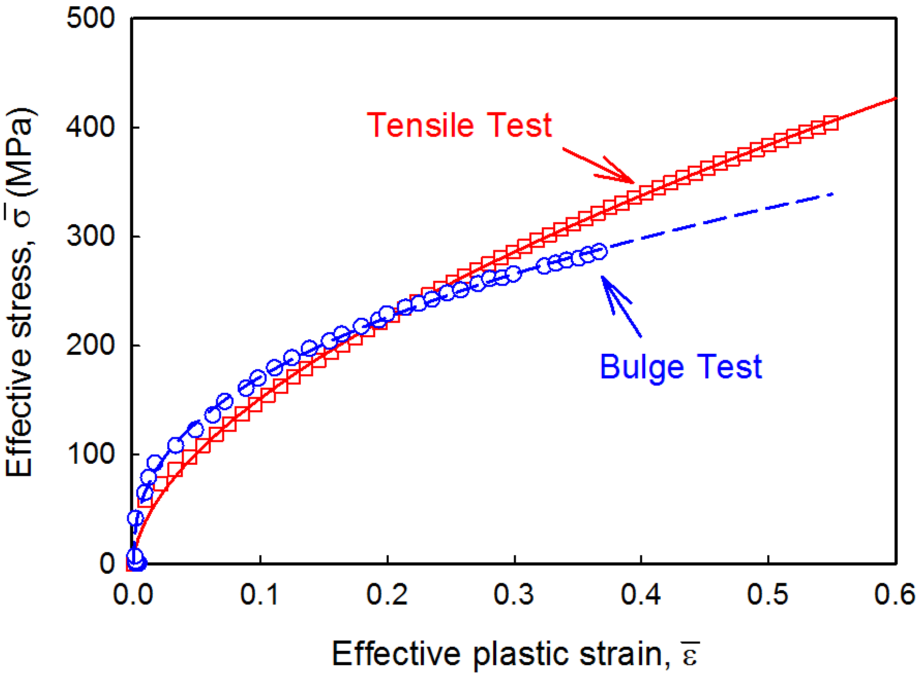

Figure 3.13 Effective stress-plastic strain curves for tensile- and bulge-tested heat treated OFHC Cu for 2h/500°C

Table 3.4 Hollomon parameters fitted to the analyzed effective stress and strain data for tensile-tested and bulge-tested OFHC Cu for 2h/500^{o}C

Material	Parameter	Tensile test	Bulge test
OFHC Cu	*K*	573.30	430.72
	n	0.578	0.400

3.4.2 Reactor-grade niobium

Figure 3.14 show the bulged niobium tube heat treated for 2h/1000°C. The bulge test results were shown in figure 3.15 and table 3.5. Using these data, the obtained effective stress-strain curve and the fitted hollomon parameters were shown in figure 3.16 and table 3.6 respectively.

Figure 3.14 Bulge formed in the reactor grade Nb tube heat treated for 2h/1000^{o}C

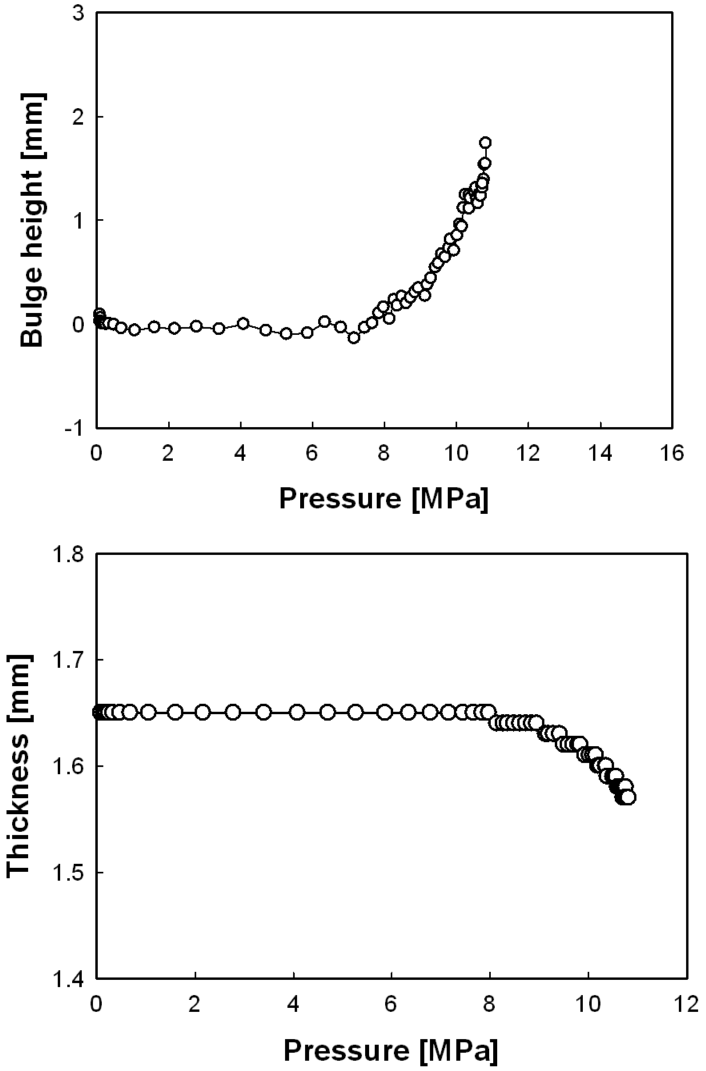

Figure 3.15 Bulge test results of reactor grade Nb heat treated for 2h/1000°C

Table 3.5 Selected bulge test results for reactor grade Nb heat treated for 2h/1000^{o}C

Pressure (MPa)	Bulge height (mm)	Wall thickness (mm)
8.95	0.35	1.64
9.49	0.59	1.62
10.02	0.85	1.61
10.50	1.27	1.59
10.80	1.54	1.57

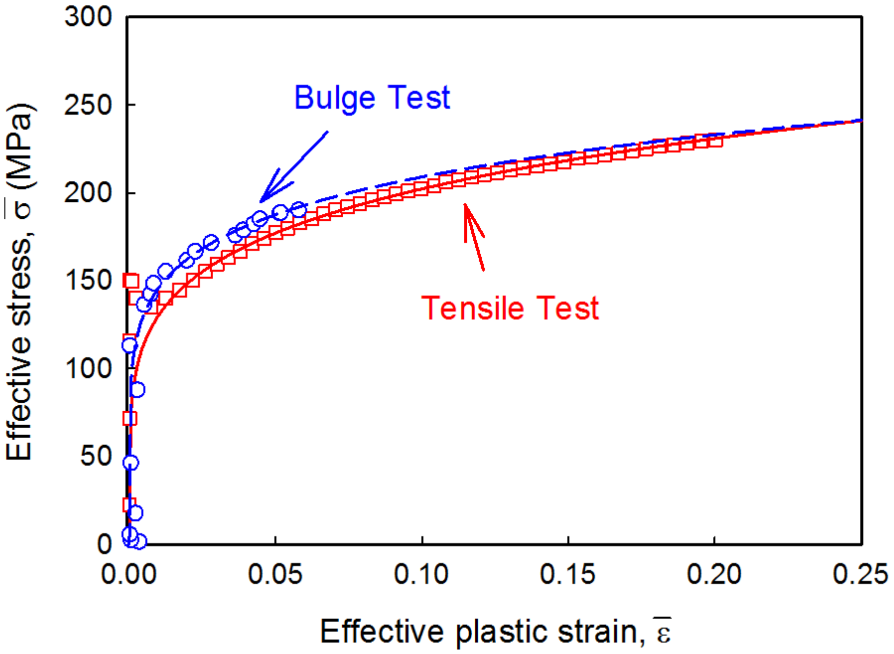

Figure 3.16 Effective stress/plastic strain curves for tensile- and bulge-tested heat treated reactor-grade Nb for 2h/1000^{o}C

Table 3.6 Hollomon parameters fitted to the analyzed effective stress and strain data for tensile-tested and bulge-tested reactor grade Nb for 2h/1000^{o}C

Material	Parameter	Tensile test	Bulge test
Nb heat treated for 2h/1000^{o}C	*K*	314.18	299.99
	n	0.191	0.157

3.4.3 Cu alloy

Two bulge tests were performed with the Cu alloy tubes heat treated for 1h/500°C and 1h/600°C. Figure 3.17 show the bulged samples heat treated for 1h/500°C and 1h/600°C after testing, respectively. Figure 3.18 and table 3.7 show the bulge test results of samples heat treated for 1h/500°C. The results for the sample heat treated for 1h/600°C are shown in figure 3.19 and table 3.8. From these data, the flow stress curves were obtained. For the sample heat treated for 1h/500°C, the anisotropic properties were also considered using the *r* value obtained from the tensile test (figure 2.18). Figure 3.20 and 3.21 show the obtained effective stress-strain curves. Table 3.9 shows the summary of the fitted parameters obtained from the tensile and tube bulge tests of the Cu alloy.

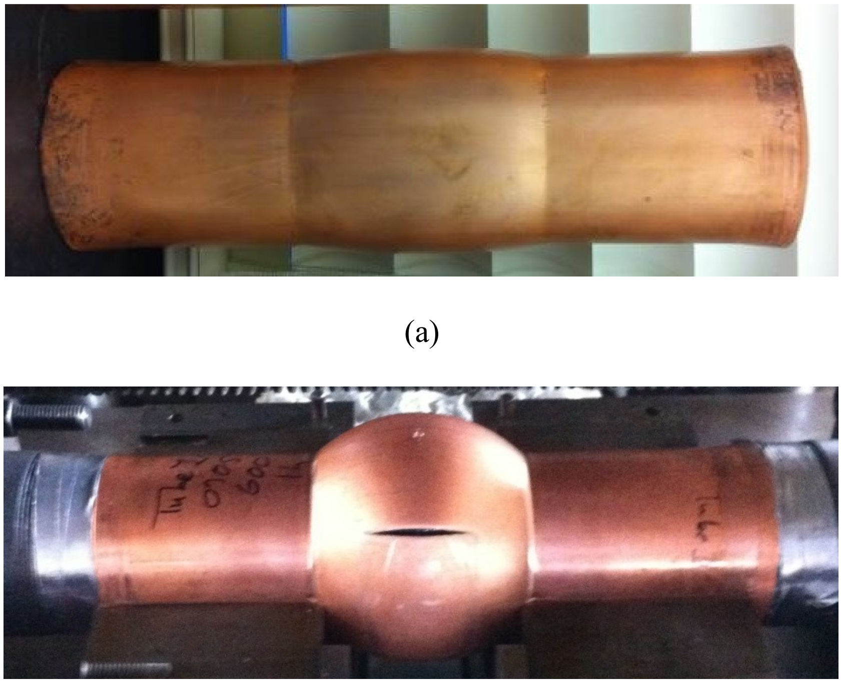

(a)

(b)

Figure 3.17 Bulge formed in the Cu alloy heat treated for (a) 1h/500°C and (b) 1h/600°C

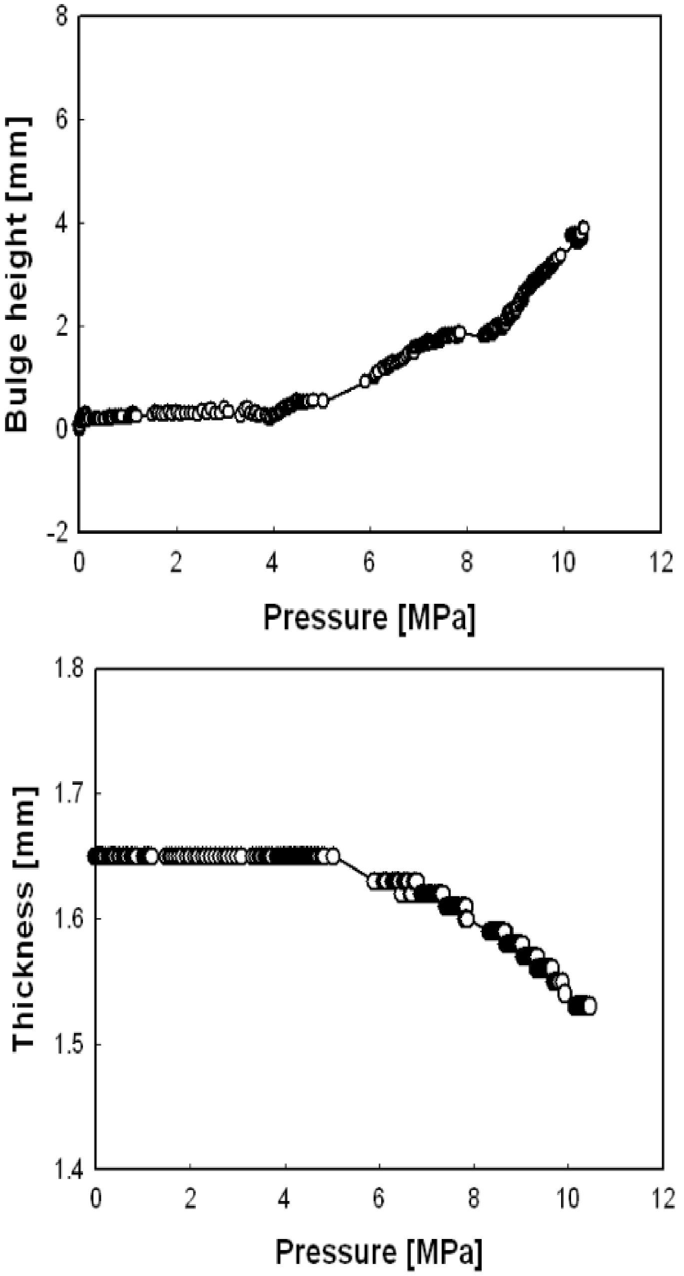

Figure 3.18 Bulge test results of Cu alloy heat treated for 1h/500^{o}C

Table 3.7 Selected bulge test results for Cu alloy heat treated for 1h/500^{o}C

Pressure (MPa)	Bulge height (mm)	Wall Thickness (mm)
6.09	0.996	1.63
7.02	1.606	1.62
8.34	1.816	1.59
9.00	2.255	1.58
10.27	3.638	1.53

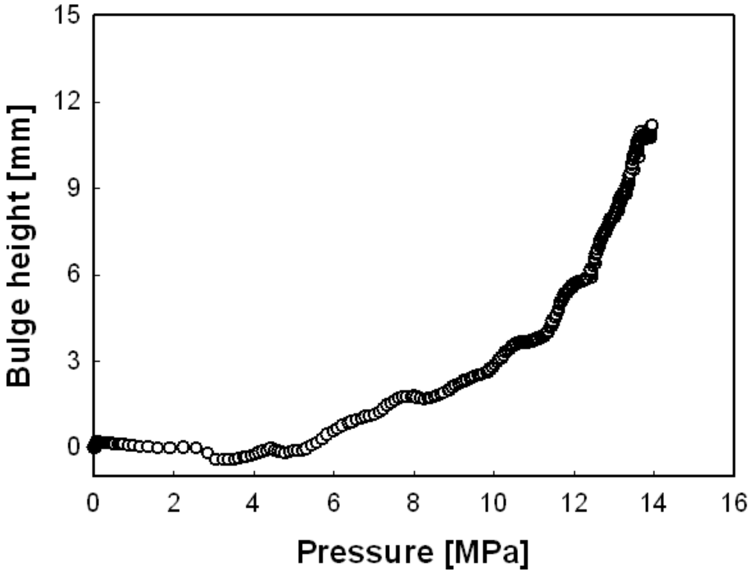

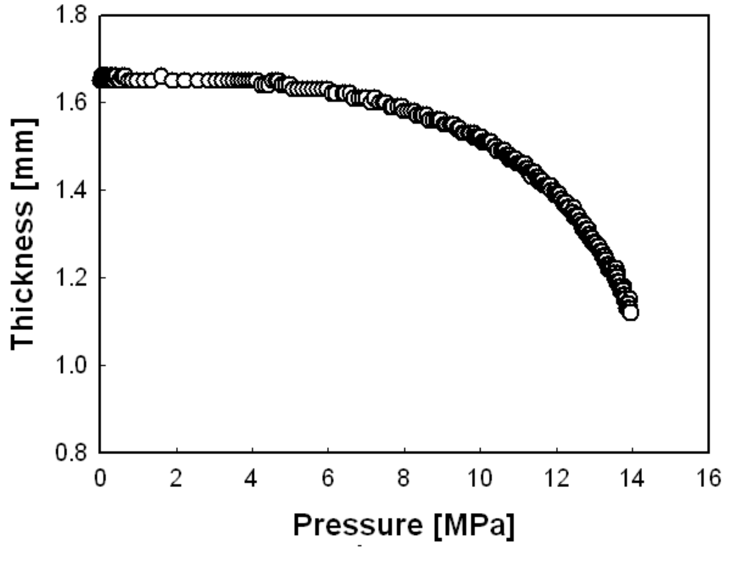

Figure 3.19 Bulge test results of Cu alloy heat treated for 1h/600^{o}C

Table 3.8 Selected bulge test results for Cu alloy heat treated for 1h/600°C

Pressure (MPa)	Bulge height (mm)	Wall thickness (mm)
6.09	0.659	1.62
7.01	1.150	1.61
8.01	1.788	1.58
9.05	2.157	1.55
10.02	2.876	1.52
11.02	3.746	1.46

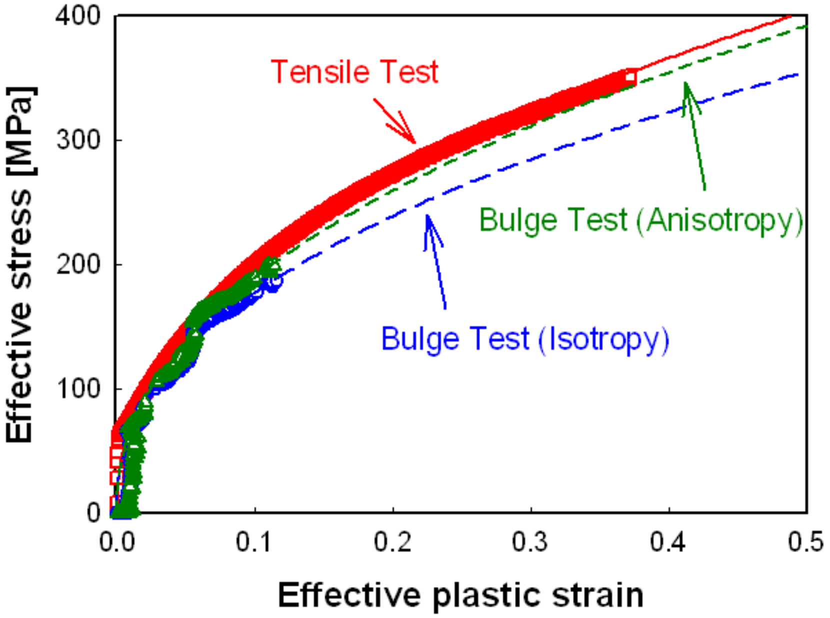

Figure 3.20 Effective stress-plastic strain curves for tensile- and bulge-tested Cu alloy heat treated for 1h/500°C

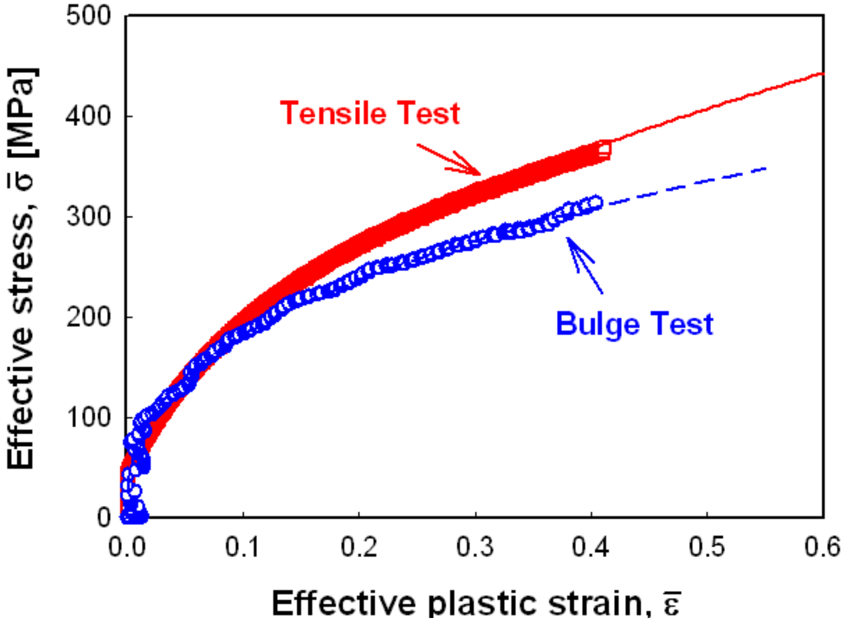

Figure 3.21 Effective stress-plastic strain curves for tensile- and bulge-tested Cu alloy heat treated for 1h/600°C

Table 3.9 Hollomon parameters fitted to the analyzed effective stress and strain data for tensile-tested and bulge-tested Cu alloy heat treated for 1h/500°C and 1h/600°C

Material	Parameter	Tensile test	Bulge test (Isotropy)	Bulge test (Anisotropy)
Cu Alloy heat treated for 1h/500 °C	K	547.30	497.78	536.10
	n	0.4373	0.4315	0.4498
Cu Alloy heat treated for 1h/600 °C	K	561.20	436.40	-
	n	0.460	0.378	-

CHAPTER 4: NUMERICAL SIMULATION

Based on the obtained experimental data in chapter 3, numerical simulation analysis was performed. First, the continuum model was constructed as a macroscopic approach. Numerical simulation based on the constitutive equations obtained by tensile and bulge tests were performed and compared to the experimental results in order to determine the most accurate flow stress curve of tubular materials under multi-axial force. The effect of anisotropic properties using the anisotropy coefficient was also investigated. Second, the multi-scale simulation approach was discussed using both the crystal plasticity model and the continuum model to consider the anisotropic properties and its evolution during the deformation.

4.1 Macro-scale approach

4.1.1 Continuum model

Finite element modelling (FEM) of the tube bulge test was performed using commercially available ABAQUS/explicit software. The axisymmetric cross-section of the tube was modeled considering the geometric symmetry to reduce the computational time as shown in figure 3.4. Dies that applied axial and radial constraints to the tube ends prevented axial feeding. Four-noded axisymmetric solid elements (CAX4R) were used for the bulge-forming simulation with 4 element layers through the thickness. The input to the model comprised the elastic and plastic properties. The plastic property inputs were the constitutive equations obtained by tensile or bulge tests in previous chapter.

For isotropic materials, the samples of OFHC Cu heat treated for 2h/500°C and reactor grade Nb heat treated for 1h/600°C were used. The elastic properties of materials used for the simulation are given Table 4.1. The plastic property inputs were the *K* and *n* values listed in previous section (Table 3.4 for OFHC Cu and Table 3.6 for Nb).

In order to obtain the accurate flow stress curve from the bulge test, the effect of consideration of anisotropic properties were also evaluated. The Cu alloy sample heat treated for 1h/500°C were used for this study. The results of tensile and bulge tests in figure 3.20 and table 3.9 were used for plastic property. The elastic properties of materials used for the simulation are given Table 4.1.

Table 4.1 Elastic properties and densities of Cu and Nb metals for the simulation

Material	Young's Modulus (GPa)	Poisson's ratio	Density (g/cm^3)
OFHC Cu	115	0.31	8.90
Nb	103	0.38	8.57
Cu alloy	110	0.36	8.93

4.1.2 Simulation results for isotropic materials

The results of the simulations expressed in terms of bulge height, *ΔR*, and bulge thickness, *t*, versus pressure for the OFHC Cu tube and the reactor-grade Nb tube are displayed in figures 4.1 and 4.2. The three curves in each figure compare the experimental results ("**Experiment**") with the computational results based on the tensile-derived ("**Tensile Test"**) and bulge-derived ("**Bulge Test"**) *K* and *n* values. Since they are actually derived from bulge-test data, the **Bulge Test** curves should replicate the **Experimental** curves and they do so within the stated model approximations up to pressures of about 10 MPa. Not so for the curves labeled **Tensile Test** which, derived from uniaxial tensile data, do not consider deformation under multi-axial stress.

Figures 4.1 show the bulge-based numerical simulation and experimental results tending to diverge at pressures above about 10 MPa and approach the burst pressure. It may be caused by the anisotropic properties or localized deformation as the pressure approaches the burst pressure. During the calculation of flow stress curve using the analytical model, it assumed that the material is isotropic. However, the orientation of the material will change during deformation. Therefore, the material behavior under large strains may be not isotropic. In addition, the estimated burst pressure for the Cu tube based on its tensile strength and dimensions [39] is 12.6 MPa. Although the Cu tube used for the bulge test did not burst above the estimated pressure, the possibility of mechanical instability or localized necking is relatively high near the burst pressure [102, 103]. The reactor grade Nb tube burst at 10.8 MPa, higher than the estimated pressure of 10.1 MPa.

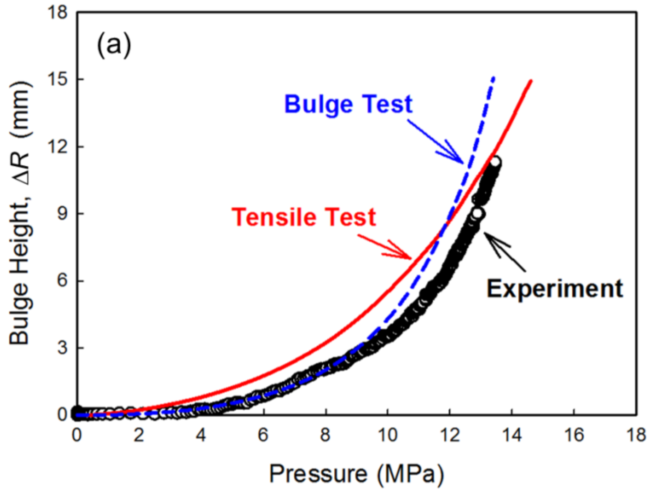

(a)

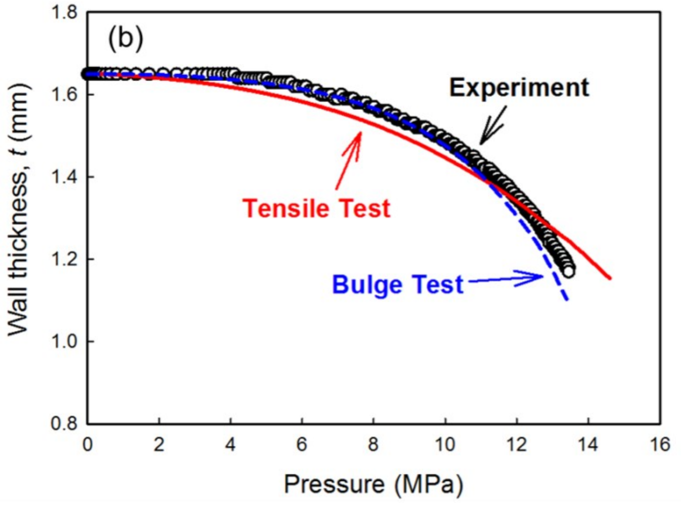

(b)

Figure 4.1 For OFHC Cu, comparisons of the experimental results with simulated results based on constitutive relationships derived from the tensile test and the bulge test in terms of (a) bulge height, ΔR, and (b) bulge thickness, t, versus applied pressure

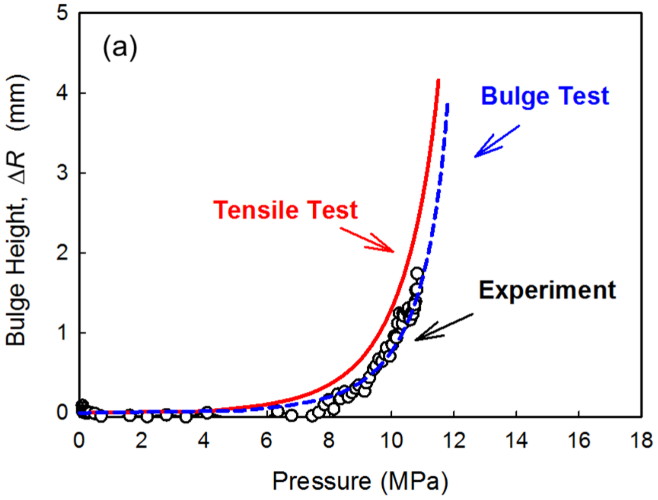

(a)

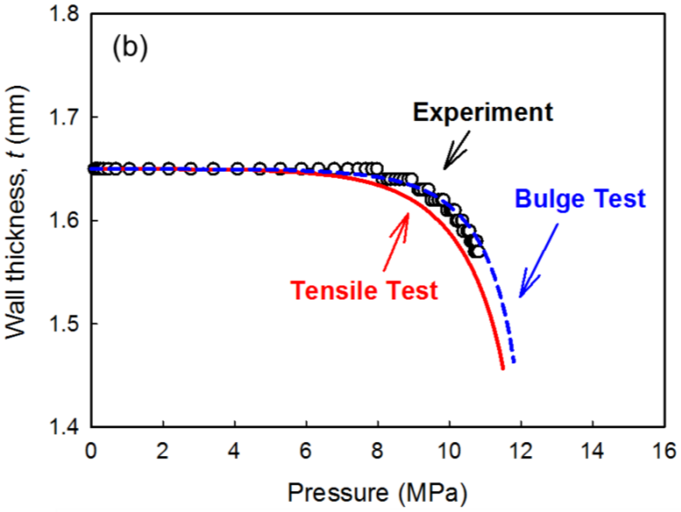

(b)

Figure 4.2 For reactor grade Nb, comparisons of the experimental results with simulated results based on constitutive relationships derived from the tensile test and the bulge test in terms of (a) bulge height, *ΔR*, and (b) bulge thickness, *t*, versus applied pressure

4.1.3 Simulation results for anisotropic materials

Figure 4.3 shows the numerical simulation results using the effective stress-strain curve from the bulge test including experimental result. The three curves in each figure compare the experimental results (“**Experiment**”) with the computational results based on the bulge-derived assuming isotropy (**“Bulge Test (Isotropy)”**) and anisotropy **“Bulge Test (Anisotropy)”** *K* and *n* values. The bulge height as a function of pressure using the flow stress curve from the bulge test assuming isotropy was quite well matched to the experimental data, while the thickness was not well matched. The simulation results using the flow stress curve from the bulge test considering anisotropy effect using *r* values were closest to the experimental data for both bulge height and thickness. Hence the incorporation of small residual anisotropic effects using r values from the tensile test led to even more accurate results. For anisotropic materials, the flow stress curve obtained from the tube bulge test including anisotropic effect using *r* value represents more accurate deformation behavior of hydroformed tubular materials.

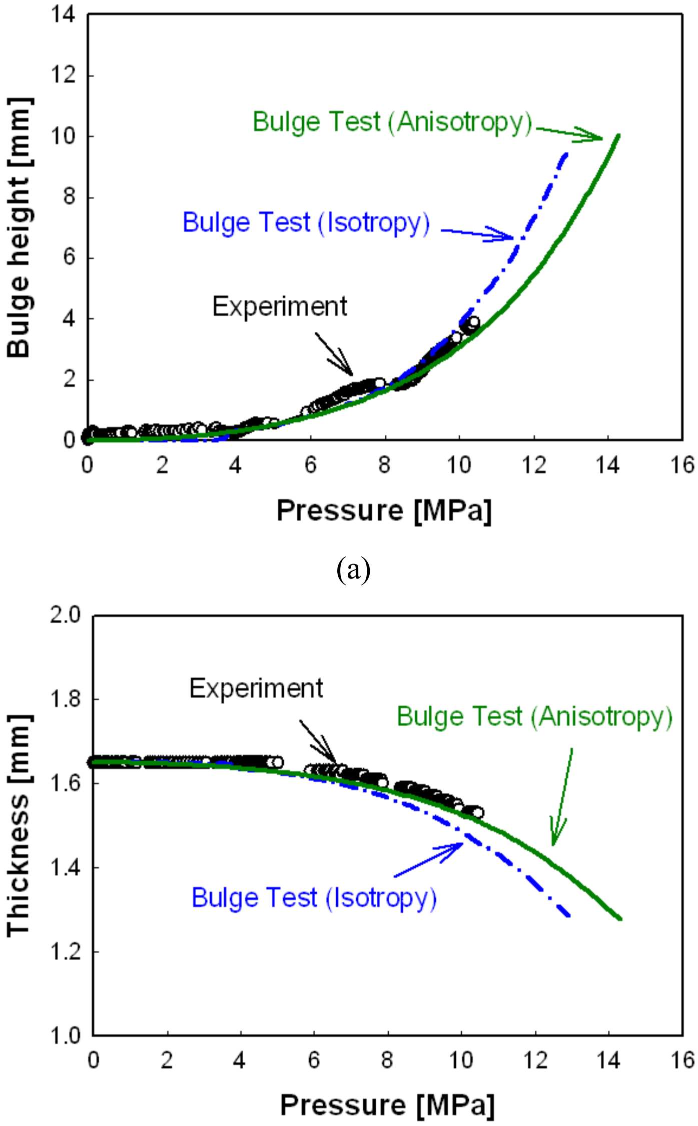

(a)

(b)

Figure 4.3 For Cu alloy, comparisons of the Experimental results with simulated results based on constitutive relationships derived from the Bulge Test by assuming isotropy or anisotropy in terms of (a) bulge height, ΔR, and (b) bulge thickness, t, versus applied pressure

4.2 Multi-scale approach

4.2.1 Crystal plasticity model

In order to consider the influence of the crystallographic texture and its evolution during deformation for the polycrystalline material, a microscopic simulation model using CP-FEM was constructed. The crystal constitutive equations based on slip systems and statistical grain orientation information were used to predict the plastic anisotropy and texture evolution during deformation. For numerical convenience, the PAN based CP-FEM model [12] considered that the plastic deformation occurs by crystallographic slip alone, and other deformation mechanism such as twining, diffusion and grain boundary sliding are not considered. In addition, neighboring grain interactions or the present of grain boundaries were ignored. The linkage of grains was considered by assuming that all grains exhibit identical strain enforcing inter-grain equilibrium.

The kinematics of the crystal plasticity approach used for this study is based on the study of [13–17]. The constitutive equation in the single crystal can be expressed using the second Piola-Kirchhoff stress S and lagrangian strain tensor E as follows:

$$\mathrm{S} = \mathrm{C^e} : \mathrm{E} = \det(\mathrm{F}^e)\mathrm{F}^{e-1}\sigma\mathrm{F}^{e-T}, \tag{4-1}$$

$$\mathrm{E} = \frac{1}{2}(\mathrm{F}^{eT}\mathrm{F}^{e} - 1) \tag{4-2}$$

where $\mathrm{C^e}$ is the fourth order elastic constant matrix and σ is the Cauchy stress.

The crystal plasticity constitutive equation is determined by the dislocation glide. The deformation gradient consists of elastic and plastic parts:

$$\mathbf{F} = \mathbf{F}^e\mathbf{F}^p \tag{4-3}$$

where F^e and F^p define elastic distortion of lattice and dislocation glide on crystal slip plane, respectively. The rate of the plastic part of the deformation gradient $\dot{\mathrm{F}}^p$, is defined as

$$\dot{\mathrm{F}}^p = \overline{\mathrm{L}}^p \mathrm{F}^p \tag{4-4}$$

where $\overline{\mathrm{L}}^p$ is the plastic velocity gradient. This gradient is related to the glide on the slip system with slip plane *α,* slip plane normal $\mathrm{n}_0{}^{(\alpha)}$, and slip direction $s_0{}^{(\alpha)}$ as follows:

$$\overline{\mathrm{L}}^p = \sum_{\alpha=1}^{n} \dot{\gamma}^{(\alpha)} s_0{}^{(\alpha)} \mathrm{x} \mathrm{n}_0{}^{(\alpha)} \tag{4-5}$$

where $\dot{\gamma}^{(\alpha)}$ is the rate of plastic shear on the slip system *α*, and *n* is total number of slip systems.

The rate of shear on the slip system *α* is described by a power low function of the resolved shear stress as follows:

$$\dot{\gamma}^{(\alpha)} = \dot{\gamma}_0 \left(\frac{\tau^{(\alpha)}}{g^{(\alpha)}} \right)^{1/m} \sin(\tau^{(\alpha)}) \tag{4-6}$$

where $\dot{\gamma}_0$ is a reference shear rate, $\tau^{(\alpha)}$ is the resolved shear stress on the slip system *α*, $g^{(\alpha)}$ is slip resistance, and *m* is strain rate sensitivity.

The slip resistance $g^{(\alpha)}$ in slip system *α* evolves during the deformation. It has the initial value of g_0 and changes as a function of plastic strain on all slip systems *β* as

$$\dot{g}^{(\alpha)} = \sum_{\beta=1}^{n} h_{\alpha\beta} \left| \dot{\gamma}^{(\beta)} \right| \tag{4-7}$$

where $h_{\alpha\beta}$ are hardening coefficients matrix representing the interactions of dislocation in different slip planes. It can be expressed by

$$h_{\alpha\beta} = h_{\beta}(q_{self} + (q_{self} - q_{lat})\delta_{\alpha\beta}), \tag{4-8}$$

$$h_{\beta} = h_0 \left(1 - \frac{g^{(\beta)}}{g_s}\right)^a \tag{4-9}$$

where the q_{self} and q_{lat} are self and latent hardening coefficient, respectively. In equation 4.9, h_0 is a reference self-hardening coefficient, a is a hardening exponent, and g_s is a saturated flow stress.

The material parameters of h_0, g_0, g_s and a in equation 4.7, 4.8, 4.9 determines the stress-strain response and evolution of texture of materials. These parameters are inputs of CP-FEM for material properties. Inverse procedure implemented to obtain the materials parameters. The simulations iterated to find the materials parameters yielding the simulation results best fitted to the experimental stress-strain responses. The uni-axial tensile test curve of the polycrystalline was used to fit the material parameters because of the difficulty to obtain the tensile behavior of the single crystal.

The above CP model was implemented using the commercial ABAQUS with user material properties (UMAT) using fortran code. For a simplicity, some factors were not considered: 1) the effect of grain size on yield stress and work hardening, 2) the spatial arrangement of orientation is, and 3) elastic anisotropy.

A simple cubic model with one element was constructed to obtain the flow stress curve under bi-axial loading. The initial inputs for this model are materials parameters (h_0, g_0, g_s and a) and crystal orientations (φ, θ and ψ). In order to determine the material parameters, the tensile test result of the sample from the tube in the axial direction was used for a reference polycrystalline behavior. The best-fit material parameters were used for an input of simulation as mentioned before. In order to represent the initial crystallographic texture without losing the original characteristic grain distribution, the OIM image divided into equal parts, and the one set of Euler angles was extracted from one part. The number of orientations used in this model was 1000. It assumed that this local microstructure distribution represents the overalls through the materials. Twelve slip systems of {111}<110> were operated for Cu with face centered cubic (FCC) crystal structure. For niobium with body centered cubic crystal structure (BCC), the total of 24 slip systems consisting of 12 systems of {110}<111> and 12 systems of {112}<111> were defined. The slip systems of {123}(111) promoted with substitutional impurities were not included.

As mentioned in previous chapter, the CP-FEM was first used for determining the constitutive equation of the sample. The obtained constitutive equation was used for the continuum simulation model. The numerical simulation results were compared to the experimental data.

4.2.2 Multi-scale simulation results

The Cu alloy heat treated for 1h/600°C and Nb heat treated for 2h/1000°C samples were used for the demonstration of the multi-scale simulation. The simulation results of Nb heat treated for other conditions were also included for the future experiments.

In order to obtain the flow stress curve from the CP-FEM, the materials parameters were first determined. Table 4.2 and 4.3 are the best-fit materials parameters for CP-FEM yielding the flow stress curve under uni-axial force equivalent to the experimental tensile test (table 3.6 for Nb and table 3.9 for Cu alloy). Using these numbers, the flow stress curve under bi-axial force was obtained using CP-FEM and fitted. Based on the simulation, the parameters of the deduced constitutive relationship ($\sigma = K \cdot \varepsilon^n$) are $K = 480.59$, $n = 0.410$ for Cu alloy and $K = 291.02$, $n = 0.145$ for Nb, respectively.

Table 4.2 Material parameters of Cu alloy for the CP-FEM

Materials	g_0	h_0	g_s	a
Cu Alloy (1h/600°C)	8	445	1005	26

Table 4.3 Material parameters of Nb for the CP-FEM

Materials	g_0	h_0	g_s	a
Nb (3h/800°C)	60	800	105	1.5
Nb (2h/1000°C)	50	810	95	1.45
Nb (3h/800°C+2h/1000°C)	50	800	150	3.5
Nb (2h/1000°C X 3)	30	1000	120	3

The summarized flow stress curves obtained from the tensile, bulge tests, and CP-FEM were shown in figure 4.4 and figure 4.5 for Cu alloy and Nb samples, respectively. Table 4.4 and 4.5 show the corresponding K and n values for Cu alloy and Nb, respectively. Based on these values, the macroscopic continuum simulations were implemented. Figure 4.6 ~ 4.8 shows the flow stress curves obtained from the tensile test and CP-FEM for Nb samples heat treated for 3h/800°C, 3h/800°C+2h/1000°C, and 2h/1000°C X3, respectively. The summary of plastic properties for inputs of macroscopic model for these Nb tubes was shown in Table 4.6.

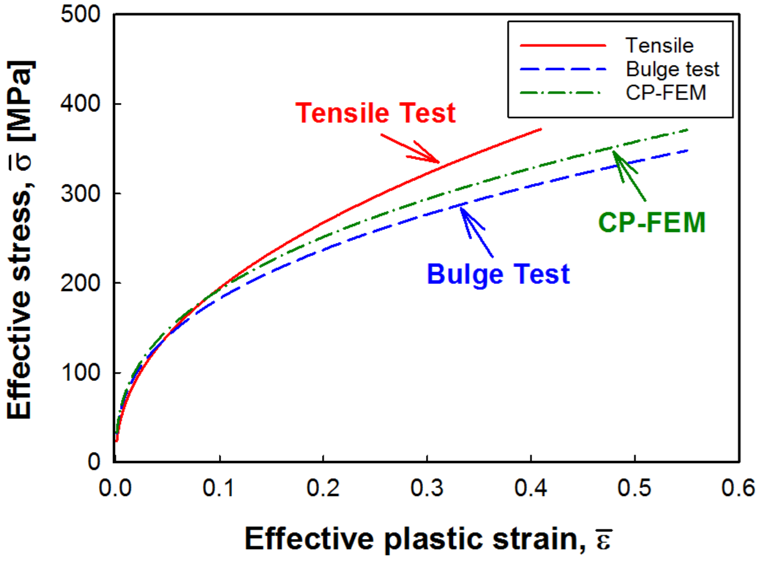

Figure 4.4 Effective stress-plastic strain curves obtained from the tensile, bulge tests and CP-FEM simulation for Cu alloy heat treated for 1h/600°C

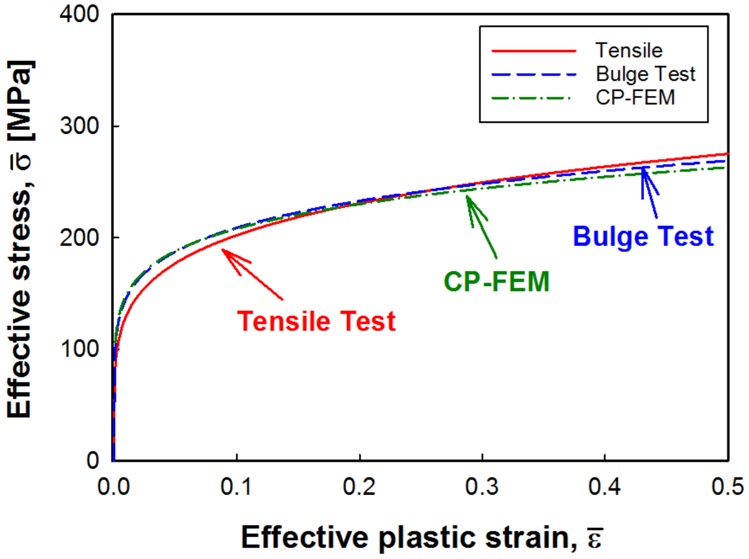

Figure 4.5 Effective stress-plastic strain curves obtained from the tensile, bulge tests and CP-FEM simulation for Nb heat treated for 2h/1000°C

Table 4.4 Summary of plastic properties for inputs of macroscopic model for Cu alloy heat treated for 1h/600°C

	K	*n*
Tensile test	561.20	0.460
Bulge test	436.40	0.378
Crystal plasticity	480.59	0.410

Table 4.5 Summary of plastic properties for inputs of macroscopic model for Nb heat treated for 2h/1000°C

	K	*n*
Tensile test	314.18	0.191
Bulge test	299.99	0.157
Crystal plasticity	291.02	0.145

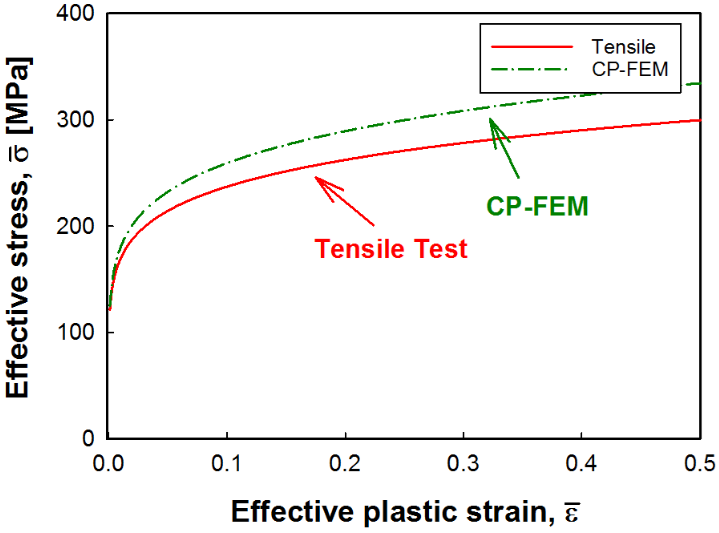

Figure 4.6 Effective stress-plastic strain curves obtained from the tensile, bulge tests and CP-FEM simulation for Nb heat treated for 3h/800°C

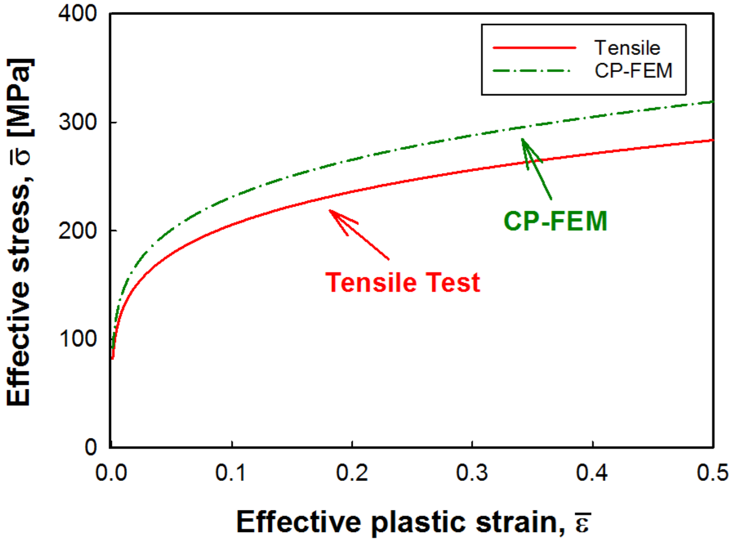

Figure 4.7 Effective stress-plastic strain curves obtained from the tensile, bulge tests and CP-FEM simulation for Nb heat treated for 3h/800°C + 2h/1000°C

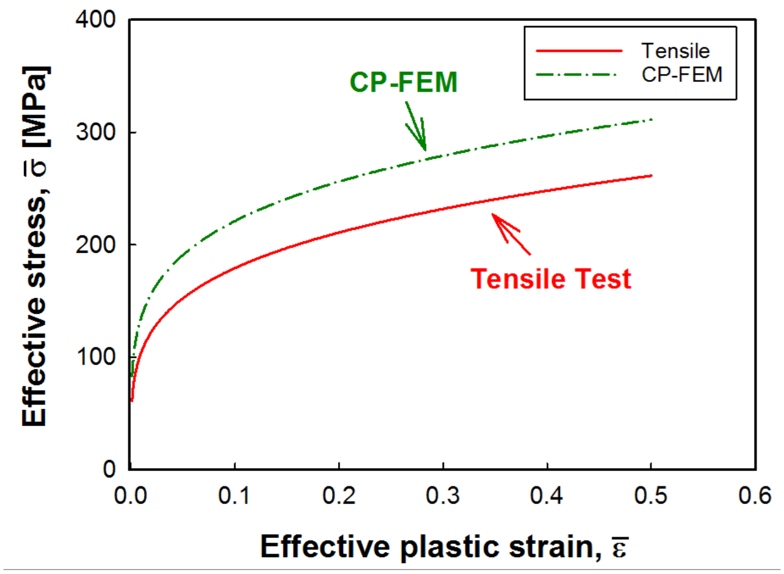

Figure 4.8 Effective stress-plastic strain curves obtained from the tensile, bulge tests and CP-FEM simulation for Nb heat treated for 2h/1000°C X3

Table 4.6 Summary of plastic properties for inputs of macroscopic model for Nb heat treated at various conditions

Material	Method	*K*	*n*
Nb (3h/800°C)	Tensile test	331.61	0.145
	CP-FEM	373.33	0.158
Nb (3h/800°C+2h/1000°C)	Tensile test	325.70	0.200
	CP-FEM	366.54	0.200
Nb (2h/1000°C X 3)	Tensile test	307.46	0.234
	CP-FEM	360.49	0.212

Figure 4.9 show the contour of von Mises stress at pressure of 13.5 and 11.5 MPa for Cu alloy heat treated for 1h/600°C and Nb heat treated for 2h/1000°C, respectively. The results of the simulations expressed in terms of bulge height, *ΔR*, and bulge thickness, *t*, versus pressure were displayed in figures 4.10 for Cu alloy for 1h/600°C and in figure 4.11 for Nb tubes heat treated for 2h/1000°C. In each figure, the experimental results (“**Experiment**”) was compared with the macroscopic simulation results based on the constitutive equations obtained from tensile test (“**Simulation_Tensile test”**), bulge test (“**Simulation_Bulge test**”), and CP-FEM simulation (“**Simualtion_CP**”). The simulation results of Nb heat treated for other conditions were shown in figure 4.12 ~ 4.14. The simulation results based on the flow stress curves from the tensile test and CP-FEM were included.

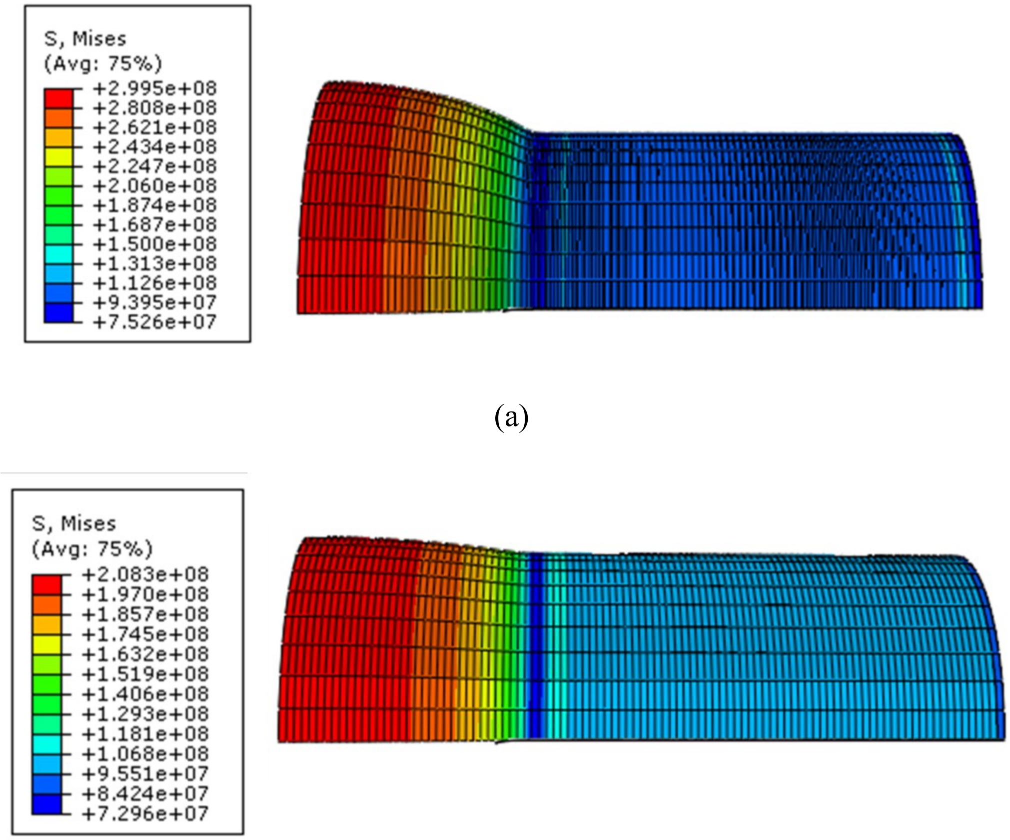

(a)

(b)

Figure 4.9 Contour of von Mises stress of (a) Cu alloy and (b) Nb tubes

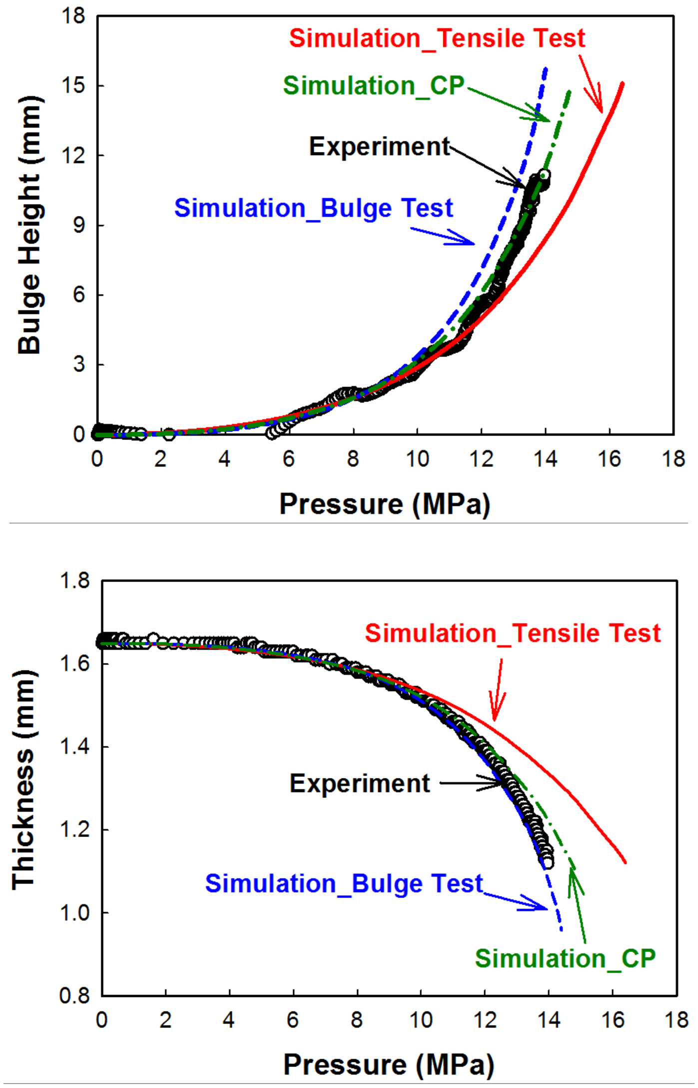

Figure 4.10 Comparison of the results of the experimental bulge test with the results of a bulge test simulation based on the test-derived and CP simulation-derived constitutive relationships for Cu alloy

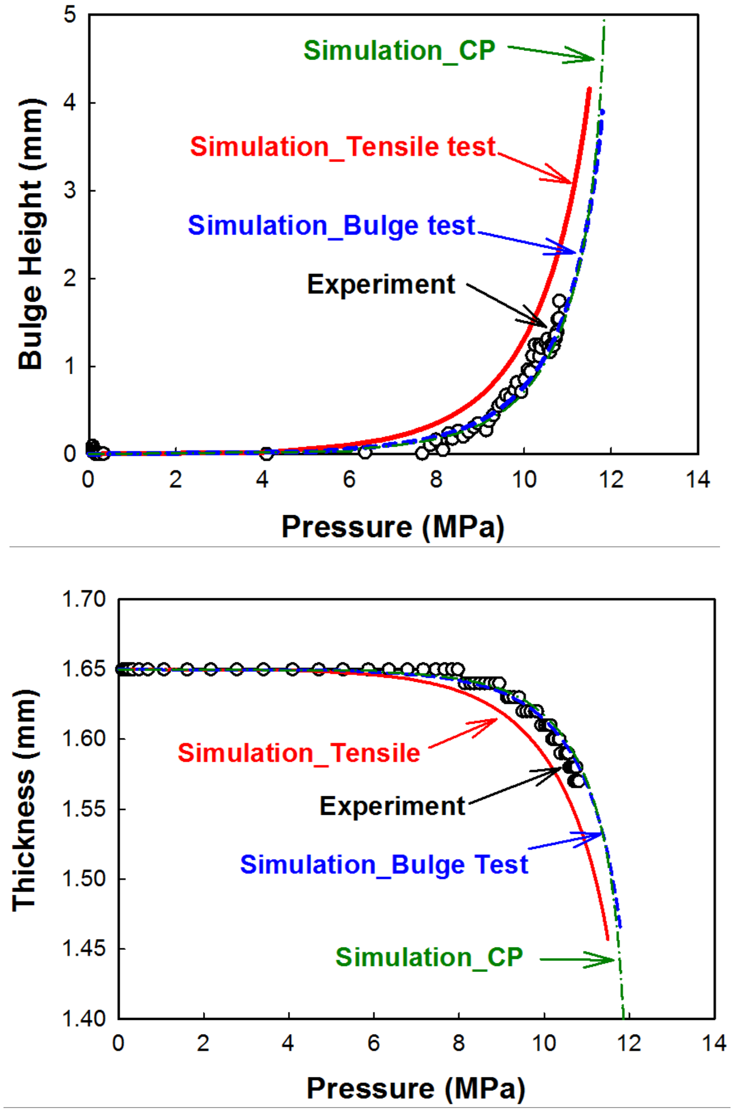

Figure 4.11 Comparison of the results of the experimental bulge test with the results of a bulge test simulation based on the test-derived and CP simulation-derived constitutive relationships for Nb heat treated for 2h/1000°C.

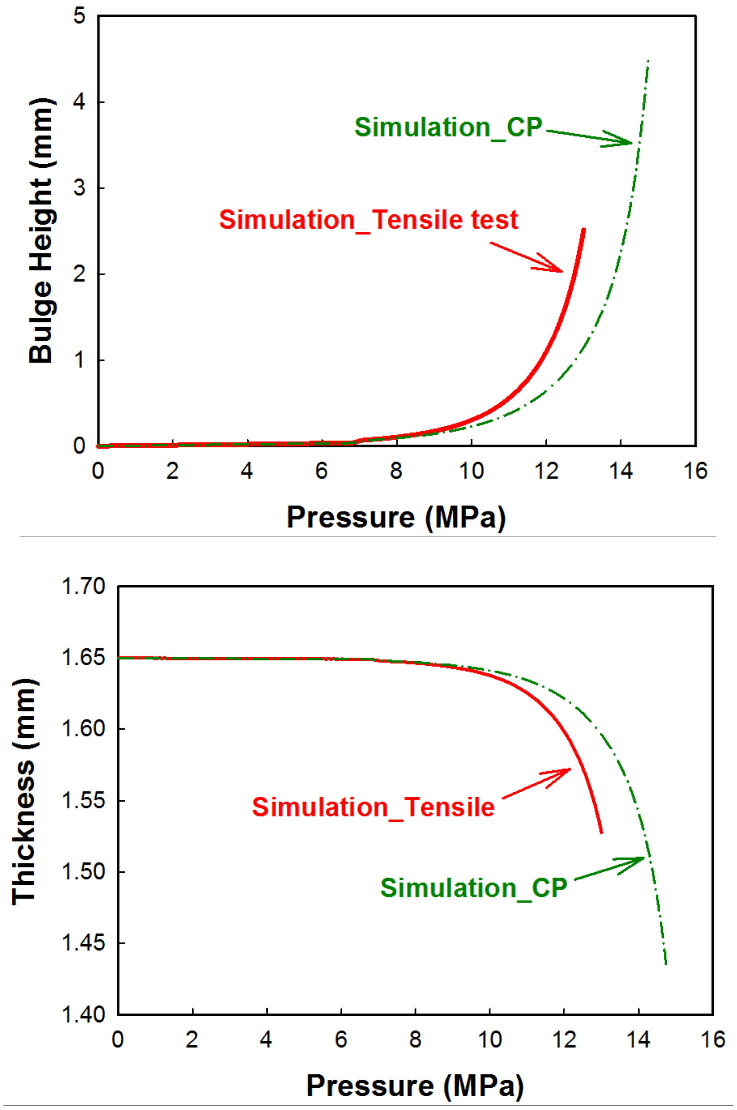

Figure 4.12 Comparison of the results of a bulge test simulation based on the test-derived and CP simulation-derived constitutive relationships for Nb heat treated for 3h/800°C.

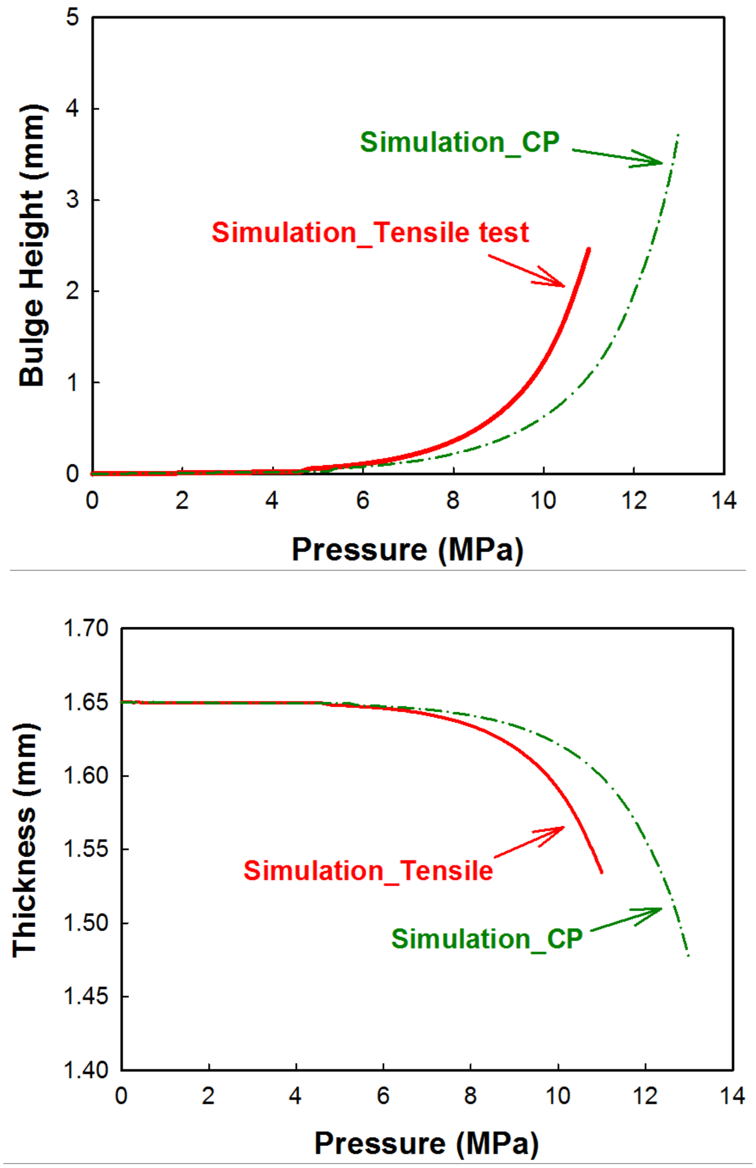

Figure 4.13 Comparison of the results of a bulge test simulation based on the test-derived and CP simulation-derived constitutive relationships for Nb heat treated for 3h/800°C + 2h/1000°C.

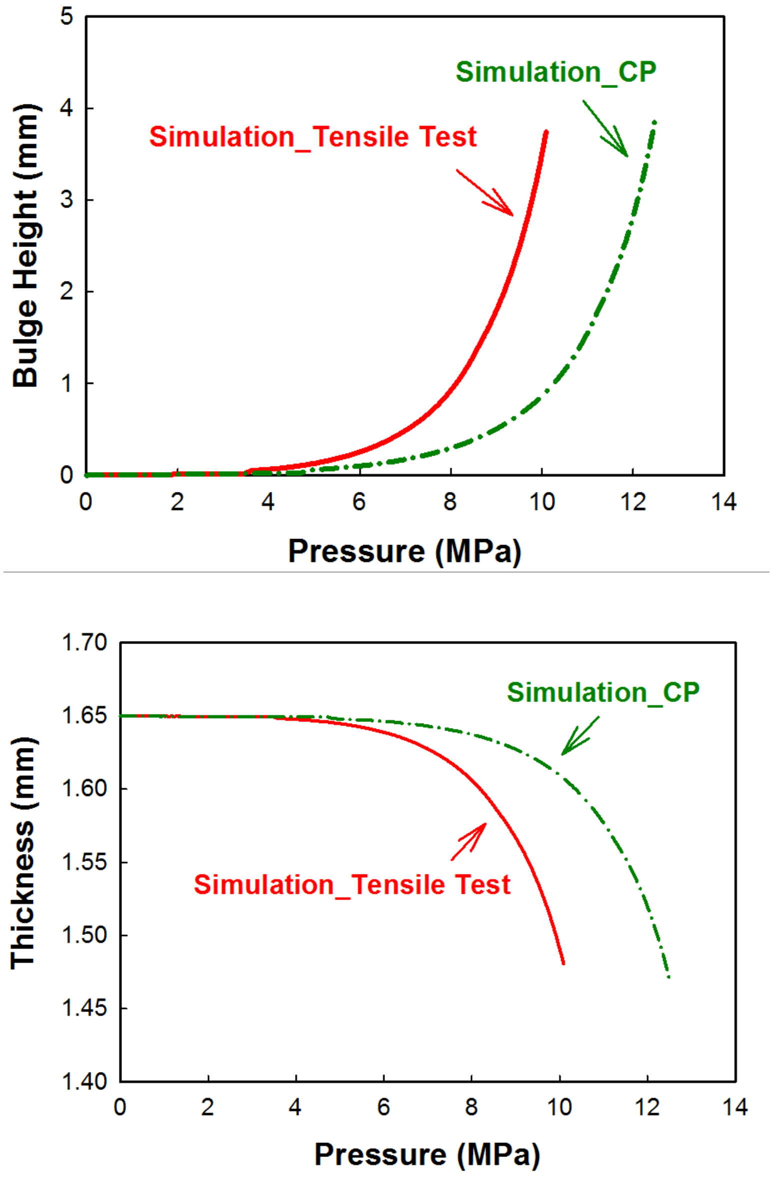

Figure 4.14 Comparison of the results of a bulge test simulation based on the test-derived and CP simulation-derived constitutive relationships for Nb heat treated for 2h/1000°C X3.

For Cu alloy, the results show that the flow stress curve from the bulge test represent more accurate deformation behavior rather than the flow stress curve from the tensile test. Due to multi axial stress state of bulge test it is more accurate to obtain the flow stress curve from the bulge test rather than the uniaxial tensile test. However, the bulge-based numerical simulation and experimental results tend to diverge at pressures above about 10 MPa. It is identical to the results for the high purity Cu tube in previous study. It may be caused by the anisotropic properties or localized deformation as the pressure reaches the burst pressure. During the calculation of the flow stress curve using the analytical model, it assumed that the material is isotropic. However, the orientation of the material will change during deformation. Therefore, the material behavior under large strains may be not isotropic. In order to obtain a more accurate flow stress curve, anisotropic property change during deformation behavior should be considered. The numerical simulation results based on the CP-FEM are well-matched to the experimental data. The CP-FEM considers the orientation and evolution of texture during the deformation. Therefore, it seems that the flow curve from the CP FEM represent more accurate deformation behavior. In case of the Nb tube heat treated for 2h/1000°C, the simulation results based on both bulge test and CP-FEM are well matched to the experimental results. The simulation results of them slightly tended to diverged at large strain, but the tube failed at lower strain range.

The constitutive equation using the CP-FEM based on the orientation information yields best fit simulation results comparing the experimental results. Therefore, the simulation strategy using combination of continuum and CP models will be possible to expect the accurate deformation behavior of tube materials instead of a full bulge CP model requiring expensive computing time.

CHAPTER 5: SUMMARY AND CONCLUSIONS

Experimental and numerical analysis of hydroformed tubular materials was performed to determine the best approach to modeling and quantitative prediction of Nb tube behavior under hydroforming with application to seamless SRF cavity fabrication for high energy particle acceleration. In the experimental part of the study samples removed from representative tubes were prepared for heat treatment, tensile testing, *RRR* measurement, and OIM. After being optimally heat treated Cu and Nb tubes were subjected to hydraulic bulge testing and the results analyzed. In order to develop a numerical simulation model, two different approaches were used, continuum and multi-scale.

For a continuum model, the empirical constitutive equations of tubular materials were obtained from both tensile and bulge tests to determine the most accurate constitutive equation under muti-axial loading. The stress-strain relationship determined from the bulge test represents a more exact description of the deformation behavior than that from tensile tests made on segments cut from the tubular materials. The incorporation of small residual anisotropic effects using anisotropic properties from the tensile test led to even more accurate results for the anisotropic material.

Multi-scale numerical simulation was also investigated. CP-FEM incorporating tube texture and orientation information was performed to obtain the flow stress curve as well as materials orientation and texture evolution during deformation. The continuum modeling was then carried out using the obtained constitutive equations. The constitutive equation using the CP-FEM based on the orientation information yielded the best fit simulation results as compared to the experimental results. Therefore, using a simulation strategy which employs a combination of continuum and CP models as a multi-scale simulation it is possible to expect to accurately predict the deformation behavior of tubular materials. In principle, this approach reduces or eliminates the need for direct hydraulic bulge testing, which will contribute to a reduction in time and cost for SRF development and help choose the best textures and tube forming processes for SRF hydroforming applications.

References

[1] E. W. Collings, "Normal and superconducting radio-frequency cavities for high energy particle accelerators," in *2011 International Conference on Applied Superconductivity and Electromagnetic Devices*.

[2] P. Marchand, "Superconducting RF cavities for synchrotron light sources," in *Proceedings of EPAC'04*, 2004, p. 21.

[3] W. Weingarten, "Superconducting cavities - Basics," *Cas - Cern Accelerator School: Superconductivity in Particle Accelerators, Proceedings,* vol. 96, pp. 167-189, 1996.

[4] H. Padamsee, J. Knobloch, and T. Hays, *RF superconductivity for accelerators*. New York: Wiley, 1998.

[5] B. Seeber, *Handbook of applied superconductivity*. Philadelphia, PA: Institute of Physics Pub., 1998.

[6] P. Kneisel, "High gradient superconducting niobium cavities - A review of the present status," *IEEE Transactions on Applied Superconductivity,* vol. 9, pp. 1023-1029, Jun 1999.

[7] R. L. Geng, H. Padamsee, A. Seaman, and V. D. Shemelin, "World record accelerating gradient achieved in a superconducting niobium RF cavity," *2005 Ieee Particle Accelerator Conference (Pac), Vols 1-4,* pp. 1313-1315, 2005.

[8] H. Padamsee, "Accelerating applications of RF superconductivity - Success stories," *IEEE Transactions on Applied Superconductivity,* vol. 15, pp. 2432-2439, Jun 2005.

[9] W. Singer, "SRF Cavity Fabrication and Materials," *arXiv preprint arXiv:1501.07142,* 2015.

[10] V. Palmieri, "Seamless superconducting RF cavities," in *Particle Accelerator Conference, 1999. Proceedings of the 1999*, 1999, pp. 541-544 vol.1.

[11] P. Kneisel and V. Palmieri, "Development of seamless niobium cavities for accelerator applications," in *Particle Accelerator Conference, 1999. Proceedings of the 1999*, 1999, pp. 943-945 vol.2.

[12] S. M'Garrech, M. Fouaidy, J. Lesrel, V. Palmieri, and S. Bousson, "Study of superconducting RF 3 GHz cavities realized by spinning," *Journal of Superconductivity and Novel Magnetism,* vol. 20, pp. 233-238, Apr 2007.

[13] V. Palmieri, "Seamless cavities: the most creative topic in RF Superconductivity," in *the 8th Workshop on RF Superconductivity*, Italy, 1997.

[14] W. Singer, I. Gonin, I. Jelezov, H. Kaiser, T. Khabibuline, P. Kneisel*, et al.*, "Hydroforming of Tesla cavities ar DESY " in *EPAC*, Vienna, Austria, 2000, pp. 327-329.

[15] W. Singer, H. Kaiser, X. Singer, G. Weichert, I. Jelezov, T. Khabibuline*, et al.*, "Hydroforming of Superconducting TESLA Cavities," in *The 10th Workshop on RF Superconductivity*, Tsukuba, Japan, 2001, pp. 170-176.

[16] W. Singer, X. Singer, K. Twarowski, I. Jelezov, T. Khabibuline, A.Skasyrskaia*, et al.*, "Hydroforming of NbCu Clad Cavities at DESY," in *The 10th Workshop on RF Superconductivity*, Tsukuba, Japan, 2001, pp. 467-470.

[17] W. Singer, "Seamless/bonded niobium cavities," *Physica C,* vol. 441, pp. 89-94, 2006.

[18] W. Singer, "SC Cavities;Material, Fabrication and QA," presented at the The14th International Workshop on RF Superconductivity, Dresden, Germany, 2009.

[19] W. Singer., "Hydroforming of Seamless Cavities," presented at the ECFA-CLIC-ILC Meeting, SCRF Session, Geneva, 2010.

[20] K. Saito, T. Fujino, N. Hitomi, H. Inoue, Y. Yamazaki, V. Palmieri*, et al.*, "R&D of Nb/Cu clad seamless cavities at KEK," in *Proc. in the 10th Workshop on RF Superconductivity, Tsukuba, Japan*, 2001.

[21] W. Singer, X. Singer, I. Jelezov, and P. Kneisel, "Hydroforming of elliptical cavities," *Physical Review Special Topics-Accelerators and Beams,* vol. 18, p. 22, Feb 2015.

[22] R. R. Calaga, "Linear Beam Dynamics and Ampere Class Superconducting RF Cavities @RHIC," Doctor of Philosophy, Stony Brook University, 2006.

[23] A. C. Rose-Innes and E. H. Rhoderick, *Introduction to superconductivity*, [1st ed. Oxford, New York,: Pergamon Press, 1969.

[24] W. Meissner and R. Ochsenfeld, "Short initial announcements.," *Naturwissenschaften,* vol. 21, pp. 787-788, 1933.

[25] P. J. Lee, *Engineering superconductivity*. New York: Wiley-Interscience, 2001.

[26] J. Knobloch, "Advanced thermometry studies of superconducting RF cavities," Doctor of philosophy, Cornell University, 1997.

[27] B. Bonin, "Field emission in RF cavities," *CERN EUROPEAN ORGANIZATION FOR NUCLEAR RESEARCH-REPORTS-CERN,* pp. 221-230, 1996.

[28] L. Cooley, "Pits in SRF Cavities: Do EB weld arcs contribute?," in *Workshop on Unipolar Arcs*, Chicago, 2010.

[29] V. Palmieri, "Advancements on spinning of seamless multicell reentrant cavities," in *the 11th Workshop on RF Superconductivity SRF2003*, Lübeck, Germany, 2003.

[30] F. Dohmann and C. Hartl, "Hydroforming - a method to manufacture light-weight parts," *Journal of materials processing technology,* vol. 60, pp. 669-676, 1996.

[31] F. Dohmann and C. Hartl, "Hydroforming-a method to manufacture light-weight parts," *Journal of materials processing technology,* vol. 60, pp. 669-676, 1996.

[32] F. Dohmann and C. Hartl, "Hydroforming-applications of coherent FE-simulations to the development of products and processes," *Journal of materials processing technology,* vol. 150, pp. 18-24, 2004.

[33] L. Lang, Z. Wang, D. Kang, S. Yuan, S.-H. Zhang, J. Danckert*, et al.*, "Hydroforming highlights: sheet hydroforming and tube hydroforming," *Journal of materials processing technology,* vol. 151, pp. 165-177, 2004.

[34] S.-H. Zhang, "Developments in hydroforming," *Journal of materials processing technology,* vol. 91, pp. 236-244, 1999.

[35] M. Koc and T. Altan, "An overall review of the tube hydroforming (THF) technology," *Journal of materials processing technology,* vol. 108, pp. 384-393, 2001.

[36] W. Rimkus, H. Bauer, and M. Mihsein, "Design of load-curves for hydroforming applications," *Journal of materials processing technology,* vol. 108, pp. 97-105, 2000.

[37] A. Aydemir, J. De Vree, W. Brekelmans, M. Geers, W. Sillekens, and R. Werkhoven, "An adaptive simulation approach designed for tube hydroforming processes," *Journal of materials processing technology,* vol. 159, pp. 303-310, 2005.

[38] Y. Aue-U-Lan, G. Ngaile, and T. Altan, "Optimizing tube hydroforming using process simulation and experimental verification," *Journal of materials processing technology,* vol. 146, pp. 137-143, 2004.

[39] M. Koc and T. Altan, "Prediction of forming limits and parameters in the tube hydroforming process," *International Journal of Machine Tools and Manufacture,* vol. 42, pp. 123-138, 2002.

[40] J. Kim, S.-W. Kim, H.-J. Park, and B.-S. Kang, "A prediction of bursting failure in tube hydroforming process based on plastic instability," *The International Journal of Advanced Manufacturing Technology,* vol. 27, pp. 518-524, 2006.

[41] Z. Xia, "Failure analysis of tubular hydroforming," *Journal of Engineering Materials and Technology,* vol. 123, pp. 423-429, 2001.

[42] V. Mises, "Mechanics of solids in plastic state," *Gottinger Nachrichten Math. Phys. Klasse,* p. 582, 1913.

[43] R. Hill, "A Theory of the Yielding and Plastic Flow of Anisotropic Metals," *Proceedings of the Royal Society of London Series a-Mathematical and Physical Sciences,* vol. 193, pp. 281-297, 1948.

[44] G. E. Dieter, *Mechanical metallurgy*. New York,: McGraw-Hill, 1961.

[45] R. H. Wagoner and J. L. Chenot, *Fundamentals of metal forming*. New York: Wiley, 1997.

[46] Z. Marciniak and J. L. Duncan, *The Mechanics of sheet metal forming*. London: Edward Arnold, 1992.

[47] D. Banabic, *Formability of metallic materials : plastic anisotropy, formability testing, forming limits*. Berlin; New York: Springer, 2000.

[48] W. T. Lankford, S. C. Snyder, and J. A. Bauscher, "New criteria for predicting the press performance of deep drawing sheets," *Transactions of the American Society for Metals,* vol. 42, pp. 1197-1232, 1950 1950.

[49] S. Nemat-Nasser and W. G. Guo, "Flow stress of commercially pure niobium over a broad range of temperatures and strain rates," *Materials Science and Engineering a-Structural Materials Properties Microstructure and Processing,* vol. 284, pp. 202-210, May 31 2000.

[50] T. S. Byun, S. H. Kim, and J. Mammosser, "Low-temperature mechanical properties of superconducting radio frequency cavity materials," *Journal of Nuclear Materials,* vol. 392, pp. 420-426, Aug 1 2009.

[51] H. Jiang, D. Baars, A. Zamiri, C. Antonie, P. Bauer, T. R. Bieler*, et al.*, "Mechanical properties of high RRR niobium with different texture," *IEEE Transactions on Applied Superconductivity,* vol. 17, pp. 1291-1294, Jun 2007.

[52] A. Zamiri, F. Pourboghrat, H. Jiang, T. R. Bieler, F. Barlat, J. Brem*, et al.*, "On mechanical properties of the superconducting niobium," *Materials Science and Engineering a-Structural Materials Properties Microstructure and Processing,* vol. 435, pp. 658-665, Nov 5 2006.

[53] M. Imaninejad, G. Subhash, and A. Loukus, "Loading path optimization of tube hydroforming process," *International Journal of Machine Tools & Manufacture,* vol. 45, pp. 1504-1514, Oct 2005.

[54] T. Sokolowski, K. Gerke, M. Ahmetoglu, and T. Altan, "Evaluation of tube formability and material characteristics: hydraulic bulge testing of tubes," *Journal of materials processing technology,* vol. 98, pp. 34-40, Jan 15 2000.

[55] Y. M. Hwang and C. W. Wang, "Flow stress evaluation of zinc copper and carbon steel tubes by hydraulic bulge tests considering their anisotropy," *Journal of materials processing technology,* vol. 209, pp. 4423-4428, May 1 2009.

[56] A. Zamiri and F. Pourboghrat, "Characterization and development of an evolutionary yield function for the superconducting niobium sheet," *International Journal of Solids and Structures,* vol. 44, pp. 8627-8647, Dec 15 2007.

[57] A. Zamiri, H. Jiang, T. R. Bieler, and F. Pourboghrat, "Applying evolutionary yield function to predicting the deformation of microstructure-sensitive High-RRR niobium," *Jom,* vol. 60, pp. 70-75, Jul 2008.

[58] F. Barlat, J. C. Brem, J. W. Yoon, K. Chung, R. E. Dick, D. J. Lege*, et al.*, "Plane stress yield function for aluminum alloy sheets—part 1: theory," *International Journal of Plasticity,* vol. 19, pp. 1297-1319, 2003.

[59] F. Barlat and K. Lian, "Plastic behavior and stretchability of sheet metals. Part I: A yield function for orthotropic sheets under plane stress conditions," *International Journal of Plasticity,* vol. 5, pp. 51-66, 1989.

[60] D. C. Ahn, J. W. Yoon, and K. Y. Kim, "Modeling of anisotropic plastic behavior of ferritic stainless steel sheet," *International Journal of Mechanical Sciences,* vol. 51, pp. 718-725, 2009.

[61] G. Sachs, "Zur ableitung einer fliessbedingung," in *Mitteilungen der deutschen Materialprüfungsanstalten*, ed: Springer, 1929, pp. 94-97.

[62] G. I. Taylor, "Plastic Strain in Metals," *Journal of the Institute of Metals,* vol. 62, pp. 307-324, 1938.

[63] G. R. C. U.F. Kocks, "How many slip systems, and which?," in *2nd Risø international symposium on metallurgy and materials science*, Risø National Laboratory, Denmark, 1981.

[64] P. Van Houtte, "Adaptation of the Taylor theory to the typical substructure of some cold rolled fcc metals," *Tokyo: Iron Institute of Japan,* vol. 428, 1981.

[65] E. Kröner, "Zur plastischen verformung des vielkristalls," *Acta metallurgica,* vol. 9, pp. 155-161, 1961.

[66] B. Budiansky and T. T. WU, "Theoretical prediction of plastic strains of polycrystals," DTIC Document1961.

[67] N. Fleck, G. Muller, M. Ashby, and J. Hutchinson, "Strain gradient plasticity: theory and experiment," *Acta Metallurgica et Materialia,* vol. 42, pp. 475-487, 1994.

[68] N. Fleck and J. Hutchinson, "Strain gradient plasticity," *Advances in applied mechanics,* vol. 33, pp. 296-361, 1997.

[69] M. E. Gurtin, "A gradient theory of single-crystal viscoplasticity that accounts for geometrically necessary dislocations," *Journal of the Mechanics and Physics of Solids,* vol. 50, pp. 5-32, 2002.

[70] M. E. Gurtin, "On the plasticity of single crystals: free energy, microforces, plastic-strain gradients," *Journal of the Mechanics and Physics of Solids,* vol. 48, pp. 989-1036, 2000.

[71] L. Evers, D. Parks, W. Brekelmans, and M. Geers, "Crystal plasticity model with enhanced hardening by geometrically necessary dislocation accumulation," *Journal of the Mechanics and Physics of Solids,* vol. 50, pp. 2403-2424, 2002.

[72] A. Arsenlis and D. M. Parks, "Modeling the evolution of crystallographic dislocation density in crystal plasticity," *Journal of the Mechanics and Physics of Solids,* vol. 50, pp. 1979-2009, 2002.

[73] A. Arsenlis, D. M. Parks, R. Becker, and V. V. Bulatov, "On the evolution of crystallographic dislocation density in non-homogeneously deforming crystals," *Journal of the Mechanics and Physics of Solids,* vol. 52, pp. 1213-1246, 2004.

[74] D. Peirce, R. Asaro, and A. Needleman, "An analysis of nonuniform and localized deformation in ductile single crystals," *Acta metallurgica,* vol. 30, pp. 1087-1119, 1982.

[75] R. J. Asaro, "Micromechanics of Crystals and Polycrystals," in *Advances in Applied Mechanics*. vol. Volume 23, W. H. John and Y. W. Theodore, Eds., ed: Elsevier, 1983, pp. 1-115.

[76] P. R. Dawson, "Computational crystal plasticity," *International Journal of Solids and Structures,* vol. 37, pp. 115-130, 2000.

[77] D. Raabe, P. Klose, B. Engl, K.-P. Imlau, F. Friedel, and F. Roters, "Concepts for integrating plastic anisotropy into metal forming simulations," *Advanced Engineering Materials,* vol. 4, p. 169, 2002.

[78] S. R. Kalidindi, C. A. Bronkhorst, and L. Anand, "Crystallographic texture evolution in bulk deformation processing of FCC metals," *Journal of the Mechanics and Physics of Solids,* vol. 40, pp. 537-569, 1992.

[79] P. Dawson, S. MacEwen, and P. Wu, "Advances in sheet metal forming analyses: dealing with mechanical anisotropy from crystallographic texture," *International Materials Reviews,* vol. 48, pp. 86-122, 2003.

[80] E. Nakamachi, C. Xie, and M. Harimoto, "Drawability assessment of BCC steel sheet by using elastic/crystalline viscoplastic finite element analyses," *International journal of mechanical sciences,* vol. 43, pp. 631-652, 2001.

[81] D. Peirce, R. J. Asaro, and A. Needleman, "Material rate dependence and localized deformation in crystalline solids," *Acta metallurgica,* vol. 31, pp. 1951-1976, 1983.

[82] G. Sarma and P. Dawson, "Effects of interactions among crystals on the inhomogeneous deformations of polycrystals," *Acta Materialia,* vol. 44, pp. 1937-1953, 1996.

[83] R. J. Asaro and A. Needleman, "Overview no. 42 Texture development and strain hardening in rate dependent polycrystals," *Acta metallurgica,* vol. 33, pp. 923-953, 1985.

[84] A. Siddiq and S. Schmauder, "Crystal plasticity parameter identification procedure for single crystalline material during deformation," *J Comput Appl Mech,* vol. 7, pp. 1-15, 2006.

[85] Y. Guan, F. Pourboghrat, and F. Barlat, "Finite element modeling of tube hydroforming of polycrystalline aluminum alloy extrusions," *International journal of plasticity,* vol. 22, pp. 2366-2393, 2006.

[86] A. E8, "Standard test methods for tensile testing of metallic materials," *Annual book of ASTM standards,* vol. 3, 1997.

[87] F. R. Fickett, "Oxygen annealing of copper: A review," *Materials Science and Engineering,* vol. 14, pp. 199-210, 1974.

[88] E. Collings, *Physics of solid solution strengthening*: Springer Science & Business Media, 2012.

[89] F. Fickett, "Electrical properties," *Materials at low temperatures,* p. 163, 1983.

[90] T. G. Nieh and W. D. Nix, "Embrittlement of copper due to segregation of oxygen to grain boundaries," *Metallurgical Transactions A,* vol. 12, pp. 893-901, 1981/05/01 1981.

[91] I. Abdyukhanov, A. Vorobieva, E. Dergunova, M. Polikarpova, K. Mareev, N. Traktirnikova*, et al.*, "The RRR Parameter of the ITER Type Bronze-Route Cr-Coated Nb3Sn Strands after Different Heat Treatments," *Applied Superconductivity, IEEE Transactions on,* vol. 22, pp. 4802804-4802804, 2012.

[92] F. Fickett, "Oxygen-free copper at 4 K: resistance and magnetoresistance," *Magnetics, IEEE Transactions on,* vol. 19, pp. 228-231, 1983.

[93] J. H. Hollomon, "Tensile deformation," *AIME TRANS,* vol. 12, pp. 1-22, 1945.

[94] P. Bortot, E. Ceretti, and C. Giardini, "The determination of flow stress of tubular material for hydroforming applications," *Journal of materials processing technology,* vol. 203, pp. 381-388, Jul 18 2008.

[95] S. Fuchizawa and M. Narazaki, "Bulge test for determining stress-strain characteristics of thin tubes," in *The fourth international conference on technology of plasticity*, 1993, pp. 488-493.

[96] M. Koc, Y. Aue-u-lan, and T. Altan, "On the characteristics of tubular materials for hydroforming - experimentation and analysis," *International Journal of Machine Tools & Manufacture,* vol. 41, pp. 761-772, Apr 2001.

[97] R. Hill, *The mathematical theory of plasticity*. Oxford,: Clarendon Press, 1950.

[98] S. Fuchizawa, "Influence of plastic anisotropy on defromation of thin-walled tubes in bulge forming," in *The second International Conference on Technology of Plasticity*, Stuttgart, 1987, pp. 727-732.

[99] Y.-M. Hwang and Y.-K. Lin, "Evaluation of flow stresses of tubular materials considering anisotropic effects by hydraulic bulge tests," *Journal of Engineering Materials and Technology-Transactions of the Asme,* vol. 129, pp. 414-421, Jul 2007.

[100] R. W. Hertzberg, "Deformation and fracture mechanics of engineering materials," 1989.

[101] D. Systèmes, "Abaqus analysis user's manual," *Simulia Corp. Providence, RI, USA,* 2007.

[102] Y. Lianfa and G. Cheng, "Determination of stress–strain relationship of tubular material with hydraulic bulge test," *Thin-Walled Structures,* vol. 46, pp. 147-154, 2008.

[103] M. Strano and T. Altan, "An inverse energy approach to determine the flow stress of tubular materials for hydroforming applications," *Journal of materials processing technology,* vol. 146, pp. 92-96, Feb 15 2004.

Appendix A: Analysis of Reactor-Grade Niobium

Element	Content (%)	Element	Content (%)
C	0.003	N	0.0005
O	0.001	H	0.0006
Zr	0.004	Ta	0.02
Fe	0.002	Si	0.0003
W	0.0005	Ni	0.0007
Mo	0.005	Hf	0.003
Ti	0.0006	Nb	balance

Appendix B: Labview Program for Data Acquisition of Tube Bulge Test

Front Panel

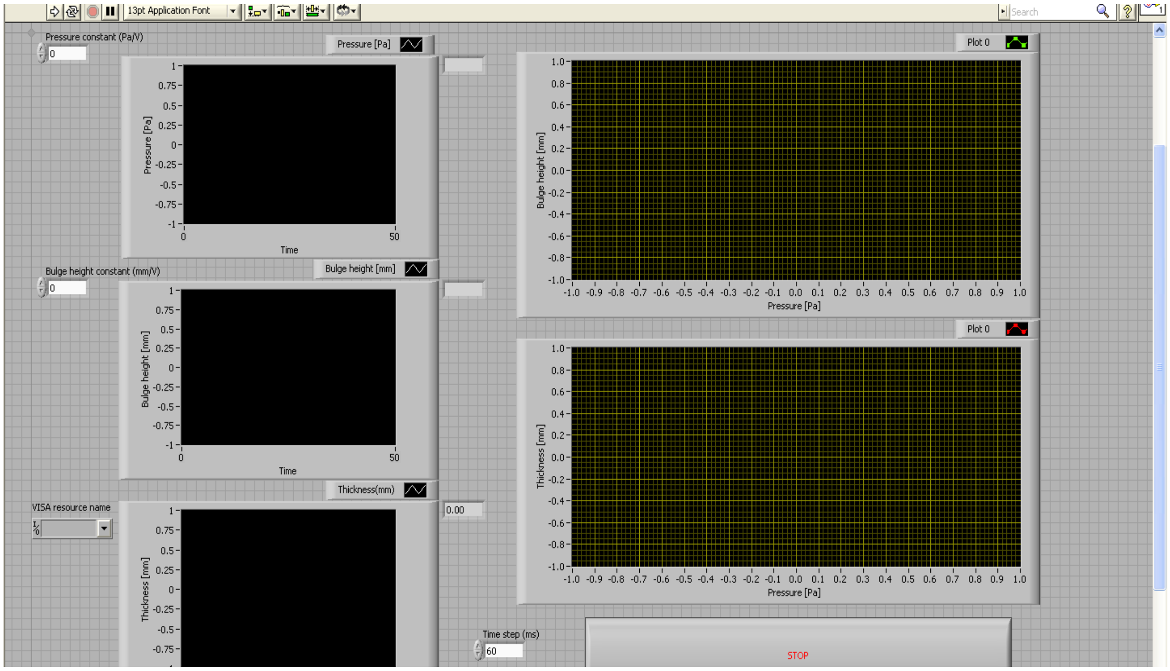

Pressure constant (Pa/V) 0

Bulge height constant (mm/V) 0

Time step (ms) 60

Block Diagram